QUANTITATIVE INSIGHTS INTO DEVELOPMENTAL SIGNALS AND PHENOTYPES IN *C. ELEGANS*

Thesis by

Claudiu Giurumescu

In Partial Fulfillment of the Requirements

for the Degree of

Doctor of Philosophy

CALIFORNIA INSTITUTE OF TECHNOLOGY
Pasadena, California

2008

(Defended July 31, 2007)

ACKNOWLEDGEMENTS

I would foremost like to thank my thesis advisor Professor Anand Asthagiri for allowing me to pursue projects that excite me at my own pace. During my residency at Caltech, he has changed the way I perceive science and view the world. From him I have learned to question reality in the most counterintuitive ways; his keen insight will always amaze me.

I want to thank Professor Paul Sternberg for giving me the opportunity to work in his laboratory and for inspiring me with the excitement of doing science. He played a great role in my decision to wavily go the "worm way" in my scientific career after Caltech. I would also like to thank my other thesis committee members, Professors Mark Davis, David Tirrell and Zhen-Gang Wang, for their valuable time and advice.

The experience at Caltech would not have been complete without my labmates Nick Graham, Niki Galownia, Steve Chapman, Melissa Pope, Kei Kushiro, Jin-Hong Kim, and Paul Minor. I have learned a lot from all of you and I will always appreciate your daily companionship while I was at Caltech. I am also indebted for their friendship to Tharathorn Rimchala and Yuan Gong, whom I had the opportunity to mentor at various times in the Asthagiri lab.

Many thanks to all the mentors that I have had throughout my years of formal education. I would like to thank my high-school chemistry teacher Zena Popa for her belief in my abilities and support in pursuing my passion for chemistry and Professors Cornelia Guran and Sorin Roşca for further guiding me in my learning of chemistry. I would also like to thank my undergraduate mentor, Professor Bernhardt Trout, for allowing me to learn all the things I nowadays know about computers in his computational lab.

Finally, I would like to thank my wife Thuy for her immeasurable help and patience throughout the late part of my PhD and for her strong encouragements.

ABSTRACT

Design of biomaterials and cellular scaffolds for tissue-engineering applications and regenerative medicine requires a precise understanding of the principles underlying multicellular patterning. Adhesion, migration, division, differentiation, and apoptosis are characteristic cellular behaviors, the engineering of which has the potential to allow creation of custom, multicellular structures. These cellular events occur naturally during embryonic and postembryonic development of multicellular organisms. Development thus offers the opportunity to learn about the design principles and molecular mechanisms that guide cellular patterning.

A key finding in developmental biology is that a limited set of conserved molecular signaling pathways act at multiple times and locations throughout the embryo to introduce cell-fate asymmetries in homogenous populations of cells. In turn, these asymmetries serve as starting points for the patterning of new organs. These signaling pathways interact quantitatively at multiple levels, including signaling cues, post-translational regulation, and gene-regulatory networks, to guide multicellular patterning.

How does the quantitative performance of these signaling networks ensure the intended phenotype pattern? How do changes in the quantitative performance of these networks, possibly over the course of evolution, give rise to new phenotypes? These are the central questions pursued in this thesis.

In order to answer such questions, we used vulva formation in the nematode *Caenorhabditis elegans* as a model system of cellular patterning. We formulated a mathematical model of the molecular network underlying cellular-fate specification in this system. Computational analysis of this molecular network reveals that cell–cell coupling through lateral LIN-12/Notch signaling amplifies the perception of the gradient in the epidermal-growth-factor-like soluble cue, LIN-3. Thus, the gradient in LIN-3 concentration produces an even steeper difference in LIN-3-mediated intracellular signals between adjoining cells. Such gradient amplification may be particularly important in converting a shallow, graded-specification signal into a spatial pattern of distinct fate choices.

Through quantitative perturbations of interaction strengths between components of the vulval patterning network, we further show that our modeling approach can correctly predict phenotype patterns observed in *C. elegans* mutation studies. This study generated a framework for quantitative analysis of molecular networks that links quantitative molecular perturbations to patterning outcomes. This framework will prove useful in the analysis of other systems involving cellular fate decisions and in tissue engineering applications where the generation of precise cell patterns is needed. We demonstrate the generality of our approach through an application to evolutionary developmental biology. Since molecular connectivity of the vulva patterning network of several closely related *Caenorhabditis* species is preserved, we correctly predict the quantitative diversification that must have occurred in this network during species evolution.

TABLE OF CONTENTS

LIST OF FIGURES

LIST OF TABLES

CHAPTER 1: MULTICELLULAR PATTERNING IN DEVELOPMENT

1.1 Abstract

Developing design strategies for tissue engineering and regenerative medicine is limited by our nascent understanding of how cell populations “self-organize” into multicellular structures on synthetic scaffolds. Mechanistic insights and design principles can be gleaned from the quantitative analysis of multicellular patterning during the natural processes of embryonic and adult development. This chapter describes the critical layers of signaling mechanisms that drive developmental multicellular patterning: spatiotemporal presentation of extracellular cues, intracellular signaling networks that mediate crosstalk among extracellular cues, and finally, intranuclear signal integration at the level of transcriptional regulatory networks. At every level in this hierarchy, the *quantitative* attributes of signals have a profound impact on patterning. We discuss how the simple model organism *Caenorhabditis elegans* may be used to uncover these quantitative features and their impact on multicellular phenotype through mathematical modeling and quantitative experiments.

1.2 Introduction

The development of a multicellular organism from an embryo is one of nature’s most remarkable phenomena. Deciphering how this transformation occurs is a fundamental challenge in biology with profound biomedical implications. Insights into the molecular signals guiding developmental patterning will provide design strategies to promote multicellular structure formation in applications such as tissue engineering and regenerative medicine. Recently, significant attention has been given to the use of stem cells in these applications. A major challenge, however, is to engineer a cellular microenvironment that presents the right combination of cues to promote differentiation and cellular "self-organization." This bioengineering challenge will undoubtedly benefit from a more quantitative and integrative understanding of developmental signals. In fact, gleaning design insight from natural developmental processes is imperative, since erroneous manipulation of developmental mechanisms can lead to pathologies. Perhaps, the most striking example is that aberrations in developmental signals play a prominent role in the structural and functional regression of tissues during cancer development [1]. Development begins with asymmetric divisions of the fertilized egg, partitioning it into distinct groups of cells or "progenitor fields" that will ultimately develop into future organs [2]. Each group executes a distinct gene expression program, thereby specifying it toward a unique developmental fate. The next round of specification cues further subdivides the progenitor field, with each subgroup now executing a distinct specification (i.e., gene expression) program. Thus, development involves successive rounds of asymmetry-inducing specification cues that trigger specific gene expression programs. Interspersed among these successive rounds is the cellular execution of the gene expression program. Specifically, this program dictates cell behaviors, such as division, migration, death, and extracellular matrix deposition and remodeling—events that shape and functionalize developing tissues, and ultimately, the organism.

Thus, the molecular signals at the heart of development are the specification cues and the network of biochemical reactions that process these cues and instruct the appropriate cell behavioral response. Specification cues must encode spatial information, since groups of cells must be partitioned according to a precise three-dimensional geometry. Once the specification cue has been perceived, cells must then execute the downstream gene expression program in a *context-sensitive* manner. Here, context has twofold significance. First, in any spatial context, cells are exposed to multiple cues. The specification cue must be processed in this rich backdrop of signals. Furthermore, in some cases, information from two or more specification cues must be integrated to induce the appropriate response. Second, cellular response to a specification cue must take into account the temporal context. When a cell is exposed to a specification cue at a particular time in development, its response will be biased by its developmental history. For example, the cell response will be affected by its proteomic profile, which is determined by the series of gene expression programs executed up to that time. In fact, the context dependence of cell response is absolutely critical, since the same specification cue is often used in multiple places and times to guide development. Cells respond to the same cue in distinct ways by accounting for their spatial and temporal context through remarkably sophisticated signal integration mechanisms.

1.3 Specification Cues

Specification cues are signals that instruct cells to execute a particular gene expression program, and thereby propel cells to a particular fate. Classical models envisioned that spatial gradients in soluble cues may guide multicellular patterning over longer length scales [3]. Indeed, such soluble specification cues or morphogens have been identified, including four major families: fibroblast growth factor (FGF), hedgehog (Hh), wingless (Wg/Wnt), and transforming growth factor-β (TGFβ) [4]. These factors operate in a wide span of organisms including both invertebrates (*Drosophila*, *C. elegans*, and sea urchin) and vertebrates (*Xenopus*, zebrafish, mouse, and chicken).

Morphogens are signaling molecules that partition a field of cells into two or more fates [5]. They act directly to specify fates in a concentration-dependent manner (Figure 1.1). Because cells respond to the local concentration, the shape of the morphogen gradient across a field of cells dictates the pattern of cell fates. Although several factors had been long thought to act as morphogens, direct experimental evidence for spatially graded, concentration-dependent action was first demonstrated for activin, a member of the TGFβ family, that guides mesoderm induction in *Xenopus* embryos [6].

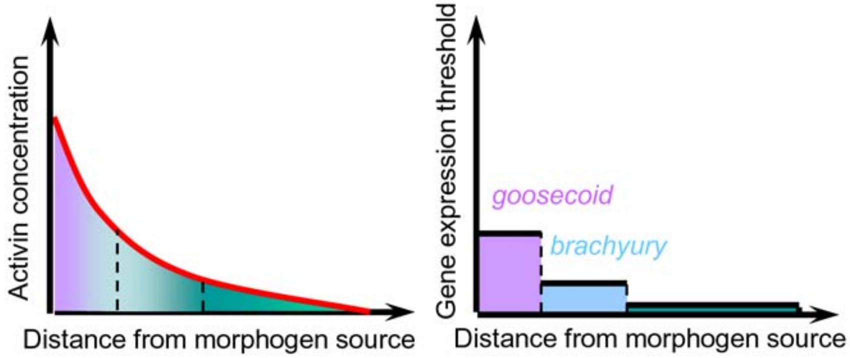

Figure 1.1. Activin concentration-dependent gene expression domains
Cells that are closest to the activin morphogen source are exposed to a high concentration of activin and express *goosecoid*. At intermediate distances, activin induces the expression of *brachyury*. Cells farthest away from morphogen source receive the least amount of morphogen and do not express either gene.

Spatial gradients are established by localized secretion of morphogen along with its transport across the cell field. The secreting source may be a single cell as in the case of LIN-3 release during *C. elegans* vulval development [7] or an array of cells as in the case of Decapentaplegic (Dpp)-mediated anteroposterior (AP) patterning of the

Drosophila wing [8]. In systems where a single cell releases the morphogen, the gradient will most likely span a short distance on the order of several cell lengths. Morphogen release from several cells can lead to gradients that span hundreds of cells lengths, although short range coverage is also possible as in Hh-initiated AP patterning in the *Drosophila* wing [9]. Importantly, morphogens need not be extracellular factors. During early stages of *Drosophila* development, the embryo is a multinuclear synctium with no cell boundaries. Gradients in maternal gene products, such as Dorsal and Bicoid, establish asymmetries in gene expression during dorsoventral (DV) and AP patterning, respectively, of the *Drosophila* embryo.

Secreted extracellular morphogens are generally expressed as transmembrane precursors that are later processed by proteases to release the soluble form [7, 10]. The mechanisms regulating morphogen release are beginning to be uncovered. Transport between intracellular compartments and retention in the endoplasmatic reticulum (ER) play a regulatory role in the release of Spitz morphogen during *Drosophila* eye development [11]. However, interesting questions remain: how are source cells synchronized to initiate (and to stop) the release of morphogen? Are such decisions autonomous or nonautonomous? Synchronous release may involve cell–cell communication, a plausible mechanism if the secreting source were a small group of cells. Such coordinated secretion would be more difficult if the secreting source were a large group of cells. In this case, a relay mechanism may provide synchronicity and the desired amplification. For example a long range gradient in Dpp morphogen patterns the *Drosophila* wing. This gradient is set up by a shorter range gradient in Hh [12].

Once secreted, the morphogen must be transported across the cell field to establish a gradient. Several genetics studies revealed that endocytosis—the internalization of morphogen-bound receptor by the cell—plays a key role in establishing morphogen gradients [13, 14]. These observations suggested that morphogen transport may occur by an active, cell-assisted process labeled transcytosis (Figure 1.2). In this process, morphogen-bound receptors are endocytosed and then exocytosed or brought back to the cell surface. Exocytosed complexes dissociate and release the morphogen. If the reemergence of the internalized morphogen is isotropic, transcytosis-mediated morphogen transport may be characterized by an effective diffusion coefficient [15]. In fact, it has been suggested that passive diffusion may not be well suited to establish steady-state morphogen gradients [16].

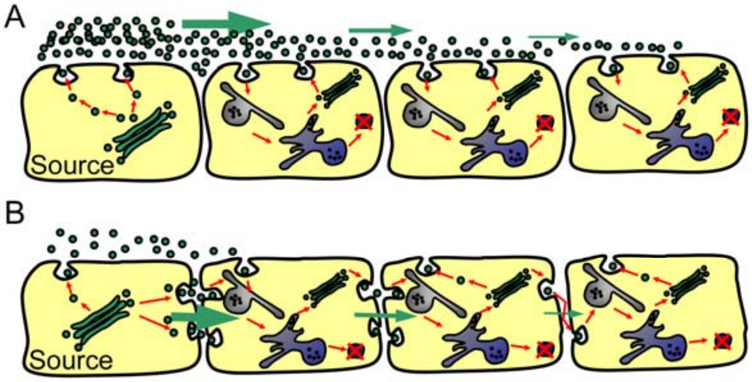

Figure 1.2. Mechanisms of morphogen transport
(A) Transport by passive diffusion entails release of morphogen from the Golgi (green) in the extracellular space by the source cell (left) and random walk of molecules away from the source. The morphogen can be endocytosed and transported through early endosomes (gray) to late endosomes (blue-gray) and recycled to Golgi or degraded in lysosomes (blue). (B) Transport by transcytosis consists of rounds of endocytosis and exocytosis by the cells in the field.

However, an integrative analysis of diffusion-mediated transport alongside key biochemical pathways revealed that diffusive transport can establish steady-state morphogen gradients, provided there are degradation sinks for the morphogen [17]. In the absence of morphogen degradation, an ever-increasing morphogen concentration will result in uniform occupancy of target receptors at steady state. However, in the presence of morphogen sinks, a steady-state gradient in receptor occupancy will form in a diffusion-based transport model. Indeed, receptor-mediated endocytosis itself promotes morphogen degradation [13, 18]. Thus, the requirement for endocytosis to establish morphogen gradients is entirely consistent with diffusive transport.

Furthermore, the diffusion/endocytosis model may be physically more plausible than transcytosis, since the latter may require that certain cellular processes occur at nonphysiological rates. For example, the formation of a steady-state gradient on the timescale of a typical developmental process would require that morphogen be transported across a single cell on an average time scale of 100 seconds [17], seemingly unachievable considering the relatively slow kinetics of the steps involved in transcytosis: receptor association, internalization, directed transport through the cell, exocytosis, and receptor dissociation. However, it can be argued that the rates of these processes have not been measured *in vivo* where cells may be optimized to facilitate transcytosis [15]. Furthermore, the diffusion/endocytosis model is not consistent with all experimental data [19]. In cell fields where a patch of cells is deficient in endocytosis, a depression in morphogen concentration is observed adjacent to the patch on the side opposite from the secreting morphogen source. The diffusion/endocytosis model would predict that in the endocytosis-defective patch, reduced receptor degradation increases receptor expression and prevents morphogen transport, thereby producing the “shadow” effect. However, recent measurements of the receptor expression level in the endocytosis-deficient patch suggest that the increase in receptor expression is not of sufficient magnitude to explain quantitatively the shadow phenomenon [19].

In summary, an integrative analysis demonstrates that diffusion is entirely capable of establishing morphogen gradients in an endocytosis-dependent fashion, although other mechanisms such as transcytosis may play a concomitant role. Model predictions about morphogen transport may be validated by comparison to direct measurements of morphogen gradients. Gradients have been directly observed *in vivo* using green fluorescent protein (GFP) fusion constructs. This approach has been used to study the formation of the Dpp and Wg gradients in *Drosophila* during the anterior-posterior patterning of wing discs and during embryonic development, respectively [13, 20, 21]. Mathematical models have been constructed to explain the mechanisms of Dpp gradient formation and the role of receptors in shaping this gradient [19, 22].

However, in most cases, direct observation of the gradient has been hampered by difficulty in expressing GFP-fused morphogens or in using antibodies to detect low concentrations of morphogens [19, 23]. In these cases, the intracellular expression of a gene target is measured as an indirect monitor of the extracellular morphogen. For example, during *C. elegans* vulval development, the gradient in an EGF-like soluble factor (LIN-3) has been observed indirectly from the graded activity of a reporter of the

LIN-3 target gene, *egl-17* [24]. Such studies offer important *qualitative* confirmation of the morphogen gradient, but do not provide key quantitative information, such as the steepness of the steady-state gradient.

A gradient that is too shallow or too steep would not be biologically useful. A metric of gradient steepness is the ratio L/λ where λ is the characteristic decay length scale of the morphogen gradient and L is the length of the field of cells to be patterned [25]. A biologically useful gradient would have a steepness characterized by $L/\lambda = 1$. Shvartsman and colleagues recently described an elegant systems approach to infer quantitatively the steady-state gradient in the morphogen Gurken in the *Drosophila* egg chamber [26]. Using molecular genetics, the expression level of the Gurken receptor (EGFR) was manipulated in order to alter the Gurken morphogen gradient. Since the gradient could not be directly measured, its effect on the expression of the target gene *pipe* was quantified using imaging techniques. This quantitative data set that related EGFR expression level to the spatial boundaries of *pipe* expression was fit to a systems-scale model of Gurken gradient formation and signaling. This analysis revealed that the steady-state Gurken gradient is characterized by a L/λ value of 2.7. This model-based estimation of the parameter L/λ provides complete information about the full, nonlinear shape of the Gurken gradient and offers intriguing insight on how sensitive downstream gene expression must be to Gurken concentration. For example, a significant change in gene expression program is observed at a boundary where the Gurken gradient changes by only threefold, suggesting a remarkable switchlike sensitivity of these cells to Gurken concentration.

This type of ultrasensitivity to morphogen concentration would seem to suggest that even mild fluctuations in gradient formation would significantly perturb developmental patterning. Indeed, it is expected that a simple transport model involving secretion, diffusion and degradation would yield gradients that are highly sensitive to variations in parameters, such as temperature and the secretion rate [25]. In some cases, additional mechanisms are employed to buffer morphogen gradient formation against these fluctuations. For example, elevations in the morphogen secretion rate are buffered by a feedback loop during AP patterning of *Drosophila* wing [27]. Here, the Hh morphogen induces localized expression of its receptor Ptc, which in turn sequesters and directs Hh to endocytic degradation. This negative feedback loop is a robust mechanism that limits the morphogen from reaching distant cells in the event of elevated morphogen secretion.

Yet, in other systems, the steady-state gradient is not robust to variations in temperature, ligand secretion rates, or geometrical variations [25, 28]. The Bicoid gradient that patterns *Drosophila* embryo along anterior-posterior axis shows an embryo-to-embryo variability in its diffusion length of 5% of embryo length. Interestingly, the expression of the downstream gene target Hunchback (Hb) is robust to these fluctuations. Instead of exhibiting fluctuations in the position of Hb expression boundary of 7% of embryo length (about 7 cell diameters), the value expected based on the above variability in the Bicoid gradient, embryos show only 1% variability. Thus, in some systems, robustness may be conferred not at the level of gradient formation, but by the mechanisms involved in perceiving and interpreting the specification cues.

1.4 Quantitative Signal Processing and Integration

Upon receiving a specification cue, cells must choose a fate that precisely accounts for (a) the quantitative nature of the signal, (b) the spatial context that may include other environmental cues, and (c) the cell's developmental history. Intracellular molecular networks achieve this quantitative signal processing and integration of spatial and temporal context.

The first step in processing graded levels of extracellular specification cues involves their detection by cell surface receptors. The cells must then interpret this quantitative information from its receptors to choose between distinct fates. The MAP kinase pathway is a common signaling "protocol" used across a wide range of developmental systems [29-31] and performs with quantitative properties that would be desirable in a developmental context. Foremost, the MAP kinase cascade has been shown to convert a graded stimulus into a digital output, a feature that has clear implications for converting a spatial morphogen gradient into a discrete pattern of cell responses (Figure 1.1). While some of this switchlike behavior is due to the cascade structure of the MAP kinase module, the dominant contribution is provided by positive feedback [32]. In *Xenopus* oocyte extracts, MAP kinase activity increases the expression of Mos, an upstream element in the MAP kinase activation pathway. This positive feedback yields a switchlike response to a graded stimulus, and inhibition of protein synthesis ablates the upregulation of Mos and results in a graded output.

When the positive feedback is of sufficient magnitude, the MAP kinase pathway encodes another attractive feature for development – irreversibility (Figure 1.3). Upon transient stimulation with progesterone, the *Xenopus* oocyte irreversibly specifies from the immature to mature state [33]. The MAP kinase pathway mediates this irreversible specification. The positive feedback loop in the MAP kinase module acts in concert with a second signaling module that also contains a positive feedback loop. The combined effect is that the progesterone stimulus activates maturation, and even upon removal of the stimulus, the cell remains committed to that fate.

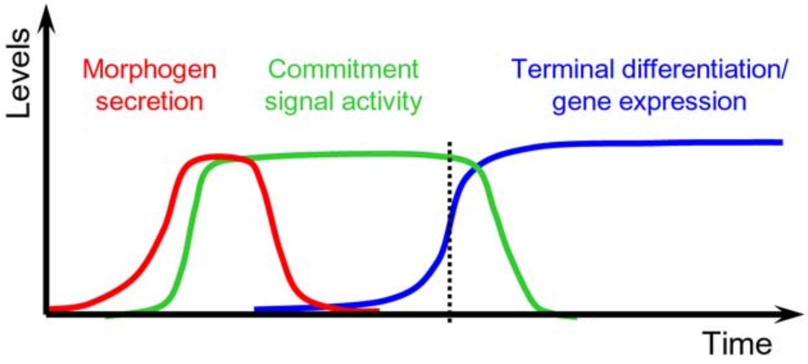

Figure 1.3. Transient signals and the irreversibility of commitment and cell fate execution
Specification cues such as morphogens (red) are secreted only transiently. This transient cue activates intracellular signals (green) that commit cells to a fate. These intermediate commitment signals must be irreversible on the short timescale during which the specification cue may subside. Over longer timescales and once past the point of commitment (vertical dotted line), the commitment signals must also dissipate, since intracellular signaling pathways, such as the MAP kinase cascade, are often reused in multiple contexts. Unlike the specification cue and the commitment signal, the expression of terminal differentiation genes (blue) associated with a specific cell fate are expressed irreversibly.

Specification cues presented to cells during development are present only transiently, long enough for the cell to commit to a fate, but short enough to prepare the system to potentially re-use the cue for later developmental steps. For example, in *C.*

elegans, the EGF-like morphogen LIN-3 is secreted by the anchor cell to stimulate vulval precursor cell specification [7]; later, the descendants of vulval precursor cells release LIN-3 toward the anchor cell to induce vulval-uterine attachment [34]. Since cues are only transient, irreversible cell commitment to execute particular fates is critical.

An important observation is that even intermediate signals, such as MAP kinase, are re-used. Thus, even though intermediate signals may be irreversible on the timescale of fate commitment, they too must decay back to a basal level to be available for the next round of specification cues. We hypothesize that this reversibility of intermediate commitment signals over longer time scales is achieved by deactivating the positive feedback pathways. However, it should be noted that fate execution itself cannot be reversible. Indeed, if the fate is cell division or death, the condition of irreversibility is obviously satisfied. However, if fate execution involves the expression of specific genes, mechanisms must be put in place to maintain that expression once the specification cue and intermediate commitment signals have dissipated. Positive feedback loops at the level of gene regulation may be involved.

Notably, a conversion from an analog to an irreversible, digital signal still leaves the cell with a conundrum. How do different levels of a single molecular signal, such as MAP kinase, trigger substantially distinct gene expression programs? In some systems, this quantitative decoding may occur at a point that is most proximal to gene expression: the *cis*-regulatory sequences that tune the level of transcriptional activity. During dorsoventral (DV) patterning of the *Drosophila* embryo, a gradient in the transcription factor Dorsal establishes a spatial pattern of gene expression (Figure 1.4). The *cis*-regulatory elements of gene targets like *twist* and *snail* contain low affinity binding sites for Dorsal, and these genes are expressed in the ventral-most field where Dorsal concentrations are high. Meanwhile, gene targets such as *rho* that are expressed more dorsally possess optimal Dorsal binding sites in their *cis*-regulatory elements. These higher affinity sites compensate for the lower Dorsal concentrations in that region. In fact, the number and quality of Dorsal binding sites on *cis*-regulatory elements strongly correlates with the pattern of dorsoventral gene expression across four divergent species of *Drosophilids* [35].

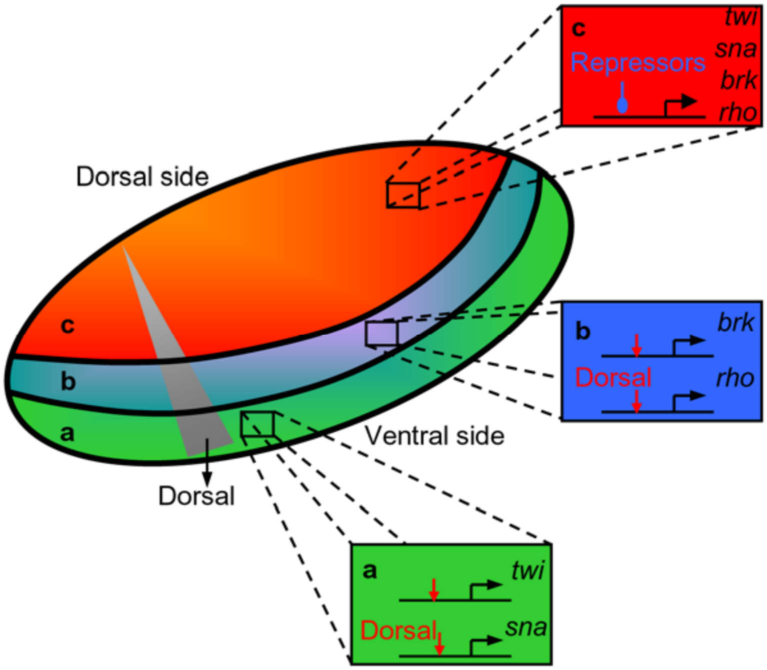

Figure 1.4. Dorsoventral patterning in *Drosophila*
A gradient in transcription factor Dorsal patterns the *Drosophila* embryo along the dorsoventral axis. The genes *twi* and *sna* with low affinity sites are active only in the ventral-most region (a) where the Dorsal concentration is highest. In the adjacent region (b) with intermediate Dorsal concentrations, *rho* and *brk* are expressed from optimal Dorsal binding sites. In the dorsal most region (c), the presence of repressors and the low concentration of Dorsal prevent activation of any of these genes.

These findings strongly suggest a model where the binding affinity of transcriptional activators to gene targets sets the threshold of specification signal needed to initiate gene expression. Genes with low affinity transcription factor binding sites may be expressed only if the specification signal is sufficiently high. Meanwhile, genes possessing high affinity binding sites would be responsive even if the specification signal were low. However, how do these high affinity binding sites remain unresponsive in regions where the specification signal is high? This additional quantitative selectivity is also prescribed by *cis*-regulatory elements, but via a mechanism unrelated to binding affinity for transcription factors. *Cis*-regulatory elements contain binding sites for multiple transcription factors, some activators and others inhibitors of gene expression. Combinatorial processing of these multiple inputs determines the net level of gene expression.

Such combinatorial processing of multiple inputs plays a key role in *Drosophila* DV patterning. As described above, the gene target *snail* contains low affinity binding sites for Dorsal and is expressed only in the ventral-most region where Dorsal concentration is highest. Interestingly, *snail* encodes a transcriptional repressor that binds *cis*-regulatory elements of other gene targets of Dorsal, including *rho*. Hence, Snail represses *rho* expression in the ventral-most region despite the high concentrations of Dorsal. Meanwhile, in the adjacent region, the concentration of Dorsal and Snail diminish. Here, *rho* is expressed because of its high affinity binding sites for Dorsal, while the lower concentration of Snail renders its repression less effective.

In this manner, *cis*-regulatory elements serve as crucial points of signal integration. Significant advances have been made in uncovering the network of transcription factors and the *cis*-regulatory elements on which they act. Such gene regulatory networks have been delineated for endomesoderm specification in sea urchin, dorsal-ventral axis patterning in *Drosophila*, vulva differentiation in *C. elegans* , and mesoderm specification in *Xenopus* (reviewed by [36, 37]). A key consideration, however, is that each *cis*-regulatory element or node in this network is not merely a connection for multiple inputs, but is a quantitative processor. The concentrations of input transcription factors are detected by the affinity and number of sites on the node. The relative amounts of activators and repressors are also part of the calculus. These quantitative aspects of the input then determine the extent of output, i.e., gene transcriptional activity.

The quantitative signal processing and integration that occur at the *cis*-regulatory modules provide not only spatial, but also temporal context. During early development of sea urchin, the *endo-16* gene [38] is expressed in the entire vegetal plate, i.e., progeny of cells derived from the veg_2 blastomeres. Later in development, its expression further increases in endoderm and future archenteron, while decaying back to basal level in veg_2 progeny cells that will become mesoderm. Throughout this time, the gene is continually repressed in micromeres or veg_1 progeny cells. In each of these spatial and temporal contexts, *endo-16* is repressed or expressed at different levels because different panels of transcription factors act on its *cis*-regulatory modules. What is the mechanistic basis for having distinct panels of transcription factors in these various contexts? The answer is a recursive one. At an earlier stage, each panel of transcription factors was expressed as dictated by their own *cis*-regulatory elements. Thus, the history of genes that were expressed in a particular cell encodes its temporal context, thereby priming the cell to respond appropriately to its current specification cues.

This cascade of gene expression events is not a simple linear pathway, but rather a gene regulatory network. The genes and the associated *cis*-regulatory elements that comprise these genetic circuits have been elucidated for a wide range of developmental contexts [37]. However, the quantitative calculations that occur at each *cis*-regulatory element remain to be elucidated. Such quantitative insight would enable the development of mathematical models of these networks. Such models can allow us to explore the capabilities of the network beyond the developmental context from which they were formulated. Indeed, development may not exhaustively cover all the contexts to which the *cis*-regulatory module of each gene responds. Analyzing the performance of *cis*-regulatory modules under developmentally unachievable contexts would offer a method to explore potential disease states or synthetic/engineering objectives.

But, one critical challenge is to develop models that not only track biochemical signals in time and space, but also predict what the actual cell fate decisions and patterns will be. Such models could explore the connection between network structure and phenotypes that are typically scored in genetics experiments. In addition, these models could provide the foundation for computationally exploring phenotypic diversity that may emerge from modifications to the underlying network. This thesis describes significant steps to address these computational challenges in developmental and evolutionary biology.

1.5 Vulva Development in *C. elegans*

The nematode *Caenorhabditis elegans* has been established as a model organism to study genetics of development since the pioneering studies led by Sydney Brenner in the 1970s [39]. It is suitable for laboratory culture and experimentation because of its self-breeding ability, short life span (about two weeks of development and senescence) and ease of genetic manipulation. Moreover, its transparent body allows visualization of individual cells by Nomarski optics. The 1 mm long worm has 959 somatic cells that derive from the fertilized egg with precise invariant lineages [40]. It is the first multicellular organism to have its genome sequenced [41].

Development of the vulva in *C. elegans* is a well-established model for studying cell patterning [42]. Over the past decades, genetics experiments have allowed inference of the molecular mechanisms guiding vulval patterning. The vulva is derived from a linear array of six vulva precursor cells (P3-8.p) [40], aligned along the antero-posterior axis of the body (Figure 1.5). These cells can adopt three fates: primary (1°), secondary (2°), and tertiary (3°). Only the first two fates are vulval fates, i.e., if adopted by a cell, that cell will be the ancestor of cells that ultimately form the vulva. While all six cells have the potential to adopt vulval fates [43], only three cells (P5-7.p) do so in wild-type worms.

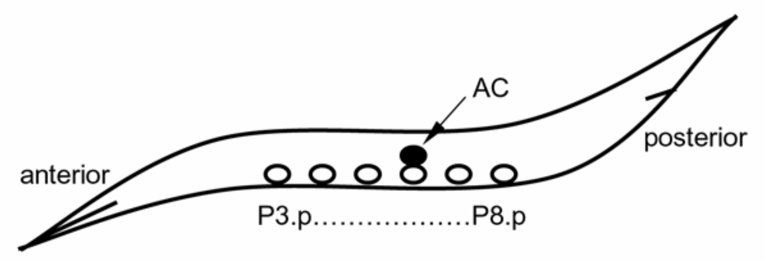

Figure 1.5. Position of vulva precursor cells along *C. elegans* body
The vulva precursor cells (P3-8.p) are aligned along the antero-posterior axis of the body. Upon receiving the LIN-3 stimulus from the anchor cell (AC), the centrally located cells P5-7.p start to divide and differentiate into the twenty-two cells that ultimately form the vulva.

Patterning of the vulva starts when EGF-like factor LIN-3 is released by the centrally positioned anchor cell (AC) (Figure 1.5 and Figure 1.6) [7]. The factor is perceived by the vulva precursor cells in a graded fashion and triggers activity of the Ras pathway [30], leading to the activation of MPK-1, the *C. elegans* MAP kinase. The MAP kinase inductive signaling in a particular cell leads to expression of ligands for the receptor LIN-12 [44] in that cell, which in turn activates LIN-12 lateral signaling in the neighboring cells. These two signals are further coupled together, as inductive signaling enhances LIN-12 endocytosis and degradation in the same cell [45], while lateral signaling transcribes genes encoding phosphatases that deactivate components of the Ras pathway [46]. Fates (1°, 2°, or 3°) are determined by the balance of the inductive and lateral biochemical signals present in a cell. Cells at high inductive and low lateral signaling adopt the 1° fate, cells at low inductive and high lateral signaling adopt the 2° fate, and cells with low signaling levels in both pathways adopt the 3° fate.

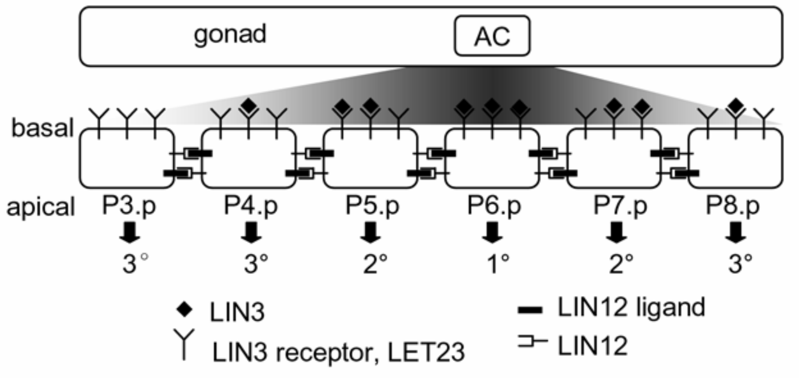

Figure 1.6. Wild-type patterning of *C. elegans* vulva
The anchor cell (AC) stimulates the vulva precursor cells Pn.p with LIN-3 in a graded manner. These cells laterally interact with one another through LIN-12 pathway. Integration of signaling from LIN-3 receptor LET-23 and LIN-12 receptor results in the wild-type pattern of differentiation 3°3°2°1°2°3°.

In this system, we focused on quantitative issues concerning the coupled network topology of inductive and lateral signaling (Chapter 2) and the patterns of cell fates that could emerge from this network when it is quantitatively perturbed (Chapter 4). Computational analysis of this molecular network as detailed in Chapter 2 reveals that cell–cell coupling amplifies the perception of the LIN-3 gradient [47]. Thus, a gradient in LIN-3 concentration produces an even steeper difference in LIN-3-mediated intracellular signals between adjoining cells. Such gradient amplification may be particularly important in converting a shallow, graded morphogen signal into a spatial pattern of digital choices suitable for robust fate determination. Variation of interaction strength among the components of the network as detailed in Chapter 4 is able to predict mutant phenotypes of cell patterns that were observed in genetics experiments. Our computational framework offers opportunities for understanding cellular fate decisions based on biochemical signals in other systems (for example cell fate specification in the immune system or cell patterning in tissue engineering applications) and for understanding the quantitative diversification occurring during evolution of closely related species with similar molecular network topologies. Preliminary experimental work was conducted to establish systems and methods to begin to validate the model predictions made in Chapter 2. These are presented in Chapter 3. Finally, future directions will be discussed in Chapter 5.

1.6 References

1. Hanahan, D. and R.A. Weinberg, *The hallmarks of cancer.* Cell, 2000. **100**(1): p. 57-70.
2. Davidson, E.H., *Later embryogenesis: regulatory circuitry in morphogenetic fields.* Development, 1993. **118**(3): p. 665-90.
3. Crick, F., *Diffusion in embryogenesis.* Nature, 1970. **225**(5231): p. 420-2.
4. Anderson, K.V. and P.W. Ingham, *The transformation of the model organism: a decade of developmental genetics.* Nat Genet, 2003. **33 Suppl**: p. 285-93.
5. Tabata, T. and Y. Takei, *Morphogens, their identification and regulation.* Development, 2004. **131**(4): p. 703-12.
6. Gurdon, J.B., et al., *Activin signalling and response to a morphogen gradient.* Nature, 1994. **371**(6497): p. 487-92.
7. Hill, R.J. and P.W. Sternberg, *The gene lin-3 encodes an inductive signal for vulval development in C. elegans.* Nature, 1992. **358**(6386): p. 470-6.
8. Lecuit, T., et al., *Two distinct mechanisms for long-range patterning by Decapentaplegic in the Drosophila wing.* Nature, 1996. **381**(6581): p. 387-93.
9. Tabata, T. and T.B. Kornberg, *Hedgehog is a signaling protein with a key role in patterning Drosophila imaginal discs.* Cell, 1994. **76**(1): p. 89-102.
10. Lee, J.R., et al., *Regulated intracellular ligand transport and proteolysis control EGF signal activation in Drosophila.* Cell, 2001. **107**(2): p. 161-71.
11. Schlesinger, A., et al., *Small wing PLCgamma is required for ER retention of cleaved Spitz during eye development in Drosophila.* Dev Cell, 2004. **7**(4): p. 535-45.
12. Strigini, M. and S.M. Cohen, *Formation of morphogen gradients in the Drosophila wing.* Semin Cell Dev Biol, 1999. **10**(3): p. 335-44.
13. Entchev, E.V., A. Schwabedissen, and M. Gonzalez-Gaitan, *Gradient formation of the TGF-beta homolog Dpp.* Cell, 2000. **103**(6): p. 981-91.
14. Dubois, L., et al., *Regulated endocytic routing modulates wingless signaling in Drosophila embryos.* Cell, 2001. **105**(5): p. 613-24.
15. Vincent, J.P. and L. Dubois, *Morphogen transport along epithelia, an integrated trafficking problem.* Dev Cell, 2002. **3**(5): p. 615-23.
16. Kerszberg, M. and L. Wolpert, *Mechanisms for positional signalling by morphogen transport: a theoretical study.* J Theor Biol, 1998. **191**(1): p. 103-14.
17. Lander, A.D., Q. Nie, and F.Y. Wan, *Do morphogen gradients arise by diffusion?* Dev Cell, 2002. **2**(6): p. 785-96.

18. Gonzalez-Gaitan, M., *Endocytic trafficking during Drosophila development.* Mech Dev, 2003. **120**(11): p. 1265-82.
19. Kruse, K., et al., *Dpp gradient formation by dynamin-dependent endocytosis: receptor trafficking and the diffusion model.* Development, 2004. **131**(19): p. 4843-56.
20. Teleman, A.A. and S.M. Cohen, *Dpp gradient formation in the Drosophila wing imaginal disc.* Cell, 2000. **103**(6): p. 971-80.
21. Pfeiffer, S., et al., *Producing cells retain and recycle Wingless in Drosophila embryos.* Curr Biol, 2002. **12**(11): p. 957-62.
22. Eldar, A. and N. Barkai, *Interpreting clone-mediated perturbations of morphogen profiles.* Dev Biol, 2005. **278**(1): p. 203-7.
23. Belenkaya, T.Y., et al., *Drosophila Dpp morphogen movement is independent of dynamin-mediated endocytosis but regulated by the glypican members of heparan sulfate proteoglycans.* Cell, 2004. **119**(2): p. 231-44.
24. Yoo, A.S., C. Bais, and I. Greenwald, *Crosstalk between the EGFR and LIN-12/Notch pathways in C. elegans vulval development.* Science, 2004. **303**(5658): p. 663-6.
25. Houchmandzadeh, B., E. Wieschaus, and S. Leibler, *Establishment of developmental precision and proportions in the early Drosophila embryo.* Nature, 2002. **415**(6873): p. 798-802.
26. Goentoro, L.A., et al., *Quantifying the Gurken morphogen gradient in Drosophila oogenesis.* Dev Cell, 2006. **11**(2): p. 263-72.
27. Eldar, A., et al., *Self-enhanced ligand degradation underlies robustness of morphogen gradients.* Dev Cell, 2003. **5**(4): p. 635-46.
28. Houchmandzadeh, B., E. Wieschaus, and S. Leibler, *Precise domain specification in the developing Drosophila embryo.* Phys Rev E Stat Nonlin Soft Matter Phys, 2005. **72**(6 Pt 1): p. 061920.
29. Voas, M.G. and I. Rebay, *Signal integration during development: insights from the Drosophila eye.* Dev Dyn, 2004. **229**(1): p. 162-75.
30. Kornfeld, K., *Vulval development in Caenorhabditis elegans.* Trends Genet, 1997. **13**(2): p. 55-61.
31. Nilson, L.A. and T. Schupbach, *EGF receptor signaling in Drosophila oogenesis.* Curr Top Dev Biol, 1999. **44**: p. 203-43.
32. Ferrell, J.E., Jr., *Building a cellular switch: more lessons from a good egg.* Bioessays, 1999. **21**: p. 866-870.
33. Xiong, W. and J.E. Ferrell, Jr., *A positive-feedback-based bistable 'memory module' that governs a cell fate decision.* Nature, 2003. **426**(6965): p. 460-5.
34. Sherwood, D.R. and P.W. Sternberg, *Anchor cell invasion into the vulval epithelium in C. elegans.* Dev Cell, 2003. **5**(1): p. 21-31.
35. Papatsenko, D. and M. Levine, *Computational identification of regulatory DNAs underlying animal development.* Nat Methods, 2005. **2**(7): p. 529-34.
36. Stathopoulos, A. and M. Levine, *Genomic regulatory networks and animal development.* Dev Cell, 2005. **9**(4): p. 449-62.
37. Levine, M. and E.H. Davidson, *Gene regulatory networks for development.* Proc Natl Acad Sci U S A, 2005. **102**(14): p. 4936-42.

38. Yuh, C.H. and E.H. Davidson, *Modular cis-regulatory organization of Endo16, a gut-specific gene of the sea urchin embryo.* Development, 1996. **122**(4): p. 1069-82.
39. Brenner, S., *The genetics of Caenorhabditis elegans.* Genetics, 1974. **77**(1): p. 71-94.
40. Sulston, J.E. and H.R. Horvitz, *Post-embryonic cell lineages of the nematode, Caenorhabditis elegans.* Dev Biol, 1977. **56**(1): p. 110-56.
41. *Genome sequence of the nematode C. elegans: a platform for investigating biology.* Science, 1998. **282**(5396): p. 2012-8.
42. Sternberg, P.W. and H.R. Horvitz, *Pattern formation during vulval development in C. elegans.* Cell, 1986. **44**(5): p. 761-72.
43. Sulston, J.E. and J.G. White, *Regulation and cell autonomy during postembryonic development of Caenorhabditis elegans.* Dev Biol, 1980. **78**(2): p. 577-97.
44. Chen, N. and I. Greenwald, *The lateral signal for LIN-12/Notch in C. elegans vulval development comprises redundant secreted and transmembrane DSL proteins.* Dev Cell, 2004. **6**(2): p. 183-92.
45. Shaye, D.D. and I. Greenwald, *Endocytosis-mediated downregulation of LIN-12/Notch upon Ras activation in Caenorhabditis elegans.* Nature, 2002. **420**(6916): p. 686-90.
46. Berset, T., et al., *Notch inhibition of RAS signaling through MAP kinase phosphatase LIP-1 during C. elegans vulval development.* Science, 2001. **291**: p. 1055-1058.
47. Giurumescu, C.A., P.W. Sternberg, and A.R. Asthagiri, *Intercellular coupling amplifies fate segregation during Caenorhabditis elegans vulval development.* Proc Natl Acad Sci U S A, 2006. **103**(5): p. 1331-6.

CHAPTER 2: INTERCELLULAR COUPLING AMPLIFIES FATE SEGREGATION DURING *C. ELEGANS* VULVAL DEVELOPMENT

2.1 Abstract

During vulval development in *C. elegans*, six precursor cells acquire a spatial pattern of distinct cell fates. This process is guided by a gradient in the soluble factor, LIN-3, and by direct interactions between neighboring cells mediated by the Notch-like receptor, LIN-12. Genetic evidence has revealed that these two extracellular signals are coupled: lateral cell-cell interactions inhibit LIN-3-mediated signaling, while LIN-3 regulates the extent of lateral signaling. To elucidate the quantitative implications of this coupled network topology for cell patterning during vulval development, we developed a mathematical model of LIN-3/LIN-12-mediated signaling in the vulval precursor cell array. Our analysis reveals that coupling LIN-3 and LIN-12 amplifies cellular perception of the LIN-3 gradient and polarizes lateral signaling, both of which enhance fate segregation beyond that achievable by an uncoupled system.

2.2 Introduction

Vulval development in *C. elegans* involves the spatially coordinated commitment of vulval precursor cells (VPCs) toward distinct cell fates, labeled primary (1^o), secondary (2^o) and tertiary fates (3^o) (Figure 2.1). This patterning is guided by an epidermal growth factor (EGF)-like soluble factor LIN-3 that is produced by a centrally positioned anchor cell (AC). LIN-3 activates an EGF receptor(LET-23)-mediated signal

---

Reprinted from Proc. Natl. Acad. Sci. USA, 2006. **103**(5): p.1331-6.

transduction pathway in the VPCs that is required for 1º and 2º cell fates; in the absence of LIN-3, all VPCs assume the default, 3º fate [1].

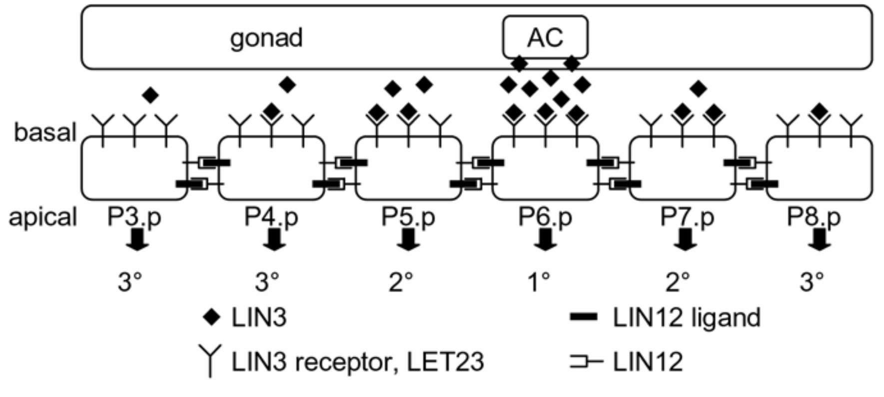

Figure 2.1. Spatial patterning of vulval precursor cells in *C. elegans*
The anchor cell (AC) in the gonad releases LIN-3 (♦), which distributes across the linear array of vulval precursor cells (P3.p–P8.p). This factor binds its receptor LET-23 (Y) on the basal surface of the precursor cells and provides an inductive signal for fate specification. The interplay between the inductive signal (LIN-3:LET-23 complexes, ⍏) and lateral coupling between neighboring cells mediated by LIN-12 (⊐–) and its ligands (▬) specifies P3.p–P8.p cells to three distinct cell fates (1º, 2º, and 3º).

The dose of LIN-3 is a critical determinant of cell fate. In animals where all VPCs but one are ablated, the intact VPC chooses a cell fate depending on its relative position to the AC: when close to the AC, the VPC chooses 1º fate, while when distal from the AC, it chooses the 3º fate. At intermediate position, the VPC chooses a 2º fate [1]. Indeed, a gradient in LIN-3 signaling has been observed indirectly *in vivo* using a sensitive reporter of LIN-3 mediated transcriptional activity [2]. These observations strongly support the notion that LIN-3 acts as a morphogen, a soluble factor whose spatial concentration gradient influences cell fate choices [3, 4].

In addition to the LIN-3 signal, direct communication between neighboring cells involving the Notch-like receptor (LIN-12) and its ligands drives cell patterning. In organisms lacking LIN-12, VPCs fail to commit to 2º fate, producing only 1º/3º cell fates [5]. Meanwhile, in mutant organisms with hyperactive inductive, LET-23–mediated signals, VPCs acquire not only 1º fates, but also 2º fates. In fact, an intriguing alternating pattern of 1º and 2º cells (e.g., 2º 1º 2º) is observed, suggesting that commitment to 1º fate forces its direct neighbors to acquire 2º fate via a lateral "inhibitory" signal [6]. These and other observations suggest a sequential model wherein LIN-3 inductive signal is essential only to promote 1º cell fate, which in turn stimulates 2º fate choice via a direct, lateral signal to its neighbors.

Resolving the relative importance of the LIN-3 gradient (morphogen model) and the lateral signal (sequential model) is challenged by the fact that these two extracellular signals are coupled through an intracellular signaling network [7]. LIN-3 binds LET-23 and produces intracellular signals via a canonical Ras-MAP kinase signaling pathway [8]. Activation of the MAP kinase, MPK-1, stimulates the production of LIN-12 ligands and the endocytosis of LIN-12 [9-11]. Thus, the inductive LIN-3 signal influences the extent to which each VPC sends out and receives lateral signal by modulating the expression of LIN-12 ligand and LIN-12, respectively. LIN-12, in turn, affects the extent to which each VPC is responsive to the inductive signal: LIN-12 stimulates the transcription of negative regulators of the LIN-3 mediated Ras signaling pathway [2, 12].

While the biochemical details of the intracellular molecular mechanisms coupling LIN-3 and LIN-12 are being elucidated, the quantitative effects of this network topology remain unclear. Because lateral signaling couples the signaling network in each VPC to that of its neighbors, it is expected to influence how each VPC responds to its local LIN-3 concentration. Conversely, the local LIN-3 concentration will impact how effectively a particular VPC receives and sends lateral signals. Here, we develop and analyze a mathematical model of LIN-3/LIN-12-mediated signaling in order to elucidate quantitatively how this network topology achieves spatially patterned cell fate specification.

2.3 Model Development

Vulval precursor cells are treated as a discrete, linear array of cells, wherein each cell (*i*) is stimulated by an inductive signal (Ind_i) corresponding to the number of LIN-3:LET-23 complexes per cell. The vector of inductive signals $\left(\mathbf{Ind} = \left\{\mathrm{Ind}_i\right\}\right)$ defines the external morphogen gradient to which the VPC array responds. In each cell, the inductive signal (Ind_i) activates the MAP kinase MPK-1, producing MPK-1^* (Figure 2.2). In turn, these active species are returned to their inactive state by the constitutive action of phosphatases (Ph).

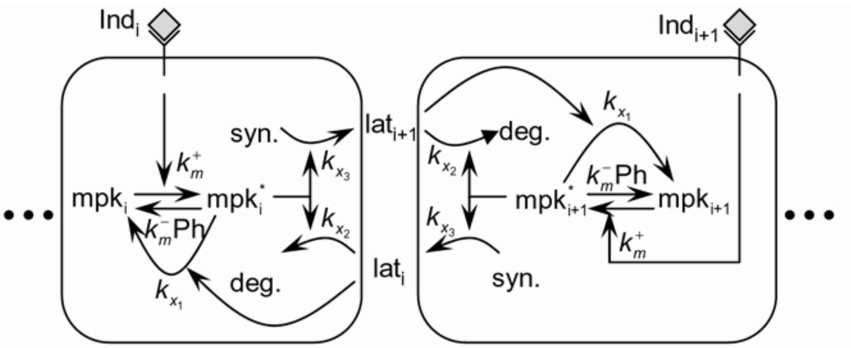

constitutive synthesis (k_n^+) and degradation (k_n^-) of lateral signals (lat$_i$) are not depicted

Figure 2.2. Model schematic
A pair of interacting cells, *i* and *i*+1, is shown; longer cell arrays are simulated by adding similar modular cells to the array. The inductive signal I_i activates MPK-1 in each cell *i* with rate constant k_m^+. Constitutive phosphatases Ph deactivate MPK-1* with rate constant k_m^-. The inductive signal upregulates the lateral signal in the neighboring cell with rate constant k_{x_3} and downregulates it in the same cell with rate constant k_{x_2}. In turn, the lateral signal in each cell deactivates MPK-1* with rate constant k_{x_1}.

In addition to constitutive deactivation, the level of MPK-1* in each cell is affected by lateral signal activity. Lateral signal activity in cell *i* (lat$_\mathrm{i}$) is received via the receptor LIN-12 and stimulates transcription of negative regulators of MPK-1. All together, the cumulative effects of inductive stimulation, constitutive deactivation and lateral signal-mediated deactivation determine the level of MPK-1* as represented by the following differential equation:

$$\frac{d\left(\mathrm{mpk}_\mathrm{i}^*\right)}{d\mathrm{t}} = k_m^+ \mathrm{Ind}_\mathrm{i}\left(\mathrm{mpk}_\mathrm{i}\right) - k_m^-\left(\mathrm{Ph}_\mathrm{T}\right)\left(\mathrm{mpk}_\mathrm{i}^*\right) - k_{x_1}\frac{\left(\mathrm{lat}_\mathrm{i}\right)^2}{K_{M_{lat}}^2 + \left(\mathrm{lat}_\mathrm{i}\right)^2}\left(\mathrm{mpk}_\mathrm{i}^*\right), \tag{2.1}$$

where Ph_T is the amount of phosphatase per cell; k_m^+ and k_m^- are the second-order rate constants for MPK-1 activation and constitutive deactivation, respectively; k_{x_1} is a rate constant for lateral signal-mediated deactivation of MPK-1*. $K_{M_{lat}}$ represents the width of the Hill function describing the transcriptional events associated with expression of MPK-1* deactivators.

The amount of lateral signal received by cell *i* ($\mathrm{lat_i}$) is determined by two MPK-1–dependent processes. First, MPK-1* stimulates the endocytic degradation of the LIN-12 receptor, thereby decreasing the reception of lateral signal. Second, active MPK-1 in neighboring cells ($\mathrm{mpk}^*_{\mathrm{i+1}}$ and $\mathrm{mpk}^*_{\mathrm{i\text{-}1}}$) stimulates the synthesis of ligands for LIN-12, thereby increasing the lateral signal into cell *i*. In addition to these MPK-1*-mediated effects, the level of lateral signal ($\mathrm{lat_i}$) is determined by constitutive synthesis and degradation.

Because little quantitative information is available on the regulation of LIN-12 endocytosis and LIN-12 binding to its ligands within the intercellular space, we sought to capture the salient features of LIN-12 regulation. Thus, the model tracks the level of LIN-12 complexes with its ligands as a lumped measure of lateral signaling as follows:

$$\frac{d\left(\mathrm{lat_i}\right)}{d\mathrm{t}} = k_n^+ - k_n^-\left(\mathrm{lat_i}\right) - k_{x_2}\left(\mathrm{mpk}^*_{\mathrm{i}}\right)\left(\mathrm{lat_i}\right) + k_{x_3}\frac{\left(\dfrac{\mathrm{mpk}^*_{\mathrm{i+1}}}{\nu_{\mathrm{i+1}}}+\dfrac{\mathrm{mpk}^*_{\mathrm{i-1}}}{\nu_{\mathrm{i-1}}}\right)^2}{K^2_{M_{ind}}+\left(\dfrac{\mathrm{mpk}^*_{\mathrm{i+1}}}{\nu_{\mathrm{i+1}}}+\dfrac{\mathrm{mpk}^*_{\mathrm{i-1}}}{\nu_{\mathrm{i-1}}}\right)^2}, \qquad (2.2)$$

where k_n^+ and k_n^- are the constitutive rate constants of lateral signal generation and degradation, k_{x_2} is the rate constant for MPK-1*-mediated downregulation of lateral signaling by enhanced endocytosis of LIN-12, k_{x_3} is the rate constant for lateral signal transmission into cell *i* by its neighbors, and $K_{M_{ind}}$ represents the width of the Hill function describing the generation of lateral signal by MPK-1*; $\nu_{\mathrm{i-1}}$ and $\nu_{\mathrm{i+1}}$ are the number of neighbors for cell *i−1* and *i+1*, respectively. For a linear array, the value of υ_i is either 1 or 2. In Equation 2.1 and Equation 2.2, we have assumed that transcriptional regulation occurs in a cooperative manner with a Hill coefficient (η_H) of 2; however, eliminating this cooperativity ($\eta_H = 1$) does not affect the trends predicted by the model.

It is meaningful to introduce the following substitutions:

$$I_i = \frac{\mathrm{Ind_i}}{\mathrm{Ind^m}}, \quad m_i = \frac{\mathrm{mpk_i^*}}{\mathrm{mpk_T}}, \quad l_i = \frac{\mathrm{lat_i}}{k_{x_3}/\left(k_{x_2}\,\mathrm{mpk_T}\right)}, \quad \tau = k_m^- \mathrm{Ph_T}\, t, \tag{2.3}$$

where $\mathrm{Ind^m}$ is the maximum number of morphogen:morphogen-receptor complexes per cell, $\mathrm{mpk_T}$ is the total number of MPK-1 molecules per cell, and *t* is dimensional time. Incorporating these substitutions in Equation 2.1 and Equation 2.2 yields the following differential equations:

$$\begin{aligned} \frac{dm_i}{d\tau} &= \mu I_i\left(1-m_i\right) - m_i - \chi m_i \frac{l_i^2}{\kappa_l^2 + l_i^2}, \\ \frac{dl_i}{d\tau} &= \lambda_s - \lambda_d l_i - \psi^{-1} m_i l_i + \psi^{-1} \frac{\left(\dfrac{m_{i+1}}{\nu_{i+1}} + \dfrac{m_{i-1}}{\nu_{i-1}}\right)^2}{\kappa_m^2 + \left(\dfrac{m_{i+1}}{\nu_{i+1}} + \dfrac{m_{i-1}}{\nu_{i-1}}\right)^2}, \end{aligned} \tag{2.4}$$

where the dimensionless parameters μ, χ, $\kappa_{M_{lat}}$, $\kappa_{M_{ind}}$, λ_s, λ_d, and ψ are defined as follows:

$$\begin{aligned} &\chi = \frac{k_{x_1}}{k_m^-\left(\mathrm{Ph_T}\right)}, \quad && \lambda_s = \frac{k_n^+ / \left[k_{x_3}/\left(k_{x_2}\,\mathrm{mpk_T}\right)\right]}{k_m^-\left(\mathrm{Ph_T}\right)}, \quad && \kappa_l = \frac{K_{M_{lat}}}{k_{x_3}/\left(k_{x_2}\,\mathrm{mpk_T}\right)}, \\ &\psi = \frac{k_m^-\left(\mathrm{Ph_T}\right)}{k_{x_2}\left(\mathrm{mpk_T}\right)}, && \lambda_d = \frac{k_n^-}{k_m^-\left(\mathrm{Ph_T}\right)}, && \kappa_m = \frac{K_{M_{ind}}}{\mathrm{mpk_T}}, \\ &\mu = \frac{k_m^+\left(\mathrm{Ind^m}\right)}{k_m^-\left(\mathrm{Ph_T}\right)}. \end{aligned} \tag{2.5}$$

Two dimensionless groups of particular importance are χ and ψ, which together offer a gauge of intercellular coupling. The first parameter χ is a ratio of the timescale for constitutive deactivation of MPK-1* to the time scale of lateral signal-mediated deactivation of MPK-1*. Large values for χ indicate that constitutive deactivation of MPK-1* occurs much slower than lateral signal-mediated deactivation. For example, a value of $\chi = 10$ indicates that when lateral signaling is maximal, lateral signal-mediated deactivation of MPK-1* occurs at a rate that is 10-fold greater than rate of deactivation mediated constitutive pathways. The second parameter ψ is a ratio of the time scale of MPK-1*-mediated downregulation of lateral signal to the time scale of MPK-1* deactivation by phosphatases. Thus, large values for ψ imply that a given MPK-1* molecule is more likely to be deactivated before contributing to the downregulation of lateral signal. Thus, large ψ indicates that each cell is more susceptible to lateral effects. Reference values for these and other dimensionless parameters were chosen as outlined in Section 2.7.

The outlined mathematical model differs significantly from a recent treatment of this system that employed a state-charts approach [13], wherein the fate of a particular VPC is decided based on the state of its neighbors using fate decision rules. These rules are high-level abstractions of the underlying logic guiding fate determination as outlined in 1989 [14]. Since then, significant advances have been made in our understanding of the intracellular signals occurring in each VPC and the molecular mechanisms by which VPCs are coupled. Our mathematical model encodes explicitly these intracellular molecular mechanisms and the coupling between VPCs, allowing a direct examination of the importance of these molecular interactions for spatial patterning of fates during *C. elegans* vulval development.

The analysis presented in this work focuses on the steady-state behavior of the model. Experiments wherein the anchor cell is ablated at different times during the fate specification process have revealed that fate specification is unaffected if the anchor cell is eliminated after a five-hour window [15, 16]. Analysis of model dynamics shows that the timescale for reaching steady state is less than five hours for reference values of parameters (data not shown). Thus, we proceed under the reasonable assumption that the steady state achieved during this time frame dictates fate specification.

2.4 Improved Gradient Perception

Two observations indicate that LIN-3 performs as a prototypical morphogen whose spatial gradient determines cell fate patterning. First, cell fate is sensitive to LIN-3 dose [1]. Second, a gradient in LIN-3 concentration has been observed indirectly *in vivo* [2]. These observations raise the question why cells seemingly guided to pattern formation by a morphogen gradient further require a lateral signaling mechanism.

To begin to address this issue, we examined how lateral coupling affects the perception of the extracellular gradient in the inductive signal LIN-3. The response of a simplified, 2-cell system to gradients in LIN-3 concentration was simulated by specifying the amount of inductive signal (I_1 and I_2) for neighboring cells (1 and 2) (Figure 2.2). To quantify how a gradient in extracellular LIN-3 concentration (I_1/I_2) is converted into a gradient in LIN-3-mediated intracellular MPK signal, we defined a gradient comparator (Q) as:

$$Q \equiv \frac{d(\ln m)}{d(\ln I)} = \frac{\ln(m_1/m_2)}{\ln(I_1/I_2)}, \tag{2.6}$$

where m_1 and m_2 are the steady state fraction of activated MPK-1 in cells 1 and 2, respectively. Note that Q is undefined when there is no gradient in input (i.e., $I_1/I_2 = 1$). When the relative spatial gradient in LIN-3 translates into exactly the same relative spatial gradient in MPK-1*, the value of Q is one. When the spatial gradient in intracellular signal is attenuated relative to the gradient in extracellular stimulus, the value of Q is less than one; in contrast, when the MPK-1* gradient is amplified relative to the extracellular LIN-3 gradient, the value of Q is greater than one.

In the absence of lateral coupling (i.e., $\chi = 0$) between neighboring cells, the gradient comparator (Q°) is given by:

$$Q^\circ = 1 - \frac{\ln\left(\dfrac{1+\mu I_1}{1+\mu I_2}\right)}{\ln\left(\dfrac{I_1}{I_2}\right)}. \tag{2.7}$$

This expression reveals two regimes of perceiving gradients in inductive signal. For sufficiently low I_1 and I_2 (specifically, $I_1 << \mu^{-1}$ and $I_2 << \mu^{-1}$), the value of Q° is nearly one. Thus, in this input domain, a gradient in extracellular signal is converted to a near equivalent gradient in intracellular signal. For relatively higher values of I_1 and I_2, Q° decreases below one, indicating that a gradient in extracellular signal is converted into a shallower gradient in intracellular signal. At these higher values of input, relative changes in input do not translate into the same relative change in intracellular signal due to a saturation of available inactive MPK-1 molecules. Figure 2.3A depicts these two regimes of gradient perception in an uncoupled system. For $I_1 = 10^{-1}$ and $I_2 = 10^{-2}$ with $\mu^{-1} = 0.05$, Q° is approximately 0.61, indicating that a 10-fold difference in input produces only a 4-fold difference in intracellular signal. Even significant differences in extracellular input result in considerably milder differences in intracellular signal, suggesting that establishing steep gradients in extracellular signal may be an inadequate mechanism for assuring distinct cell fate choices in an uncoupled system.

In contrast, a system coupled by lateral signaling displays gradient amplification. The value of the gradient comparator for a coupled system (Q^c) exceeds one in a subdomain of inductive signals (Figure 2.3B). In this region, a gradient in extracellular signal is amplified to produce a steeper gradient in intracellular MPK-1* signal. For example, maximum gradient amplification occurs at $I_1 = 0.0091$ and $I_2 = 0.0072$ (equivalent to 910 and 720 LIN-3:LET-23 complexes per cell, respectively). For this combination of inductive signals, the value of Q^c is 1.8, indicating that the ~30% difference in inductive signal is magnified to ~50% difference in intracellular MPK-1* activity between neighboring cells. For low to moderate coupling, an increase in the strength of coupling further enhances the extent of gradient amplification (Figure 2.3C). For the aforementioned combination of inductive signals, Q^c improves to 9.0 when the value of χ is increased 10-fold, corresponding to a ~725% disparity in intracellular MPK-1* activity while the extracellular signals still differ by only ~30%. These results demonstrate that lateral coupling substantially sharpens the perception of an extracellular gradient in LIN-3, overcoming an inherent limitation of uncoupled systems.

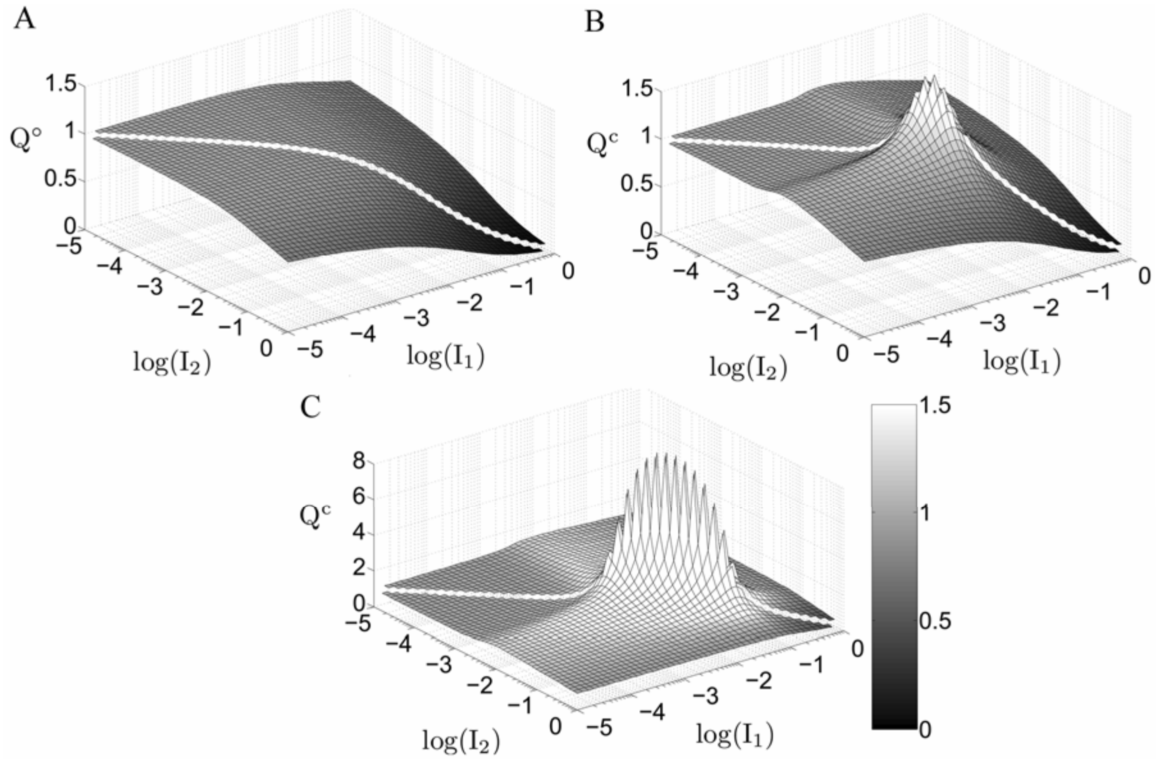

Figure 2.3. Gradient amplification in coupled systems
The value of the gradient comparator (Q) was determined for a wide range of inductive signals in a two-cell system that was uncoupled (A, $\chi = 0$) or coupled at two different strengths (B, $\chi = \chi^o$, and C, $\chi = 10\ \chi^o$). The color bar denotes the relation between the greyscale and the value of the gradient comparator. Only in the presence of lateral coupling (B and C), the value of the gradient comparator exceeds one, indicating gradient amplification in that subdomain of inductive signals. The extent of gradient amplification increases in the presence of greater lateral coupling (compare B and C).

The underlying cause of amplified perception of the LIN-3 gradient involves the establishment of a countergradient in lateral signaling. In analytical terms, in order to achieve gradient amplification (i.e., $Q^c > 1$), the following condition must hold:

$$l_2 > l_1 + \frac{\mu}{\chi}(I_1 - I_2)\frac{(\kappa_l^2 + l_1^2)(\kappa_l^2 + l_2^2)}{\kappa_l^2(l_1 + l_2)} \text{ for } I_1 > I_2 . \tag{2.8}$$

That is, the lateral signal in cell 2 must be sufficiently greater than the lateral signal in cell 1, yielding a gradient that is in direct opposition to the gradient in inductive signal ($I_1 > I_2$). Thus, as in the context of a metabolic network [17], gradient amplification requires the presence of two competing contributions, one inductive (LIN-3) and the other inhibitory (lateral signal), whose spatial profiles run counter to each other.

Even in regions of the input domain where gradient amplification does not occur ($Q^c < 1$ in Figure 2.3B and Figure 2.3C), lateral coupling still provides a robust and significant advantage over an uncoupled system in perceiving a morphogen gradient. For example, for $I_1 = 10^{-1}$ and $I_2 = 10^{-2}$, Q^c is approximately 0.85 whereas Q^o is 0.61. Thus, lateral coupling offers approximately 40% improvement in perceiving this particular gradient in extracellular signal when compared to the uncoupled system. In fact, Figure 2.4 shows that in the entire domain of inductive signals, the coupled system outperforms an uncoupled system in perceiving a gradient in inductive signal. Thus, the gradient comparator for a coupled system (Q^c) is greater than or equal to Q° for all combinations of inductive signals. In mathematical terms, we find that lateral coupling improves the perception of a gradient in inductive signal, i.e., $Q^c > Q^\circ$, if

$$l_2 > \left(\frac{1+\mu I_2}{1+\mu I_1}\right) l_1 \text{ for } I_1 > I_2 . \qquad (2.9)$$

The above criterion is less stringent than that required for gradient amplification (Equation 2.8), suggesting that it may be satisfied over a broader range of model parameters. In fact, the coupled system meets this condition, or the associated equality, for any choice of model parameter values (Section 2.8). Thus, our model predicts that lateral coupling robustly enables better, or at least equivalent, gradient perception as an uncoupled system, with the added advantage that for a subset of inductive signals meeting condition Equation 2.8, lateral coupling amplifies the external gradient. These predictions are currently being tested in wild-type (coupled) and mutant (uncoupled) worms in which the gradient in MPK-1* is monitored using an *egl-17* transcriptional reporter.

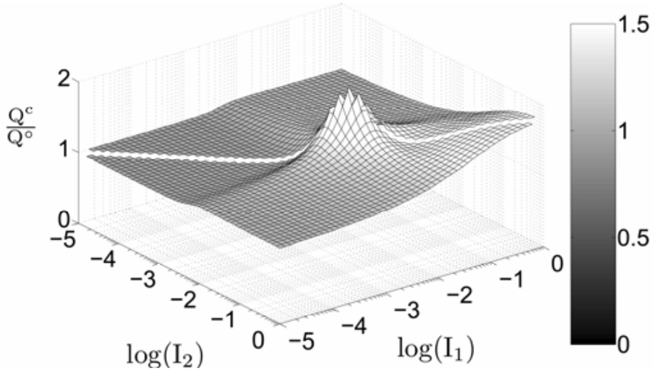

Figure 2.4. Coupled systems robustly outperform uncoupled systems in gradient sensing

The ratio of the gradient comparator for coupled systems (Q^c) to that of uncoupled systems (Q^o) is plotted for a wide range of inductive signals in a two-cell system. The lateral coupling was maintained at its reference value ($\chi = \chi^o$). The ratio Q^c:Q^o is greater than or equal to one in the entire domain of inductive signals.

What determines whether the perception of LIN-3 gradient is amplified? We have stated that an opposing gradient in lateral signal is required (condition Equation 2.8). However, even in the absence of coupling $(\chi = 0)$, a gradient in the inductive signal LIN-3 produces a countergradient in lateral signal (Figure 2.5A), owing to MPK-1-mediated regulation of lateral signaling (Figure 2.2, arrows marked k_{x_2} and k_{x_3}). In systems such as the R3-R4 fate specification in *Drosophila*, this morphogen-induced bias in lateral signal is then magnified via a feedback loop intrinsic to the Notch-Delta signaling system [18]. However, the polarization of lateral signals between neighboring cells has no consequence for the interpretation of the morphogen gradient in these systems.

Here, vulval development in *C. elegans* appears to be unique. Experimental evidence suggests that the Notch-Delta-like lateral signaling system is not self-propelled by an intrinsic positive feedback [19]. Rather, in the presence of coupling ($\chi > 0$), lateral signal deactivates MPK-1 (Figure 2.2, arrow marked k_{x_1}). Thus, a gradient in inductive LIN-3 signal sets a disparity in lateral signal (Figure 2.5A), and in a coupled system, the latter provides a disparity in the specific driving force for MPK-1* deactivation (Figure 2.5B). The net effect is that the cell receiving smaller inductive signal receives greater lateral signal and possesses greater specific activity for MPK-1* deactivation (Figure 2.5A and Figure 2.5B, cell 2). These disparities render the MPK-1 activity in this cell more sensitive to the strength of coupling. Thus, as the value of χ is increased, the MPK-1 activity decreases in the cell distal from the LIN-3 signal, while the cell proximal to the inductive signal is less affected (Figure 2.5C). However, at extremely high values of χ, lateral signal-mediated deactivation of MPK-1 dominates, even in the cell receiving the higher inductive signal (Figure 2.5B). Thus, the disparity in MPK-1 activity shrinks (Figure 2.5C), thereby eliminating the key element supporting a gradient in lateral signal. In the absence of a lateral signaling gradient at extremely high χ (Figure 2.5A), the MPK-1 gradient is determined entirely by the LIN-3 gradient, as would be the case in an uncoupled system. Thus, for extremely high χ, the perception of the LIN-3 gradient becomes equivalent to that of an uncoupled system (Figure 2.5D).

Our analysis shows that intercellular coupling via Delta-Notch signaling alters the way VPCs perceive the LIN-3 morphogen gradient. This gradient appears steeper when read as intracellular MPK-1 activity. We propose that this mechanism for enhancing the *perception* of the gradient reveals a new paradigm for spatial patterning that contrasts other developmental contexts wherein the extracellular morphogen gradient itself is steepened or otherwise re-shaped to guide patterning. Examples of the latter include the establishment of Gurken and Spitz morphogen gradients during *Drosophila* egg development [20, 21] or Hedgehog and Wingless morphogen gradients during *Drosophila* wing disc patterning [22].

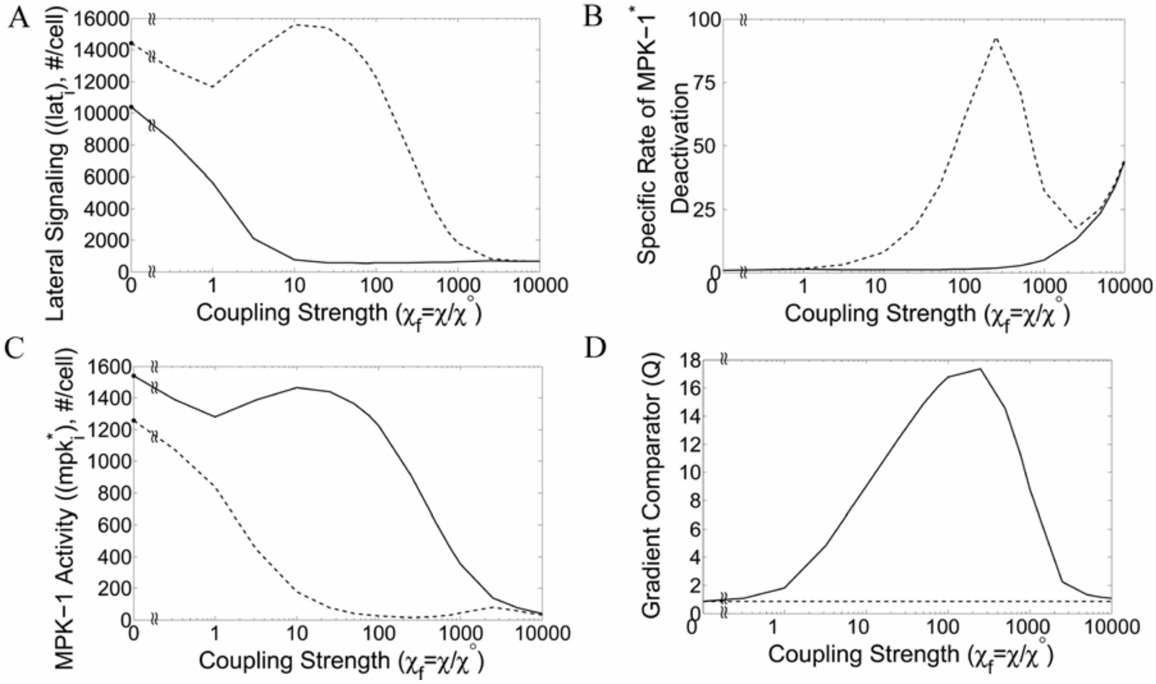

Figure 2.5. Factors contributing to coupling-mediated gradient amplification
(A) Lateral signal in cell 1 (solid) and in cell 2 (dashed) is shown as a function of lateral coupling strength. (B) The specific rate of MPK-1* deactivation is plotted as a function of coupling strength for cell 1 (solid) and 2 (dashed). The specific rate of MPK-1* deactivation is the rate of MPK-1* deactivation normalized by the amount of MPK-1*, and according to Equation 2.4, it is given by $1+\chi l_i^2/\left(\kappa_l^2+l_i^2\right)$. (C) The amount of MPK-1* in cells 1 (solid) and 2 (dashed) is plotted as a function of lateral coupling strength. (D) The value of the gradient comparator in a coupled system $Q^{c,\max}$ (solid) and uncoupled system Q° (dashed) are shown for varying lateral coupling strength. Calculations were performed at $I_1 = 0.0091$ and $I_2 = 0.0072$, the combination of inductive signals that yielded maximum Q^c when lateral coupling strength is $\chi_f = \chi/\chi^o = 1$ (Figure 2.3B).

Enhancing the gradient in intracellular perception without altering the extracellular morphogen gradient raises the possibility that one mode of perception (e.g., the MAP kinase pathway) is amplified, while other parallel signals generated by the morphogen mirror the external gradient. This differential perception may help to modularize the developmental purpose of a morphogen, while leaving parallel signals available to mediate other critical cellular/organismal functions. Indeed, such pleiotropic roles for soluble factors is not uncommon as most ligands, including EGF, often stimulate several parallel signaling pathways and concomitantly affect a range of cell functions.

2.5 Fate Plane

Our analysis demonstrates that lateral coupling enhances the perception of the extracellular LIN-3 gradient in a two-cell model system. In addition, experimental evidence suggests that lateral signaling plays a more direct role in specifying cell fates [14]. In the absence of lateral signaling, the 2° fate is not observed, although VPCs acquire 1º and 3º fates. Furthermore, in mosaic experiments where P5.p and P7.p cells lack the receptor for LIN-3, these cells still acquire 2º fate, suggesting that the lateral LIN-12-mediated signal may confer this fate independently, provided the inductive LIN-3 signal has been sufficiently quenched. These observations have led to the hypothesis that the level of active MPK-1 and the amount of LIN-12-mediated signaling together determine 1° and 2° fates, respectively. Cells with high MPK-1 activity and low lateral activity commit to a 1º fate, while cells with low MPK-1 activity and high lateral activity commit to a 2º fate. Finally, cells lacking both MPK-1 and lateral activity acquire the 3º fate.

Based on this paradigm for fate specification, we examined the role of lateral coupling in segregating VPCs on a “fate plane,” where MPK-1 activity is represented on the ordinate and LIN-12 activity is represented on the abscissa (Figure 2.6). Further, our analysis was expanded to a linear array of six cells, topologically representative of the P3.p – P8.p vulval precursor cells (Figure 2.1). The simulations were conducted with a gradient in inductive signal that decays as the square of the distance from the anchor cell, characteristic of morphogen diffusion. The maximal inductive signal ($I_{P6.p}$) was applied to the P6.p cell, the VPC most proximal to the anchor cell. Results for one side of the gradient (P3.p – P6.p cells) are presented, since the response of P7.p and P8.p cells is nearly equivalent to that of P5.p and P4.p cells, respectively (Figure 2.8).

Our analysis shows that fate specification of the VPC array requires the inductive signal provided by the anchor cell. At low morphogen levels ($I_{P6.p} = 10^{-3}$), there is no segregation of cells along the lateral signaling axis, suggesting that 2º fate specification depends upon the level of inductive signal (Figure 2.6). These results are consistent with the experimental observation that 2º fates are not observed in systems where the anchor cell is laser ablated [1]. Thus, the response to low morphogen levels was used to parameterize the threshold amount of MPK-1* (approx. $5{\cdot}10^2$/cell) and lateral signal (approx. 10^3/cell) needed for 1º and 2º fates, respectively. Therefore, cells in quadrants I, II and III are designated as 1º, 2º and 3°, respectively (Figure 2.6). Based on this parametrization of the fate plane, segregation of VPC fates is observed at higher inductive signals ($I_{P6.p} = 10^{-2}$) (Figure 2.6). This result is in agreement with LIN-3 dosage experiments, wherein increasing LIN-3 production by the anchor cell permits specification of 1° and 2° fates [4].

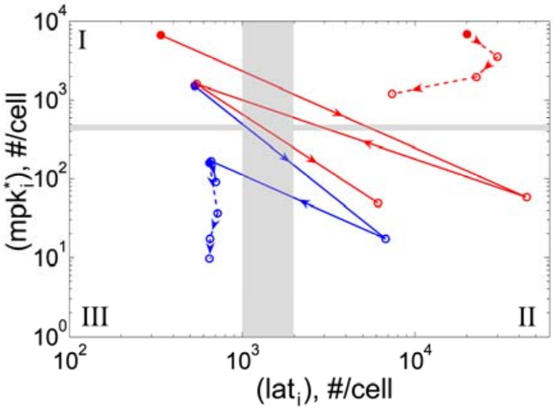

Figure 2.6. Wild-type and mutant alternating phenotypes on the fate plane
The position of P3.p-P6.p vulval pre-cursor cells is depicted on a fate plane defined by two fate-determining signals, the intracellular product of inductive signaling (mpk^*_i , *y*-axis) and the lateral signal (lat_i, *x*-axis). The wild-type cell array (blue) was coupled (χ/χ^o = 100) with $\mu = \mu^o$ and stimulated with two levels of inductive signal: $I_{P6.p} = 10^{-3}$ (dashed) or 10^{-2} (solid). The mutant cell array (red) with hyperactive inductive signaling ($\mu = 10\ \mu^o$) was stimulated with $I_{P6.p} = 10^{-2}$ and was either uncoupled ($\chi/\chi^o = 0$, dashed) or coupled ($\chi/\chi^o = 100$, solid). The filled circle denotes the P6.p cell, and the empty circles mark the remainder of the cells (P5.p, P4.p and P3.p) in the order indicated by the arrowhead. The three quadrants (I, II and III) demarcated by the gray bars denote 1°, 2° and 3° fates, respectively. The cells in the unmarked quadrant will adopt either 1° or 2° fate, but it cannot be determined which fate.

To further validate our model, we considered the striking phenotype observed among mutant animals with hyperactive LIN-3 signaling. In these mutant worms, VPCs acquire only 1° and 2° fates with a final pattern that precludes two adjoining 1° cells [23]. Thus, a common phenotype among these mutants is the alternating fate pattern 1° 2° 1° 2° 1° 2°, a sharp contrast to the wild-type 3° 3° 2° 1° 2° 3° fate pattern. This alternating pattern has been reported in mutant animals with either *lin-15(lf)* or *let-60(gf)* mutations [6, 14, 24]. The detailed molecular mechanism by which *lin-15(lf)* hyperactivates LIN-3 signaling remains unclear. In contrast, it is well established that *let-60* encodes a Ras homolog that lies upstream of MPK-1 activation [25]. Thus, we simulate the *let-60(gf)* mutation in our model by increasing the value of μ from its wild-type, reference value μ^o.

As shown in Figure 2.6, the mutant cell array ($\mu = 10\ \mu^o$) displays an alternating 1º-2º phenotype. The cells switch between a high MPK-1*/low lateral state (P8.p, P6.p, P4.p) and a low MPK-1*/high lateral state (P7.p, P5.p, P3.p) in the fate plane. Notably, a mutant cell array lacking any coupling ($\chi = 0$) does not yield an alternating phenotype. Rather, all cells reside in the high MPK-1*/high lateral signal state. Thus, our model accurately predicts the 1º 2º 1º 2º 1º 2º phenotype as observed experimentally in *let-60(gf)* mutants. Further, it demonstrates that lateral coupling is an essential mechanism to achieve this alternating phenotype.

2.6 Enhanced Segregation on the Fate Plane

Even in the absence of coupling ($\chi = 0$), it is possible to distinguish cells based on their position along the lateral signaling axis (Figure 2.7A). The P5.p cell acquires the highest lateral signal, due to its position next to the P6.p, the cell with greatest MPK-1 activity. These results suggest that the inductive signal-mediated bias of lateral signaling (Figure 2.2, arrows marked k_{x_2} and k_{x_3}) is sufficient to establish some degree of segregation of precursor cells on the fate plane.

Importantly, for coupled systems ($\chi > 0$), the extent of fate segregation is amplified (Figure 2.7A). Increasing the value of χ reduces the lateral signal in both the P6.p and P4.p cells; concomitantly, an increase in coupling strength reduces the MPK-1 activity in the P5.p cell. Suppressing the lateral signal and MPK-1 activity in P6.p and P5.p cells, respectively, polarizes these cells destined to become 1º and 2º cells, respectively.

To gauge more quantitatively the dependence of fate segregation on coupling strength, we calculated the disparity in MPK-1* and lateral signal activity between P6.p (presumptive 1º) and P5.p (presumptive 2º) cells for a wide range of inductive signal ($I_{P6.p}$) and coupling strength (χ) (Figure 2.7B and Figure 2.7C). As noted earlier, establishing differences in MPK-1* and lateral signal between P6.p and P5.p requires inductive signal. For low inductive signals ($I_{P6.p} < \sim 10^{-3}$), fate specification is not observed. Notably, for low to moderate coupling, an increase in coupling strength increases the segregation of the presumptive 1º and 2º cells with respect to both the MPK-1 signal and lateral signal (Figure 2.7B and Figure 2.7C, respectively). However, at extremely high values of χ, even the basal level of constitutive lateral signaling suppresses MPK-1 activity. Since the perception of inductive signal is required for fate specification, extremely high coupling ablates fate specification entirely. Thus, our model predicts that moderate coupling enhances the segregation of fates determined by two signals, one involving a soluble inductive factor LIN-3 and the other transmitted by lateral cell-cell interactions via Notch-Delta signaling.

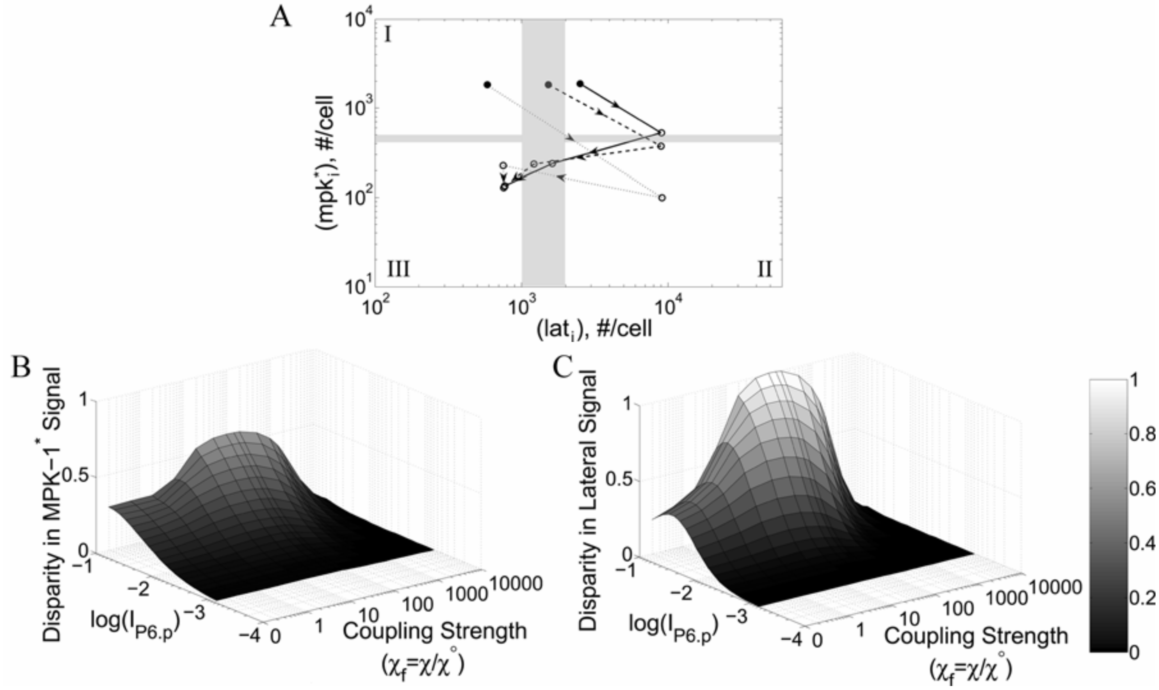

Figure 2.7. The effect of coupling on segregating two fate-determining signals in a six-cell array

(A) The position of P3.p-P6.p vulval pre-cursor cells is depicted on the fate plane. The cell array was simulated with $I_{P6.p} = 10^{-2}$. The filled circle denotes the P6.p cell, and the empty circles mark the remainder of the cells (P5.p, P4.p and P3.p) in the order indicated by the arrowhead. The lateral coupling strength was varied as $\chi_f = \chi/\chi^o = 0$ (solid), 1 (dashed) and 10 (dotted). (B and C) The disparity in MPK-1* (B) and lateral signals (C) between the presumptive 1º and 2º cells was quantified for a wide range of inductive signal and coupling strengths. The disparity in MPK-1* signal is the value of $m_{P5.p}$ subtracted from the value of $m_{P6.p}$. For the disparity in lateral signal, a similar calculation was performed with the difference now computed in the value of *lat*.

2.7 Parameter Values

Values for the dimensional model parameters were chosen based on available experimental data in other systems as outlined below (Table 2.1). The associated reference values of dimensionless parameter groups are listed in Table 2.2.

Table 2.1. Dimensional parameters of the model and their typical values

Molar units were converted to molecules per cell assuming a volume of cell of 10 pL.

Parameter	Value	Units
k_m^+	1.7×10^{-4}	$(\text{molecules/cell})^{-1}\ \text{min}^{-1}$
k_m^-	1.7×10^{-4}	$(\text{molecules/cell})^{-1}\ \text{min}^{-1}$
Ph_T	5×10^3	molecules/cell
mpk_T	10^4	molecules/cell
Ind^m	10^5	molecules/cell
k_n^+	1.3×10^2	$\text{molecules/cell} \cdot \text{min}^{-1}$
k_n^-	2×10^{-2}	min^{-1}
k_{x_1}	8.3×10^{-1}	min^{-1}
k_{x_2}	3×10^{-6}	$(\text{molecules/cell})^{-1}\ \text{min}^{-1}$
k_{x_3}	1.2×10^3	$\text{molecules/cell} \cdot \text{min}^{-1}$
$K_{M_{ind}}$	2.5×10^3	molecules/cell
$K_{M_{lat}}$	10^4	molecules/cell

Table 2.2. Dimensionless groups of the model and their reference values

Parameter	Description	Reference Value
χ	$\dfrac{\text{time scale of constitutive deactivation of mpk-1}^*}{\text{time scale of lateral signal-mediated deactivation of mpk-1}^*}$	1.0
ψ	$\dfrac{\text{time scale of constitutive deactivation of mpk-1}^*}{\text{time scale of mpk-1}^*\text{-mediated deactivation of lateral signal}}$	2.8×10^2
μ	$\dfrac{\text{time scale of constitutive deactivation of mpk-1}^*}{\text{time scale of induced activation of mpk-1}^*}$	2×10^2
λ_d	$\dfrac{\text{time scale of constitutive deactivation of mpk-1}^*}{\text{time scale of constitutive deactivation of lateral signal}}$	2.4×10^{-2}
λ_s	$\dfrac{\text{time scale of constitutive deactivation of mpk-1}^*}{\text{time scale of constitutive synthesis of a characteristic amount of lateral signal}}$	3.9×10^{-4}
κ_m	dimensionless threshold for activation of lateral signal by mpk-1*	2.5×10^{-1}
κ_l	dimensionless threshold for mpk-1* inhibition by lateral signal	2.5×10^{-1}

k_m^+ is a lumped activation constant of MPK-1 based on a more detailed biochemical mechanism of MAPK activation [26]. It was estimated from the rate constant for the formation of activated MAPK from MEK*-MAPK complex and the equilibrium constant for MEK*-MAPK complex formation. k_m^- is the lumped rate constant with which phosphatases deactivate MPK-1*. Likewise, its value was estimated from data available for MAPK*-Phosphatase complex formation [26]. No upregulation or downregulation of constitutive phosphatases was modeled, thus phosphatase levels are constant at (Ph_T). The maximum number of morphogen:morphogen-receptor complexes Ind^m and the total number of MPK-1 molecules mpk_T are estimated from the total number of EGFR molecules per cell and the total number of ERK molecules per cell, respectively [26].

k_n^+ is the constitutive rate of lateral signaling generation. This process it thought to be limited by synthesis of ligand LAG-2 or receptor LIN-12. We use a numerical estimate for k_n^+ based on the rate of EGF receptor synthesis [27]. k_n^- is the rate of constitutive deactivation of lateral signaling. Deactivation of lateral signaling occurs via two mechanisms: LAG-2:LIN-12 complexes dissociate or the cytoplasmic tail of LIN-12 is cleaved upon association with LAG-1 transcription factor. We assume that cytoplasmic LIN-12–LAG-1 complexes have a finite lifetime after which they are degraded by the proteosomal pathway. Therefore, the kinetic parameter k_n^- is set to a value between the rate of LAG-2–LIN-12 complex dissociation and the rate of proteosomal degradation of the cyto-LIN-12–LAG-1 complex. No experimental data are available about the lifetime of these complexes, thus base parameter estimates on the EGF-EGFR system are used [27].

k_{x_1} is the rate constant of MPK1* deactivation induced by lateral signaling. Thus it lumps both the lateral signal-mediated upregulation of MPK-1* phosphatases and the action of those phosphatases on MPK-1*. This rate constant is equivalent to that of constitutive phosphatases, except it incorporates the characteristic level of lateral signal-induced phosphatase expression. Therefore, we take $k_{x_1} = k_m^-(\mathrm{Ph_T})$. k_{x_2} is the rate constant of lateral signaling deactivation due to MPK-1*-mediated endocytosis of LIN-12 receptors. The appropriate value for the kinetic parameter k_{x_2} is then taken to be the rate constant for receptor/complex endocytosis adjusted for the fraction of active MPK-1*. k_{x_3} is the rate constant for MPK-1*-induced lateral signal generation. In cells with high inductive signaling, it defines the maximal rate at which lateral signaling is generated in a neighboring cell. k_{x_3} represents an induced process, thus we set its the value to almost one order of magnitude larger than the constitutive rates of gene expression.

$K_{M_{ind}}$ and $K_{M_{lat}}$ are parameters associated with induced transcriptional events. Their values are unknown, but reasonable choices could be $K_{M_{ind}} = 0.25(\mathrm{mpk_T})$ and $K_{M_{lat}} = 0.25[k_{x_3}/(k_{x_2}\mathrm{mpk_T})]$, i.e., 25% of the characteristic levels for inductive and lateral signaling, respectively.

2.8 Robustness of Improved Gradient Perception in Coupled Systems

We show here that for any parameter values, $Q^c > Q^\circ$ for a two cell system at steady state. At steady state the dimensionless inductive signal is (from Equation 2.4 in the text):

$$m_i = \frac{\mu I_i}{\mu I_i + 1 + \chi f(l_i)}; f(l_i) = \frac{l_i^2}{\kappa_l^2 + l_i^2}.$$

Using the definition for the gradient comparator, showing that $Q^c > Q^\circ$ is equivalent to showing that:

$$\frac{\ln(m_1^c / m_2^c)}{\ln(m_1^\circ / m_2^\circ)} > 1, \text{ or } \frac{m_1^c}{m_1^\circ} > \frac{m_2^c}{m_2^\circ}.$$

With the above formula for m_i, one needs to show that:

$$\frac{\mu I_1 + 1}{\mu I_1 + 1 + \chi f(l_1)} > \frac{\mu I_2 + 1}{\mu I_2 + 1 + \chi f(l_2)},$$
$$\frac{\mu I_2 + 1 + \chi f(l_2)}{\mu I_2 + 1} > \frac{\mu I_1 + 1 + \chi f(l_1)}{\mu I_1 + 1},$$
$$1 + \frac{\chi f(l_2)}{\mu I_2 + 1} > 1 + \frac{\chi f(l_1)}{\mu I_1 + 1}.$$

Since in the coupled case $\chi > 0$, one needs to show that:

$$\frac{f(l_2)}{f(l_1)} > \frac{\mu I_2 + 1}{\mu I_1 + 1}.$$

One can show that $f(l)$ is a one-to-one mapping, i.e., if $l_1 < l_2$ then $f(l_1) < f(l_2)$.

$$l_1 < l_2 \Leftrightarrow l_1^2 < l_2^2 \Leftrightarrow \frac{1}{l_2^2} < \frac{1}{l_1^2} \Leftrightarrow \frac{\kappa_l^2}{l_2^2} < \frac{\kappa_l^2}{l_1^2} \Leftrightarrow 1 + \frac{\kappa_l^2}{l_2^2} < 1 + \frac{\kappa_l^2}{l_1^2} \Leftrightarrow$$
$$\frac{\kappa_l^2 + l_2^2}{l_2^2} < \frac{\kappa_l^2 + l_1^2}{l_1^2} \Leftrightarrow \frac{l_1^2}{\kappa_l^2 + l_1^2} < \frac{l_2^2}{\kappa_l^2 + l_2^2} \Leftrightarrow f(l_1) < f(l_2)$$

If $I_1 > I_2$ then the induced lateral gradient is inverted with respect to the inductive gradient, i.e., $l_1 < l_2$ in either the presence or absence of lateral coupling. For example, in the absence of lateral coupling, if $I_1 > I_2$ then:

$$m_1 = \frac{\mu I_1}{\mu I_1 + 1}; m_2 = \frac{\mu I_2}{\mu I_2 + 1} \Rightarrow m_1 > m_2.$$

But, from Equation 2.9 in the text:

$$l_1 = \frac{\lambda_s + \psi^{-1} g(m_2)}{\lambda_d + \psi^{-1} m_1}; l_2 = \frac{\lambda_s + \psi^{-1} g(m_1)}{\lambda_d + \psi^{-1} m_2}; g(m_i) = \frac{m_i^2}{\kappa_m^2 + m_i^2}.$$

With $m_1 > m_2$ and $g(m)$ being a one-to-one mapping, then $l_1 < l_2$.

For $I_1 > I_2$ then:

$$\frac{\mu I_2 + 1}{\mu I_1 + 1} < 1.$$

Therefore, for $I_1 > I_2$ and any parameter choices (obviously $\mu \neq 0$ for inductive signaling to exist),

$$\frac{f(l_2)}{f(l_1)} > 1 > \frac{\mu I_2 + 1}{\mu I_1 + 1}.$$

2.9 Slight Asymmetry in VPC Array

P6.p is the precursor cell closest to the anchor cell, the source of LIN-3 inductive signal (Figure 2.1). The VPC array is not symmetric with respect to this cell. While P4.p receives lateral signals from two neighbors (P3.p and P5.p), the corresponding cell on the other side of the array (P8.p) has only one neighbor (P7.p). Thus, we expect that P8.p will display lower lateral activity than its counterpart P4.p. Figure 2.9 shows the position of P6.p, P7.p, and P8.p on the fate plane, analogous to that shown for P6.p, P5.p, P4.p and P3.p in Figure 2.7A. Comparing the two figures confirms that P8.p displays lower lateral activity than P4.p. Meanwhile, the lateral signal levels in P5.p and P7.p are similar, indicating that these activities are primarily determined by interaction with the P6.p cell. These observations indicate that the response of P3.p – P6.p is similar quantitatively to the response of the other half of the VPC array.

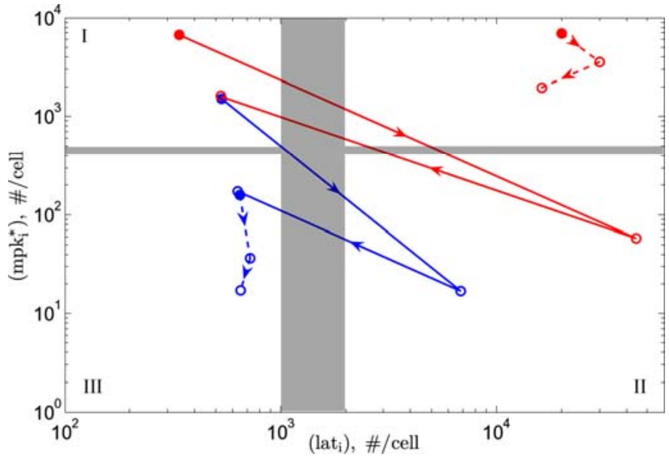

Figure 2.8. Position of P6.p–P8.p of wild-type and mutant alternating phenotypes on the fate plane

The position of P6.p, P7.p and P8.p on the fate plane in wild-type and mutant alternating phenotypes is shown for the same conditions as of Figure 2.6 in the manuscript. Here, the filled circle denotes P6.p and empty circles mark P7.p and P8.p in the direction of the arrows. Wild-type phenotype ($\mu = \mu^\circ$, blue) is shown for $I_{P6.p} = 10^{-3}$ (dashed) or $I_{P6.p}=10^{-2}$ (solid) at $\chi = 100$. Alternating mutant phenotype at $I_{P6.p} = 10^{-2}$ ($\mu = 10\ \mu^\circ$, red) is shown for $\chi = 0$ (dashed) or $\chi = 100$ (solid).

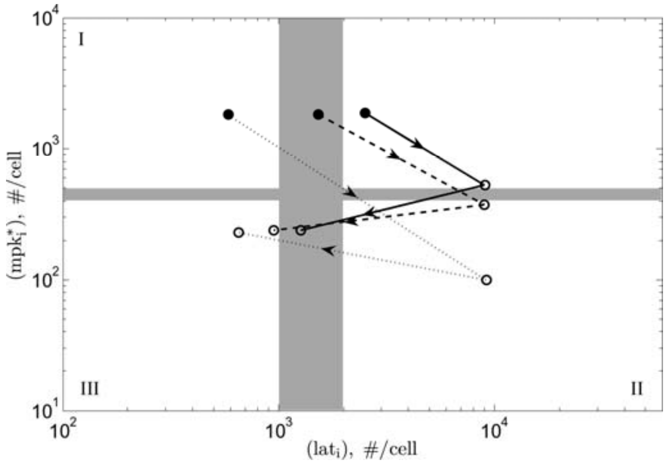

Figure 2.9. Position of P6.p–P8.p VPCs on the inductive and lateral signal map

The position of P6.p, P7.p and P8.p cells are depicted on the fate plane. This plot complements Figure 2.7A, which shows the response of P3.p – P6.p cells. Together, Figure 2.9 and Figure 2.7A reveal the response of the entire VPC array. Here, the filled circle denotes P6.p and empty circles mark P7.p and P8.p in the direction of the arrows. The lateral coupling strength was varied as $\chi_f = \chi/\chi^o = 0$ (solid), 1 (dashed) and 10 (dotted).

2.10 References

1. Sternberg, P.W. and H.R. Horvitz, *Pattern formation during vulval development in C. elegans.* Cell, 1986. **44**(5): p. 761-72.
2. Yoo, A.S., C. Bais, and I. Greenwald, *Crosstalk between the EGFR and LIN-12/Notch pathways in C. elegans vulval development.* Science, 2004. **303**(5658): p. 663-6.
3. Gurdon, J.B. and P.Y. Bourillot, *Morphogen gradient interpretation.* Nature, 2001. **413**(6858): p. 797-803.
4. Katz, W.S., et al., *Different levels of the C. elegans growth factor LIN-3 promote distinct vulval precursor fates.* Cell, 1995. **82**(2): p. 297-307.
5. Greenwald, I.S., P.W. Sternberg, and H.R. Horvitz, *The lin-12 locus specifies cell fates in Caenorhabditis elegans.* Cell, 1983. **34**(2): p. 435-44.
6. Sternberg, P.W., *Lateral inhibition during vulval induction in Caenorhabditis elegans.* Nature, 1988. **335**(6190): p. 551-4.
7. Sundaram, M.V., *Vulval development: the battle between Ras and Notch.* Curr Biol, 2004. **14**(8): p. R311-3.
8. Moghal, N. and P.W. Sternberg, *The epidermal growth factor system in Caenorhabditis elegans.* Exp Cell Res, 2003. **284**(1): p. 150-9.
9. Shaye, D.D. and I. Greenwald, *Endocytosis-mediated downregulation of LIN-12/Notch upon Ras activation in Caenorhabditis elegans.* Nature, 2002. **420**(6916): p. 686-90.
10. Chen, N. and I. Greenwald, *The lateral signal for LIN-12/Notch in C. elegans vulval development comprises redundant secreted and transmembrane DSL proteins.* Dev Cell, 2004. **6**(2): p. 183-92.
11. Shaye, D.D. and I. Greenwald, *LIN-12/Notch trafficking and regulation of DSL ligand activity during vulval induction in Caenorhabditis elegans.* Development, 2005.
12. Berset, T., et al., *Notch inhibition of RAS signaling through MAP kinase phosphatase LIP-1 during C. elegans vulval development.* Science, 2001. **291**: p. 1055-1058.
13. Fisher, J., et al., *Computational insights into Caenorhabditis elegans vulval development.* Proc Natl Acad Sci U S A, 2005. **102**(6): p. 1951-6.
14. Sternberg, P.W. and H.R. Horvitz, *The combined action of two intercellular signaling pathways specifies three cell fates during vulval induction in C. elegans.* Cell, 1989. **58**(4): p. 679-93.
15. Kimble, J., *Alterations In Cell Lineage Following Laser Ablation Of Cells In The Somatic Gonad Of Caenorhabditis-Elegans.* Developmental Biology, 1981. **87**(2): p. 286-300.
16. Wang, M. and P.W. Sternberg, *Competence and commitment of Caenorhabditis elegans vulval precursor cells.* Dev Biol, 1999. **212**(1): p. 12-24.
17. Krishnan, J. and P.A. Iglesias, *A modeling framework describing the enzyme regulation of membrane lipids underlying gradient perception in Dictyostelium cells.* J Theor Biol, 2004. **229**(1): p. 85-99.

18. Fanto, M. and M. Mlodzik, *Asymmetric Notch activation specifies photoreceptors R3 and R4 and planar polarity in the Drosophila eye.* Nature, 1999. **397**(6719): p. 523-6.
19. Levitan, D. and I. Greenwald, *LIN-12 protein expression and localization during vulval development in C. elegans.* Development, 1998. **125**(16): p. 3101-9.
20. Pribyl, M., C.B. Muratov, and S.Y. Shvartsman, *Discrete models of autocrine cell communication in epithelial layers.* Biophys J, 2003. **84**(6): p. 3624-35.
21. Shvartsman, S.Y., C.B. Muratov, and D.A. Lauffenburger, *Modeling and computational analysis of EGF receptor-mediated cell communication in Drosophila oogenesis.* Development, 2002. **129**(11): p. 2577-89.
22. Eldar, A., et al., *Self-enhanced ligand degradation underlies robustness of morphogen gradients.* Dev Cell, 2003. **5**(4): p. 635-46.
23. Horvitz, H.R. and P.W. Sternberg, *Multiple intercellular signalling systems control the development of the Caenorhabditis elegans vulva.* Nature, 1991. **351**(6327): p. 535-41.
24. Ferguson, E.L., P.W. Sternberg, and H.R. Horvitz, *A genetic pathway for the specification of the vulval cell lineages of Caenorhabditis elegans.* Nature, 1987. **326**(6110): p. 259-67.
25. Han, M. and P.W. Sternberg, *let-60, a gene that specifies cell fates during C. elegans vulval induction, encodes a ras protein.* Cell, 1990. **63**(5): p. 921-31.
26. Asthagiri, A.R. and D.A. Lauffenburger, *A computational study of feedback effects on signal dynamics in a mitogen-activated protein kinase (MAPK) pathway model.* Biotechnol Prog, 2001. **17**(2): p. 227-39.
27. Lauffenburger, D.A. and J.J. Linderman, *Receptors: Models for Binding, Trafficking, and Signaling*. 1993, New York: Oxford University Press.

CHAPTER 3: TOWARD MODEL VALIDATION: FLUORESCENCE IMAGING OF LIVE WORMS

3.1 Abstract

The *C. elegans* vulva is patterned from a set of six vulva precursor cells that respond to the graded concentration of EGF-like LIN-3 factor. Our mathematical model predicts that cell-cell coupling between adjacent precursor cells enhances perception of the LIN-3 gradient. Specifically, a gradient in extracellular LIN-3 across two adjacent precursor cells must be converted into a difference in the intracellular MAP kinase signal (MPK-1) in order for neighboring cells to choose distinct cell fates. Our model predicts that organisms with intact cell-cell coupling mechanisms will better achieve this extracellular-to-intracellular gradient conversion than mutant organisms in which cell-cell coupling has been perturbed. As an initial step toward experimental validation of our model predictions, we describe here several experimental procedures that we have explored for quantifying MPK-1 activity using a fluorescent reporter in live worms cultured both in standard and microfluidic platforms.

3.2 Introduction

The development of the nematode *C. elegans* entails one embryonic stage and four larval stages L1 through L4. Hatched embryos roam on agar plates with sinusoidal movements. Upon proceeding from one larval stage to the next, the animal becomes quiescent in its motion and sheds off the cuticle surrounding the body for about two hours, a period known as molt. For example, the L1 molt follows the first larval stage L1, before the animal enters the second larval stage L2. The time length of the larval stages (including molting period) is 16, 9, 9, and 11 hours for L1, L2, L3 and L4 stages, respectively (at 20 °C). Hence, after 45 hours from hatching the animal is a young adult [1]. Growth is slightly faster at 25 °C, with the animal becoming a young adult after 36 hours from hatching [2].

The vulva of the nematode *C. elegans* is derived from six Pn.p vulva precursor cells (VPCs) aligned along the antero-posterior axis of the body. These cells are born eight hours posthatching, in the L1 larval stage [1]. Upon receiving the LIN-3 (EGF-like protein) from the anchor cell in the gonad (see Figure 2.1 or 4.5 for graphical representation), the VPCs exit their elongated G1 phase [3] and specify and commit to undertake vulval fates. The anchor cell is specified from either one of the Z1.ppp or Z4.aaa cells during mid- to late-L2 stage [4, 5]. The Z1.ppp and Z4.aaa are born at the beginning of the L2 stage [1].

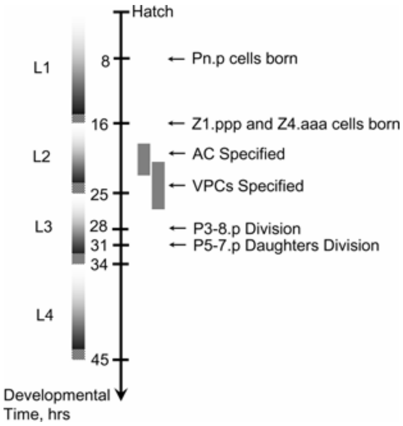

Figure 3.1. Events associated with specification of vulval precursor cells
The worm has four larval stages L1-L4. The vulval precursor cells (VPCs) that form worm vulva are specified in the period from mid-L2 to early-L3 by the LIN-3 signal released by the anchor cell (AC). The AC is randomly specified from one of the Z1.ppp or Z4.aaa cells. The time scale corresponds to animals grown at 20 °C.

Vulval precursor cells undertake the 1°, 2°, and 3° vulval fates through the interplay of LIN-3 inductive signaling and LIN-12 lateral signaling [6]. These two signaling networks are coupled by negative regulators [7]. One important finding from our modeling analysis of this regulatory network is that of the coupling between inductive and lateral signaling in the vulva precursor cells may amplify the extracellular LIN-3 gradient into steeper gradient in the intracellular MAP kinase signal (see Chapter 2 and [8]). In mathematical terms, gradient amplification is represented by this inequality:

$$Q^c = \frac{\ln\left(\text{mpk-1}^*_{\text{P6.p}} \big/ \text{mpk-1}^*_{\text{P5/7.p}} \right)\Big|_{\text{coupled}}}{\ln\left(\text{LIN-3}_{\text{P6.p}} \big/ \text{LIN-3}_{\text{P5/7.p}} \right)\Big|_{\text{coupled}}} > 1.$$

Importantly, gradient amplification is limited to certain parameter values, including certain LIN-3 gradients. Whether wild-type organisms operate with these parameter values is unknown. Meanwhile, we identified a second, closely related property of gradient perception that is robust to changes in all parameter values. This robust property is that the conversion of extracellular LIN-3 gradient into a gradient in the intracellular MAP kinase signal will always be better in an organism with intact signaling network that couples inductive and lateral signaling pathways. Ablating this coupling will hamper gradient perception. In mathematical terms, this finding is presented by this inequality:

$$\frac{\ln\left(\text{mpk-1}^*_{\text{P6.p}} \big/ \text{mpk-1}^*_{\text{P5/7.p}} \right)\Big|_{\text{coupled}}}{\ln\left(\text{mpk-1}^*_{\text{P6.p}} \big/ \text{mpk-1}^*_{\text{P5/7.p}} \right)\Big|_{\text{uncoupled}}} \frac{\ln\left(\text{LIN-3}_{\text{P6.p}} \big/ \text{LIN-3}_{\text{P5/7.p}} \right)\Big|_{\text{uncoupled}}}{\ln\left(\text{LIN-3}_{\text{P6.p}} \big/ \text{LIN-3}_{\text{P5/7.p}} \right)\Big|_{\text{coupled}}} > 1, \qquad (3.1)$$

where mpk-1^* refers to the intracellular signal triggered by the extracellular LIN-3.

3.3 Experimental Validation Strategy

To determine whether gradient amplification occurs in wild-type organisms, we would have to measure the gradient in extracellular LIN-3 and the gradient in intracellular MAP kinase signal. Visualization of morphogen gradients over tens to hundreds of cells has been achieved in several systems using antibody staining methods or fusion proteins of GFP and morphogen [9]. Unfortunately, similar approaches have been attempted but have not been successful in *C. elegans* [10]. Currently there is no method for direct measurement of the LIN-3 gradient. Moreover, our model predictions suggest that gradient amplification is not a robust property. Thus, whether the wild-type organism operates with parameter values that produce gradient amplification is unknown.

For these reasons, we turned to quantifying the second, closely related model prediction: gradient perception in coupled wild-type animals will always be better than in uncoupled mutants. Importantly, there is no experimental evidence to suggest that mutations that uncouple precursor cells would affect the secretion, transport and degradation of the LIN-3 signal. Therefore, the inequality Equation 3.1 simplifies to the following:

$$\frac{\left.\ln\left(\text{mpk-1}^{*}_{\text{P6.p}} \big/ \text{mpk-1}^{*}_{\text{P5/7.p}} \right)\right|_{\text{coupled}}}{\left.\ln\left(\text{mpk-1}^{*}_{\text{P6.p}} \big/ \text{mpk-1}^{*}_{\text{P5/7.p}} \right)\right|_{\text{uncoupled}}} > 1 .$$

Thus, there would be no need for direct measurement of LIN-3 gradient. Thus, to validate this model prediction, we would need: (a) to generate mutant animals in which lateral coupling is eliminated, and (b) to measure the level of intracellular MAP kinase signaling.

In order to generate worms with uncoupled pre-cursor cells, one can envision three methods. In the first method, one ablates the LIN-12 protein by introducing a *lin-12(0)* null mutation in wild-type worms using genetic manipulation. This method ensures that no lateral signal is ever turned on as the receptor for the signal is knocked out and that mutant worms are uncoupled. However, there are side effects to *lin-12(0)* mutants, one being a double anchor cell in the gonad [5]. While anchor cell ablation is commonly performed [4], the LIN-3 gradient of mutant, anchor cell ablated worms will be altered compared to the wild-type coupled worms and would not allow us to cancel the log ratio of LIN-3 in P6.p and P5/7.p in the equation above.

In the second method, one uses feeding RNAi [11]. If one assumes that intracellular biochemistry related to negative lateral feedback coupling does not influence gradient formation (for example by affecting receptor expression levels or endocytosis of receptor-ligand complexes), then wild-type worms (coupled) and worms exposed to RNAi against negative regulators of inductive signaling have the same quasi-steady specification extracellular LIN-3 gradients and the log ratio involving LIN-3 in P6.p and P5/7.p cancels out in the equation above. While we originally invalidated this method due to need of multiple RNAis and the efficiency of RNAi method, it was recently shown [12] that lateral signaling does influence the receptor distribution in P5/7.p. Hence, in a model where the LIN-3 gradient is shaped through release from the anchor cell and endocytosis of LIN-3::LET-23 receptors, this gradient would not be similar in wild-type coupled worms and worms exposed to RNAi (uncoupled).

In the third method one measures MPK-1 activity at early and late stages of specification and then compares the dynamics. At early stages of specification, the negative regulators of MPK-1 activity are not expressed yet, as lateral signaling ligands and MPK-1^* target genes are being expressed first. At such early stages, the gradient in MPK-1^* activity is equivalent to that of an uncoupled system. At later stages of specification, negative regulators such as *ark-1*, *lip-1*, and *lst* genes have been expressed and the measured reporter activity is that of the coupled system.

The activity of MPK-1 in the vulva precursor cells cannot yet be measured directly and requires the use of a fluorescent reporter. Activation of MPK-1 leads to phosphorylation of two transcription factors, LIN-1 and LIN-31 [13] . The gene *egl-17* encodes the *C. elegans* fibroblast growth factor and this gene is specifically expressed in the VPCs at the time of their induction and later on in their descendants in response to MPK-1 activity [14]. It has been recently shown that the Ets transcription factor LIN-1 is required for expression of the *egl-17* gene during vulva induction [15]. The following experimental work uses the very sensitive reporter *arIs92* that is driven by the *egl-17* promoter and has been shown to detect the gradient in MPK-1 activity [7]. However, quantitative correlation between reporter activity and the amount of active MPK-1 (or even phosphorylated LIN-1) depends on the half-life of the reporter protein. CFP half-life in yeast has been estimated at 72 min [16]. While half-life in the P3-8.p cells of *C.*

elegans may be slightly different, this short half-life should allow for inferring activity upstream of reporter from reporter intensity data.

Here we describe four experimental methods that were used to obtain the dynamic expression profile of the *arIs92* reporter activity during early-L2 to early-L3 stages of vulva development of *C. elegans* larvae and the advantages and disadvantages that emerged.

3.4 Results and Discussion

3.4.1 Quantitation of CFP Fluorescence Images

Visualization of individual cells in *C. elegans* requires 100× DIC and fluorescence microscopy. Figure 3.2 displays a typical set of images acquired for quantitation.

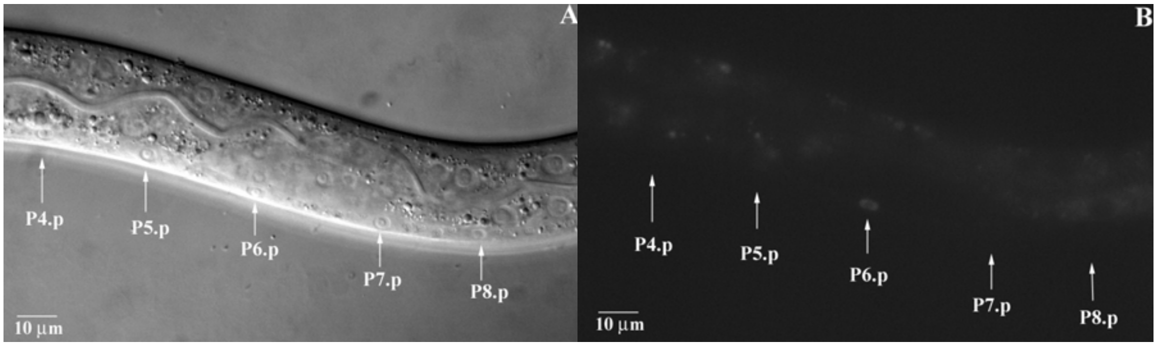

Figure 3.2. Worm imaging at 100× magnification
(A) DIC image of a late-L2 worm (as judged by the size of gonad primordium). The nuclei of VPCs P4-8.p are indicated with arrows. (B) CFP fluorescence image of the same worm in (A). Only P6.p cell shows visible reporter fluorescence at this stage.

Production of CFP fluorescence images suitable for quantitation requires that pixels in the region of interest are not saturated. Testing several settings of gain and offset on the acquisition camera indicated that for the CFP fluorophore in *arIs92* transgene pixel saturation does not occur when the offset is zero and gain is as high as 200 digital levels (maximum is 255) if the integration time is kept within 2 seconds (data not shown). To ensure linearity of fluorescence signal with the integration time, images were collected at multiple integration times, ranging from 100 ms to 2 seconds (Figure 3.3). Prolonged exposure of the fluorophore to incident excitation light is twofold deleterious: it photobleaches the fluorophore and it heats up the worm sample. Hence, image collection at different integration times requires to manually open and close the incident light shutter on the microscope between exposures.

Measuring CFP reporter fluorescence intensity requires quantitation of acquired digital images. We developed Matlab code that processes a set of digital images as follows. First, the DIC image is loaded and the user can mark the P5-7.p cells. Then each fluorescent image (corresponding to exposure at a different integration time) is loaded already having the position of the P5-7.p marked as previously selected from the DIC image. In order to easily select regions of interest corresponding to nuclear fluorescence from P5-7.p the image is automatically “autoleveled” such that all 255 gray levels are used in the displayed image. Two to four regions of interest are selected corresponding to background fluorescence (usually measured by considering an area of similar pixel size as nuclei of P5-7.p, positioned somewhere between the P6.p and P5/7.p nuclei) and to fluorescence in the P6.p and P5/7.p nuclei. Pixel intensity in the regions of interest is reported from the original nonautoleveled image. Analysis of the region of interest includes area and maximum, minimum and mean pixel intensities. Quantitative data from maximum and mean pixel intensities agree (data not shown).

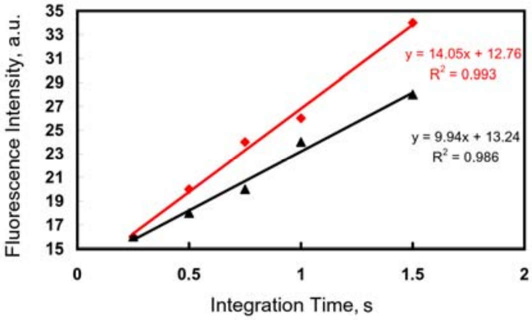

Figure 3.3. Measurement of fluorescence intensity in vulval precursor cells
Analysis of CFP fluorescence in P6.p cell shown in Figure 3.2 (red) vs. background fluorescence (black). Pictures at different integration times are taken to avoid pixel saturation. *y*-axis measures maximum pixel intensity over P6.p nucleus based on a manually selected region of interest.

The fluorescence level (a.u.) in a cell is reported as the slope of the fluorescence intensity in that cell minus the slope of the background fluorescence intensity (Figure 3.3).

3.4.2 Dynamic egl-17::cfp-lacZ Expression from Individual Anesthetized Worms Imaged at Several Developmental Times

Comparing reporter activity for the same developmental time in different worms requires that these worms are synchronized along their developmental time axes (i.e., have the same developmental age) such that each worm is positioned appropriately along the time axis. We have used two synchronization methods: “lay-off and hatch-off” and L1 starvation (see experimental details). However, we find that there is slight variability in the developmental age of the worms produced by these procedures (data not shown). Either worms desynchronize from the time of synchronization (L1 stage or hatching) to the time of imaging (L2 stage) or there is enough worm-to-worm variability in the "synchronized" population to begin with. Hence, developmental age needed to be inferred on a worm-to-worm basis based on characteristics such as the size of the gonad primordium.

Worms are naturally moving sinusoidally on agar foraging for bacteria. High magnification imaging requires that worms are immobile, hence worms are anesthetized prior to mounting on slide. However, the anesthetic can be deleterious to the worms and can slow their growth or reduce their viability to experimental manipulation.

Figure 3.4 displays the *arIs92* fluorescence dynamics in five worms following anesthesia at the indicated starting developmental times (early-, mid-, or late-L2). After imaging at a particular relative developmental time, worms were washed with M9 buffer to recover them from anesthesia. This procedure cannot be repeated very often, hence only three or four relative developmental times can be imaged before the worm is not viable anymore.

If we compare the early-L2 vs. mid-L2 vs. late-L2 worms, we notice that initially fluorescence is very weak and present only in P6.p cell, then it seems to increase in both P6p and P5.p or P7.p cells, and then it disappears in P5.p and P7.p while continuing to increase in P6.p. While this is in agreement with previous qualitative results [7], there seems to be great variability in the fluorescence levels in these cells. This variability could be due to intrinsic worm-to-worm variations and our imprecise knowledge of exact developmental time of the worm. Individual worms must ultimately correct for this variability such that correctly patterned vulvas are formed each time.

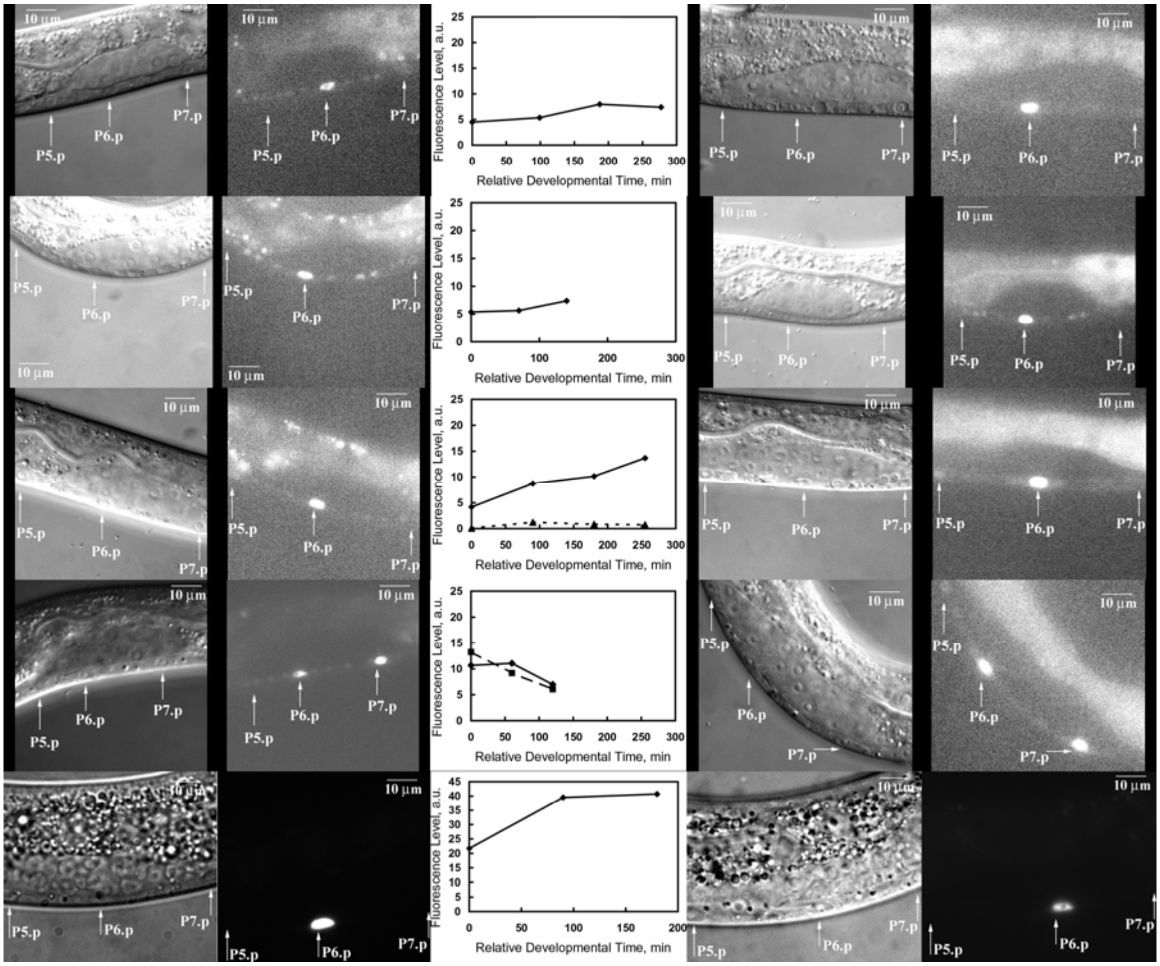

Figure 3.4. Dynamics of MPK-1 reporter activity in VPCs at L2 larval stage from single anesthetized worms
(Middle column) Quantification of fluorescence levels in P6.p (continuous line and diamonds) and P5.p (dotted line and triangles) or P7.p (dashed line and squares) cells in worms anesthetized at multiple times during their development. (First and second columns) Nomarski and *arIs92* fluorescence images of worms at the zero relative developmental time reported in the middle column. (Fourth and fifth columns) Nomarski and *arIs92* fluorescence images of worms at the last relative developmental time reported in the middle column. Worms were at early-L2 stage (first and second rows), mid-L2 stage (third and fourth rows), and late-L2 stage (fifth row), respectively for the zero relative developmental time reported in the middle column. Actual developmental times (early-, mid-, or late-L2) were determined based on the size of the gonad primordium. Levels in the fluorescence images of the second and fifth columns should not be compared to one another as brightness and contrast have been adjusted differently for clarity.

Notice that *arIs92* fluorescence intensity in the VPCs during early to mid-L2 stage (when the gradient is observed in VPCs) is very weak and is expected to have very low signal-to-noise ratio. Figure 3.4 shows that visualization of weak fluorescence in P5.p or P7.p cells requires significant changes of image contrast such that autofluorescence of the worm body becomes visible. Such changes are not necessary for imaging at late-L2 (bottom row of Figure 3.4) or early-L3 (data not shown) stages as fluorescence is then visible to the eye without any contrast adjustments. Although subjective to digital camera settings in different laboratories via digital gain and offset, this qualitative observation is consistent with published reports using the *arIs92* fluorescence reporter to visualize MPK-1* activity gradient at L2 stage [17, 18]. In our analysis, quantitation is performed on raw pixel intensities and should not alter the fluorescence levels reported here for different worms if camera settings were the same. However, these levels are very low. In fact, for fluorescence imaging during L2 stage, signal-to-noise (reported as the slope of fluorescence intensity in the cell of interest vs. the slope of fluorescence intensity of the background—see Figure 3.3) in P7.p cell can be as low as 1.2:1 and as high as 2:1. In P6.p, the signal-to-noise can be as low as 1.5:1 and as high as 3:1. During late L2 and L3 stages, *arIs92* fluorescence intensity improves such that signal-to-noise ratio can be as high as 4:1.

3.4.3 Dynamics of egl-17::cfp-lacZ Expression from Multiple Anesthetized Worms Imaged at a Single Developmental Time

Worm length is a quantity with high dynamic range during larval development. For example the worm extends from about 350 μm in L2 to about 600 μm in L3 [2]. Here, we used worm length as a marker of developmental time of individual worms. We measured fluorescence from multiple randomly picked worms in a synchronized culture by imaging anesthetized worms at a single developmental time. We then measured the length of these worms using 10× magnification and aligned them on the “worm length” axis (Figure 3.5). Ordering of the worms along this axis agrees with qualitative judgment of developmental age based on size of the gonad primordium.

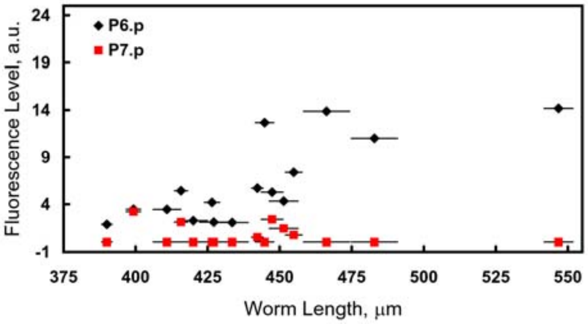

Figure 3.5. Dynamics of MPK-1 reporter activity in VPCs at L2 larval stage from multiple anesthetized worms
Worm length is indicative of the developmental age of the worm imaged. The fluorescence level in P6.p and P7.p was measured in sixteen worms at different developmental ages. Errorbars indicate standard deviation of three measurements of worm length at 10× magnification.

These results show that at inferred (from worm length) early L2 stages fluorescence in P6.p cells is low and it is absent from P5/7.p cells. Fluorescence in P7.p cell is only present at intermediate lengths and correlates with low P6.p fluorescence (except for the worm at about 400 μm, which shows equal fluorescence levels in P6.p and P7.p, a phenomenon ascribed to variability in the position of the anchor cell and the gonad). High P6.p fluorescence occurs for even longer and older worms.

3.4.4 Dynamic egl-17::cfp-lacZ expression from individual immobile worms imaged at several developmental times

The previous two subsections illustrate that there actually is a lot of variability among worms and that obtaining the complete dynamic profile of *egl-17::cfp-lacZ* transgene expression in the vulval precursor cells requires imaging of single worms over elongated periods of time. We have shown that wild-type worms cannot survive exposure to anesthetic over such elongated periods and that repeated mounting and unmounting from slides between exposures also reduces worm viability.

There is evidence that wild-type worms mounted on slides and maintained on slide can survive and develop normally ([1] and data not shown). Therefore we decided to generate an immobile worm strain that would contain a mutation which does not interfere with the process of vulva specification and formation.

The *unc-54(e190)* is a null allele of the *unc-54* gene. The *unc-54* gene encodes a muscle myosin class II heavy chain, is expressed in different muscle cell types in the worm body, and it is required for locomotion and egg laying. Mutant L1 larvae are able to move, but they become slower as they grow older. Mutant adults are immobile and cannot lay eggs due to defects in the uterine and vulval muscles, hence eggs hatch inside the mother.

We have developed a mutant strain of worms that carries the transgene *arIs92* and the *unc-54(e190)* mutation (see materials and methods for details). Low motility of L2 larvae makes this strain immobile when mounted on agar slides for imaging.

Figure 3.6 and Figure 3.7 display the fluorescence dynamics over a five-hour period of time in worms starting in early-L2 or mid-L2 larval stage (the stage has been inferred from the size of the gonad primordium and whether the posterior distal tip of the primordium was posteriorly positioned with respect to P7.p VPC). Interestingly, the worm at early-L2 stage (Figure 3.6) displays *arIs92* fluorescence in the P5-7.p cells before the time of anchor cell specification. A common feature of reporter fluorescence dynamics in these worms (middle panels in Figure 3.6 and Figure 3.7) is that fluorescence levels do not show a clear increasing or decreasing trend over the five-hour time window of imaging. While fluctuations could be accounted for by slight changes in focus during imaging (confocal microscopy should address this issue), the lack of a trend poses a conundrum.

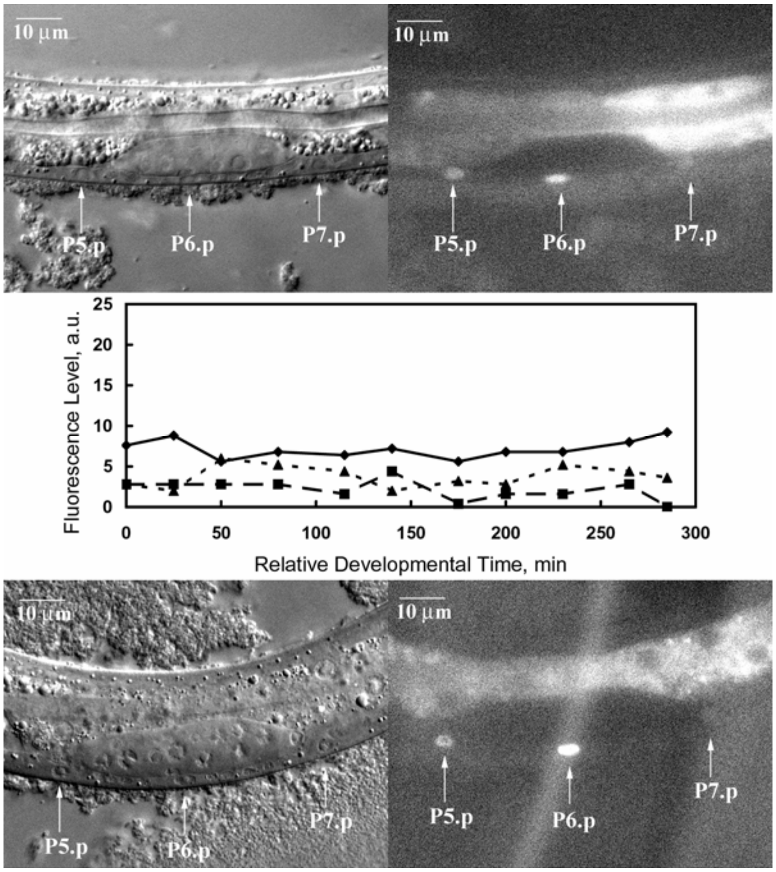

Figure 3.6. *ArIs92* reporter activity dynamics at early-L2 larval stage in *unc-54* worms
(Top row) Nomarski and *arIs92* fluorescence imaging of an early-L2 worm at zero minutes relative developmental time. (Middle row) Dynamics of quantified fluorescence levels in P6.p (continuous line and diamonds), P5.p (dotted line and triangles), or P7.p (dashed line and squares) over a five-hour time period. (Bottom row) Nomarski and *arIs92* fluorescence imaging at the end of the imaging period corresponding to about 290 minutes of relative developmental time.

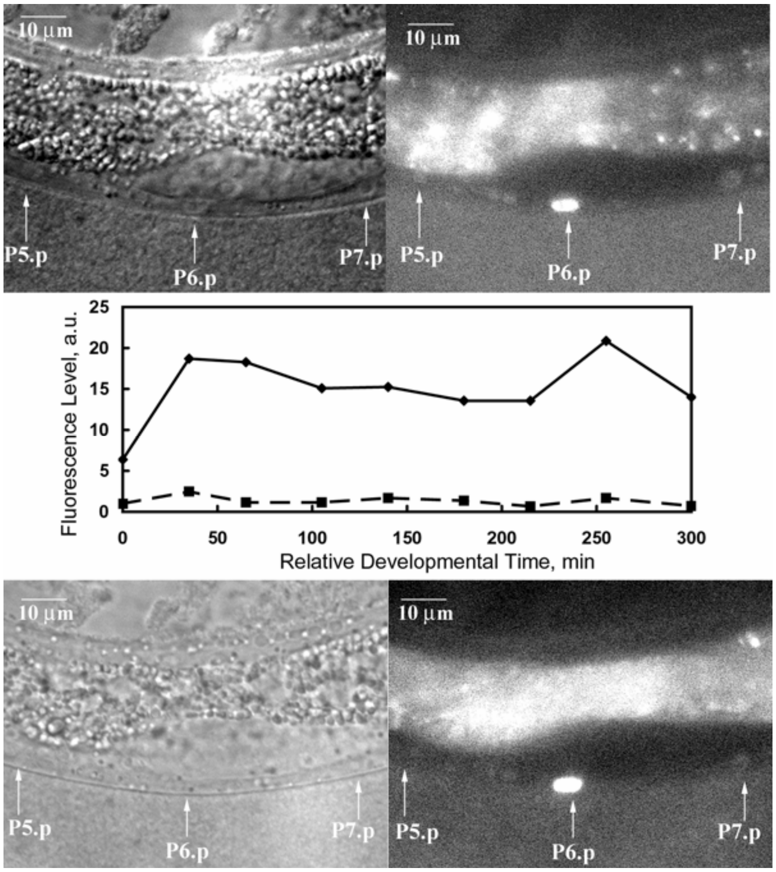

Figure 3.7. *ArIs92* fluorescence dynamics at mid-L2 larval stage in *unc-54* worms (Top row) Nomarski and *arIs92* fluorescence imaging of a mid-L2 worm at zero minutes relative developmental time. (Middle row) Dynamics of quantified fluorescence levels in P6p (continuous line and diamonds) and P7.p (dashed line and squares) cells over a five-hour time period. (Bottom row) Nomarski and *arIs92* fluorescence imaging at the end of the imaging period corresponding to 300 minutes of relative developmental time.

To solve this conundrum, we tested whether worms imaged on-slide for prolonged time develop a vulva at all. For yet another early-L2 worm we observed the same fluctuating stationary fluorescence dynamics over a period of five hours (Figure 3.8, second row). After imaging, the worm was viable and was recovered and returned to an agar plate. The next day, after about 1700 minutes from start of the imaging session, this worm showed a vulva corresponding to mid to late-L3 stage (Figure 3.8, fourth row). This huge delay in vulva development suggests that on-slide imaged worms arrest development and that development resumes upon return to normal culturing conditions, albeit not immediately.

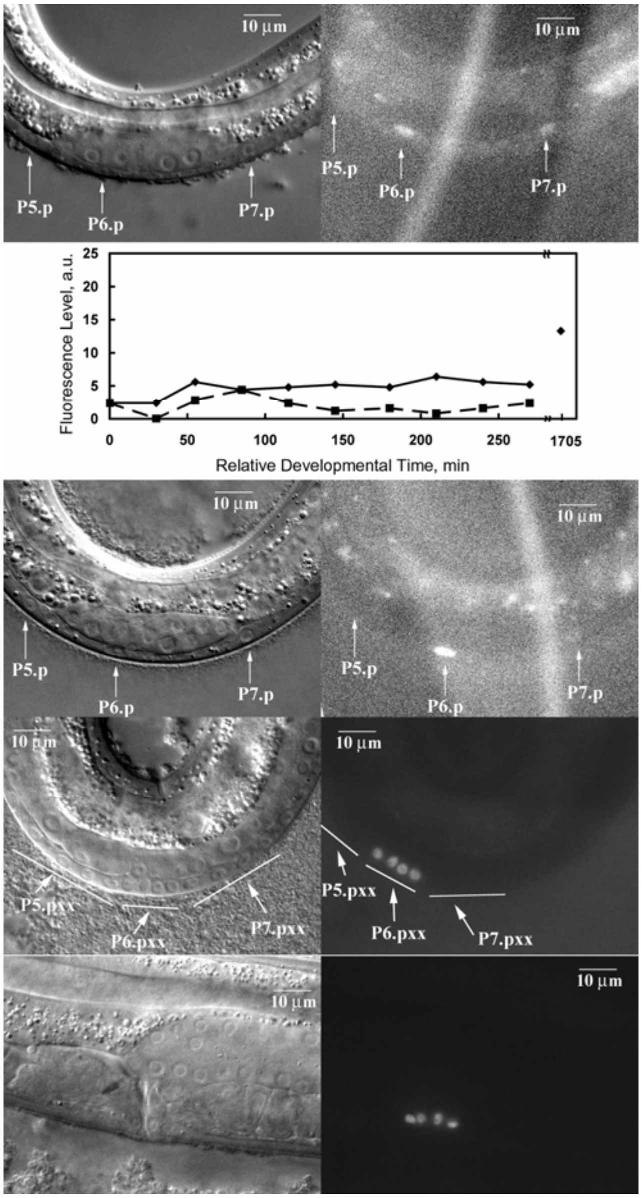

Figure 3.8. Worms maintained on microscope slide take longer to develop
(First row) Nomarski and *arIs92* fluorescence imaging of a mid-L2 worm at zero minutes relative developmental time. (Second row) Dynamics of quantified fluorescence levels in P6.p (continuous line and diamonds) or P7.p (dashed line and squares) cells over a five-hour time period. Isolated diamond quantifies fluorescence at 1700 minutes of relative developmental time, averaged over the four P6.pxx granddaughters presented in the fourth row. (Third row) Nomarski and *arIs92* fluorescence imaging at the end of the imaging period corresponding to about 300 minutes of relative developmental time. (Fourth row) Nomarski and *arIs92* fluorescence imaging one day after the imaging session, corresponding to about 1700 minutes of relative developmental time. (Fifth row) Nomarski and *arIs92* fluorescence imaging two days after the imaging session. Levels in the fluorescence images of the second column should not be compared to one another as brightness and contrast have been adjusted differently for clarity.

In order to ascertain this delay on a shorter developmental time scale, we continuously imaged on-slide an early-L3 worm (developmental stage inferred from size and structure of gonad) for four hours and asked whether we observe the first division of the induced VPC cells. Figure 3.9 (middle row) recapitulates the results in Figure 3.6 to Figure 3.8 with respect to fluorescence dynamics, namely fluorescence level in VPCs fluctuates during the imaging period rather than showing a clear increasing or decreasing trend.

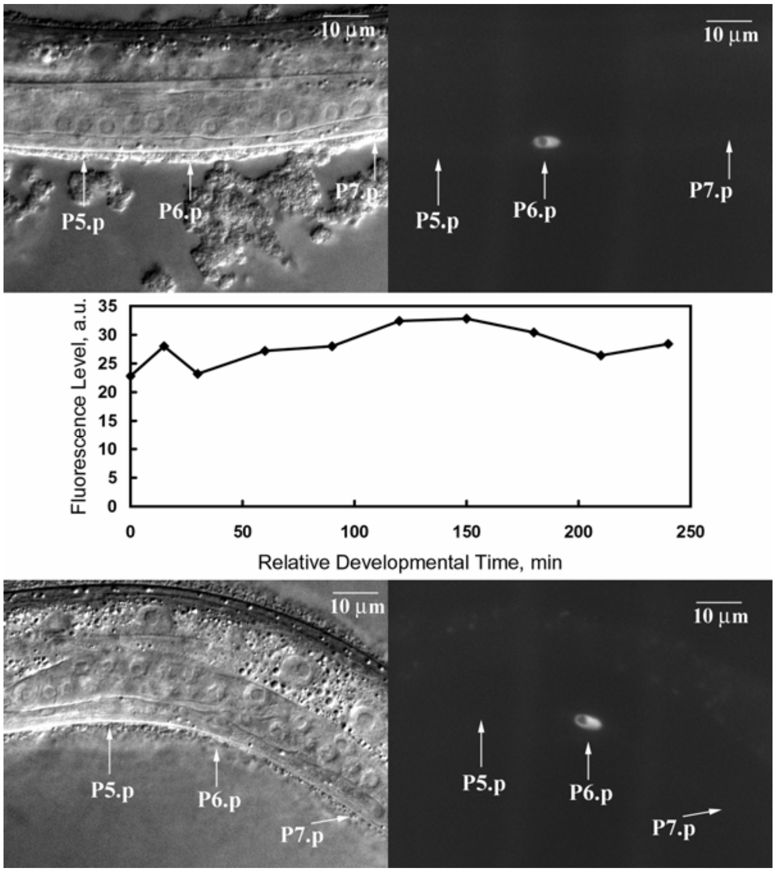

Figure 3.9. *ArIs92* reporter activity dynamics at early-L3 larval stage in *unc-54* worms
(Top row) Nomarski and *arIs92* fluorescence image of an early-L3 worm, corresponding to zero minutes relative developmental time in the middle row. (Middle row) Dynamics of quantified P6.p fluorescence levels over a four hour time period. (Bottom row) Nomarski and *arIs92* fluorescence imaging at the end of the imaging period corresponding to 240 minutes of relative developmental time.

The observed delay is not due to the worm being dead. Similar to the worm in Figure 3.8, this worm was recovered and imaging the following day showed that vulva forms normally (data not shown).

In order to further confirm this delay in development, we asked whether worms briefly imaged at early-L3 stage, but maintained on agar plates display the same phenomenon. Figure 3.10 displays three such worms, briefly imaged at early-L3 stage (based on size and structure of gonad) and then returned to the agar plate for a period of 300 to 400 minutes, and then briefly imaged again. Such worms should display VPC daughters after 210 minutes and VPC granddaughters after 360 minutes (see Figure 3.1). Figure 3.10 shows that these worms do develop normally and reach the two- and four-cell stage of P5-7.p division at the appropriate time. Furthermore, notice the variability in the fluorescence levels in these worms at early-L3 stage (relative developmental time zero in each worm). As explained before, lack of precise knowledge of developmental time in each worm and intrinsic worm-to-worm variability contributes to this variability. Fluorescence levels in P6.p progeny should not be compared as dilution due to cellular division acts on top of the original worm-to-worm variability.

These results thus show that maintaining the *unc-54* strain of worms on slide for continuous imaging delays their development. Possible reasons include reduced oxygen availability or lack of nutrition due to limited foraging for bacteria.

Imaging using immobile worms add to the results of the previous section by further showing that fluorescence quantitation at L2 stage has a very small signal-to-noise ratio (Figure 3.6 to Figure 3.8), with this ratio improving for fluorescence images of worms in L3 stage (Figure 3.9 and Figure 3.10).

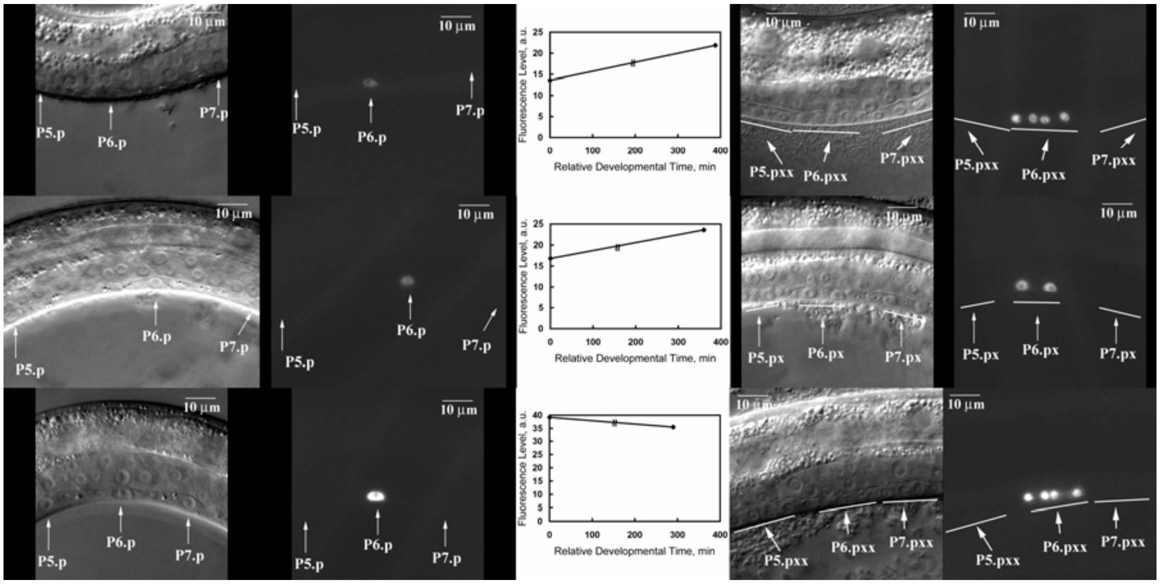

Figure 3.10. Development on agar plates occurs faster than on microscope slides (Top, middle and bottom rows) Three early-L3 stage worms briefly mounted on microscope slide for imaging at two developmental time points about 300 to 400 minutes apart. (Two left columns) Nomarski and fluorescence images of the three worms at the early developmental time point. (Two right columns) Nomarski and fluorescence images of the three worms at the late developmental time point. (Middle column) Quantification of fluorescence (in P6.p or averaged over its descendants) at the indicated times corresponding to the left or right columns. Fluorescence levels in the images of the second and fifth columns should not be compared to one another as brightness and contrast have been adjusted differently for clarity.

3.4.5 Imaging Worms Trapped in a Microfluidic Device

The previous subsections illustrated that continuous monitoring of signaling molecules guiding worm development requires experimental imaging conditions where worms do not lack oxygen and nutrition. Taking advantage of the possibility of maintaining *C. elegans* in liquid culture [19] a microfluidic device was designed in Professor's Changhuei Yang's lab to allow worm trapping and pinning for imaging.

Figure 3.11 shows a top-view diagram of the microfluidic device and its mode of operation. The design uses control layer (red) valves to allow flow in the flow layer (black) (Figure 3.11A) [20]. The worm is trapped at the gratings (Figure 3.11B) where it can be pinned down for imaging. Worms are loaded by closing the valves associated with bacterial feed and worm outlet (Figure 3.11C). Once a worm has been trapped, the worm inlet valve is closed and bacterial flow is allowed through the feed lines (Figure 3.11D). Bacterial flow is driven by a three-valve peristaltic pump or external pressure.

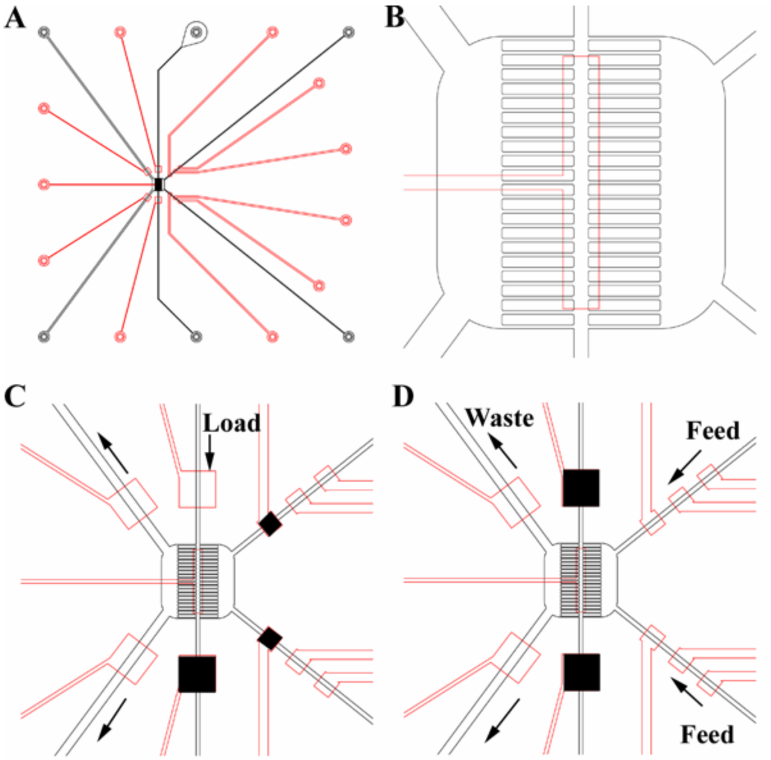

Figure 3.11. Microfluidic device for worm trapping and imaging
(A) Overall schematic of the microfluidic device with a control layer (red) and a flow layer (black). (B) Worm chamber: the worm is trapped in the line between the gratings and can be pinned down by pressurizing the top control layer valve (vertical red rectangular contour). (C) Worm loading: the feed and worm outlet valves are closed (black squares) while worm inlet and feed outlet valves are open. (D) Worm maintenance: worm inlet and outlet valves are closed (black squares) and bacteria is flowed through the feed lines and exits through the waste lines.

We were able to load, maintain, and image worms in the microfluidic device. Figure 3.12 shows low magnification imaging of a trapped worm. Successful worm trapping depends on worm age. L1 larvae can pass through the gratings and cannot be easily trapped. Larger worms (L2-L4 stages) are initially partially squeezed through the grating (Figure 3.12) but are able to release themselves later on. Since the height of the flow channel needs to be properly controlled for the control layer valves to seal correctly, the microfluidic device does not allow flow of young adult or older worms.

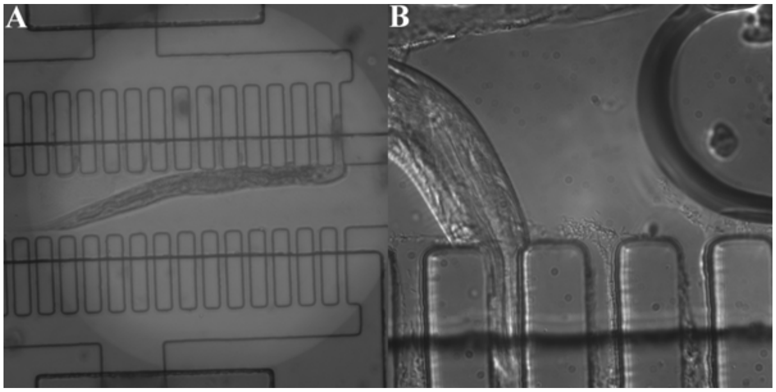

Figure 3.12. Worm trapping in the microfluidic device
(A) 10× magnification imaging of worm trapping. (B) 20× magnification imaging of another trapped worm.

An added advantage of the microfluidic device is the ability to pin down worms to immobilize them for high magnification imaging in the absence of anesthetic and without the need to generate immobile mutant strains. Figure 3.13 shows a high magnification Nomarski image and the corresponding fluorescence image from the *arIs92* reporter of an L4 worm. Fluorescence quantitation can be performed on acquired images (data not shown).

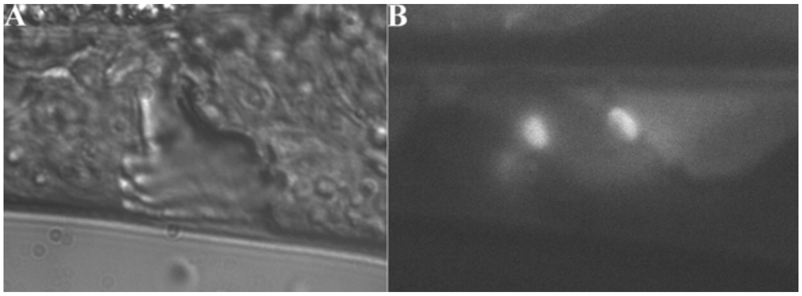

Figure 3.13. High magnification 100× imaging in the microfluidic device
Nomarski (A) and fluorescence (B) images of vulva of an L4 stage worm trapped and pinned down in the microfluidic device.

Obtaining dynamic fluorescence reporter activity over many hours of development requires that the worm is pinned during imaging and then released afterwards for several times during an experiment. Hence we asked whether worm viability is altered after a pinning session. Figure 3.14 shows the same worm imaged in Figure 3.13, but now released from pinning. The image sequence shows that the worm is alive and moving in the flow channel.

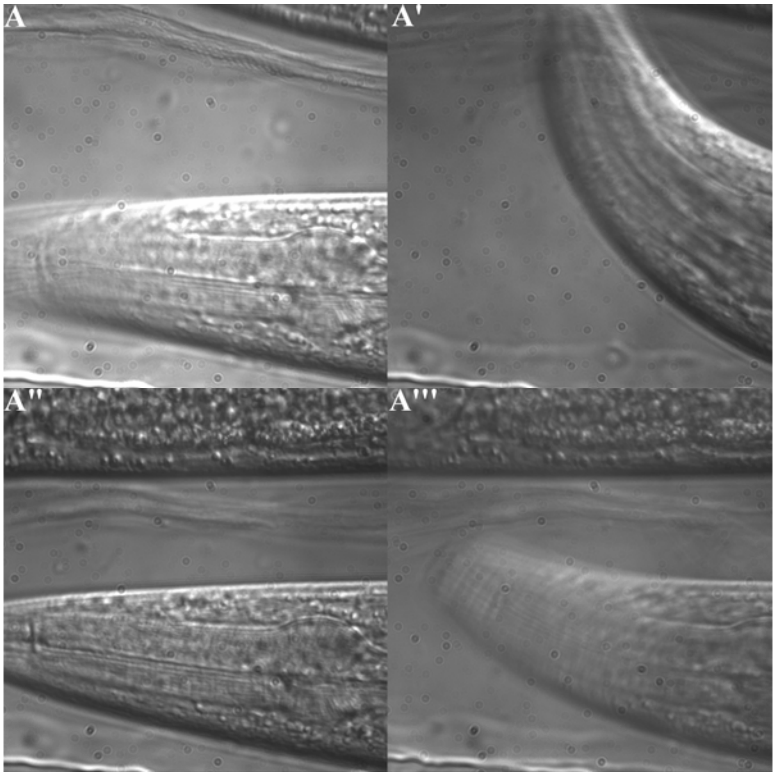

Figure 3.14. Worms survive in the microfluidic device

Additional work is required to probe elongated worm viability in the microfluidic chamber. There currently does not exist a method of recovering trapped worms from the microfluidic chamber. Future designs could potentially alleviate this problem.

3.5 Materials and Methods

3.5.1 Strain Maintenance

This study used the strain *unc-54(e190)* and the transgenic lines *unc-4(e120); arIs92[egl-17p::cfplacZ, unc-4(+), ttx-3::gfp], him-8(e1489); arIs92[egl-17p::cfplacz, unc-4(+), ttx-3::gfp]*, and *unc-54(e190); arIs92[egl-17p::cfplacZ, unc-4(+), ttx-3::gfp]*. Worms were grown in 60 mm Petri dishes, on an OP50 *E. coli* bacterial lawn on agar. Plates of all strains were stored in an incubator at 20 °C. Worms were passed every two-three generations as the bacterial lawn depleted on the plate by picking several L1 larvae or unhatched eggs and transferring them to a new plate.

3.5.2 Microscopy

On-slide imaging was performed on agar (5% w/v in water; BD, Difco Noble Agar, Cat. No. 214230) pads prepared using usual protocol [19]. Briefly, a patch of agar is made on a glass microslide (Gold Seal, Cat. No. 3011), and a worm is sandwiched between the agar pad and a glass coverslip (Fisherbrand Coverglass, Cat. No. 12-542A).

Worm loading on the pad for anesthetized worms was performed as follows: 3 μL of M9 (3 g/L KH_2PO_4, 6 g/L Na_2HPO_4, 5 g/L NaCl, 1 mM $MgSO_4$) buffer plus 0.1 mM levamisole (Sigma, L9756) anesthetic or S-basal (5.85 g/L NaCl, 1 g/L K_2HPO_4, 6 g/L KH_2PO_4, 1 mL cholesterol (5 mg/mL in ethanol)) buffer plus 0.1 mM levamisole were placed on the agar pad, and then a single worm was transferred from the plate into this droplet using a worm pick with a speck of bacteria on the tip.

For immobile, *unc-54(e190)*, mutant worms loading was performed as follows: one first prepares a pad of agar on glass microslide and places 2.5 μL of M9 or S-basal on the pad. Then a speck of bacteria was placed in the center of a glass coverslip and 0.5 μL of M9 buffer or S-basal buffer were dropped on the speck. A worm was picked from a plate with the worm pick and deposited in the bacterial speck. The coverslip was placed on top of the agar pad such that the two droplets fall onto one another. In this way the worm is assured to be located in the middle of a bacterial lawn during imaging.

S-basal buffer is used whenever the worm is kept on slide for a prolonged period of time as the animals require cholesterol for molting and other functions. To prevent drying of the agar pad on the slide during prolonged imaging, a droplet of S-basal buffer was added around the pad at about 30-minute intervals.

Differential interference contrast (DIC) and cyan fluorescent protein (CFP) images of worms were acquired using a Zeiss Axioskop microscope equipped with a Hamamatsu Orca-ER C4742-80 digital camera (12 bit, 1×1 bining, 1× digital gain, low light mode) using 10× (Achroplan/0.25 Ph) or 100× (Plan-Neufluar/1.3 oil) objectives. Further camera settings: for Figure 3.2 to Figure 3.4 the digital gain was 10 and offset was zero; for Figure 3.5 the digital gain was 200 and offset was zero; for Figure 3.6 to Figure 3.10 the digital gain was 26 and offset was zero. Other camera settings (integration time) were used as detailed in the section 3.4.1. Imaging of worms in the microfluidic device was performed with a similarly equipped Zeiss Axiovert 200 inverted microscope. Images were captured using Openlab 5.0.2. Using a hemacytometer pixel sizes were determined to be: 10× – 8pixels/10μm, 100× – 71 pixels/10μm. Microscopy was performed in a room at temperature 21-23 °C.

3.5.3 Manufacturing of the Microfluidic Device

The polydimethylsiloxane (PDMS) microfluidic device was manufactured using the standardized protocol of the microfabrication facility at Caltech. Briefly, the bulk of the the chip is made of a 5:1 w:w mix of GE RTV615A and GE RTV615B silicone components. The thin membrane that separates the control and flow layers is made of a 20:1 w:w mix of RTV615A and RTV615B. The thick and thin layers are baked in oven at 80 °C for 90 and 45 minutes, respectively, following by alignment of the two layers. The layers are cut and then bonded by baking in the oven at 80 °C for two hours. The chip is then attached to a glass coverslip (Thomas Red Label, Cat. No. 6663-G67) spincoated with PDMS and further baked for two hours.

3.5.4 Generating the Mutant Immobile Worm Strain

The transgenic strain *unc-54(e190); arIs92[egl-17p::cfplacZ, unc-4(+), ttx-3::gfp]* was generated during this study to allow imaging of CFP fluorescence dynamics in single worms without reverting to anesthetic. This line was obtained by crossing the myosin deficient strain *unc-54(e190)* with the transgenic strain *him-8(e1489); arIs92[egl-17p::cfplacz, unc-4(+), ttx-3::gfp]*. The former strain is defective of egg laying, hence eggs hatch inside the mother and the mother dies while freeing up the young animals. The latter produces a population with an increased occurrence of males due to the *him-8* mutation. Briefly, 3 males of the latter strain were allowed to roam together with 6 or 7 hermaphrodites of the former strain on an agar plate. One progeny (such progeny must be heterozygous for the *him-8* mutation, the *unc-54* mutation, and the *arIs92* transgene) displaying GFP fluorescence (from *ttx-3::gfp* marker) was picked from the plate, transferred to an empty plate and allowed to self. Twelve of its progeny displaying GFP fluorescence were further selected and plated individually on twelve plates. Only those plates containing a dead mother due to larvae hatching inside and displaying fluorescent larvae were kept. These plates contained mothers that were homozygous for the *unc-54* mutation and the progeny must be at least heterozygous for the *arIs92* transgene. Such progeny was passed repeatedly by selecting marker expressing worms until a plate that showed only fluorescent hermaphrodites was identified.

3.5.5 Strain Synchronization

Two methods of synchronizing the developmental stage of worms were used. Synchronization was necessary to produce populations of worms at known developmental stages for studies in the microfluidic device or on-slide imaging using anesthetic. The first method takes advantage of the growth arrest of L1 larvae in the absence of food. Upon return to a bacterial lawn such L1 larvae resume development. A plate with many gravid mothers is bleached using a bleach solution (20% v/v bleach in water, 0.5M KOH). The unhatched eggs survive the procedure and are resuspended in M9 buffer. They will hatch in this solution but arrest growth due to lack of food [2]. Freshly prepared (one- to two-days-old) L1 starved worms reach mid-L2 stage after 24 hours from plating on the bacteria lawn in agar plates. The second method is the lay-off and hatch-off procedure [21]. Briefly, twenty to thirty gravid adults are transferred to a plate and allowed to lay eggs for two hours. Twenty to thirty eggs are further picked and moved to a separate plate. Twelve hours later unhatched eggs are picked from this plate and allowed to hatch on a different plate for one hour. Those eggs that hatched (usually three or four) during this period will reach L2 molt in 24 hours. Neither of these synchronization procedures can be applied to *unc-54* mutant strain as in this case eggs hatch inside the mother and larvae die upon bleaching.

3.6 Acknowledgements

Many thanks to Oren Schaedel for intriguing discussions about the microfluidic design. Help from Adeline Seah, Jennifer Green, and Mihoko Kato in the Sternberg lab is also greatly appreciated. I would like to thank Xiquan Cui in Professor's Changhuei Yang's laboratory for manufacturing the microfluidic devices.

3.7 References

1. Sulston, J.E. and H.R. Horvitz, *Post-embryonic cell lineages of the nematode, Caenorhabditis elegans.* Dev Biol, 1977. **56**(1): p. 110-56.
2. Wood, W.B., *The Nematode Caenorhabditis elegans* 1988, Cold Spring Harbor: Cold Spring Harbor Laboratory Press.
3. Euling, S. and V. Ambros, *Heterochronic genes control cell cycle progress and developmental competence of C. elegans vulva precursor cells.* Cell, 1996. **84**(5): p. 667-76.
4. Kimble, J., *Alterations in cell lineage following laser ablation of cells in the somatic gonad of Caenorhabditis elegans.* Dev Biol, 1981. **87**(2): p. 286-300.
5. Greenwald, I.S., P.W. Sternberg, and H.R. Horvitz, *The lin-12 locus specifies cell fates in Caenorhabditis elegans.* Cell, 1983. **34**(2): p. 435-44.
6. Sternberg, P.W. and H.R. Horvitz, *The combined action of two intercellular signaling pathways specifies three cell fates during vulval induction in C. elegans.* Cell, 1989. **58**(4): p. 679-93.
7. Yoo, A.S., C. Bais, and I. Greenwald, *Crosstalk between the EGFR and LIN-12/Notch pathways in C. elegans vulval development.* Science, 2004. **303**(5658): p. 663-6.
8. Giurumescu, C.A., P.W. Sternberg, and A.R. Asthagiri, *Intercellular coupling amplifies fate segregation during Caenorhabditis elegans vulval development.* Proc Natl Acad Sci U S A, 2006. **103**(5): p. 1331-6.
9. Teleman, A.A. and S.M. Cohen, *Dpp gradient formation in the Drosophila wing imaginal disc.* Cell, 2000. **103**(6): p. 971-80.
10. Sternberg, P.W., *Personal communication*. 2005.
11. Tabara, H., A. Grishok, and C. C. Mello, *RNAi in C. elegans: Soaking in the Genome Sequence.* Science, 1998. **282**(5388): p. 430-431.
12. Stetak, A., et al., *Cell fate-specific regulation of EGF receptor trafficking during Caenorhabditis elegans vulval development.* Embo J, 2006. **25**(11): p. 2347-57.

13. Tan, P.B., M.R. Lackner, and S.K. Kim, *MAP kinase signaling specificity mediated by the LIN-1 Ets/LIN-31 WH transcription factor complex during C. elegans vulval induction.* Cell, 1998. **93**(4): p. 569-80.
14. Burdine, R.D., C.S. Branda, and M.J. Stern, *EGL-17(FGF) expression coordinates the attraction of the migrating sex myoblasts with vulval induction in C. elegans.* Development, 1998. **125**(6): p. 1083-93.
15. Tiensuu, T., et al., *lin-1 has both positive and negative functions in specifying multiple cell fates induced by Ras/MAP kinase signaling in C. elegans.* Dev Biol, 2005. **286**(1): p. 338-51.
16. Hackett, E.A., et al., *A family of destabilized cyan fluorescent proteins as transcriptional reporters in S. cerevisiae.* Yeast, 2006. **23**(5): p. 333-49.
17. Dutt, A., et al., *EGF signal propagation during C. elegans vulval development mediated by ROM-1 rhomboid.* PLoS Biol, 2004. **2**(11): p. e334.
18. Fisher, J., et al., *Predictive modeling of signaling crosstalk during C. elegans vulval development.* PLoS Comput Biol, 2007. **3**(5): p. e92.
19. Stiernagle, T., *Maintenance of C. elegans*, in *WormBook*, T.C.e.R. Community, Editor. 2006, WormBook.
20. Unger, M.A., et al., *Monolithic microfabricated valves and pumps by multilayer soft lithography.* Science, 2000. **288**(5463): p. 113-6.
21. McCarter, J., et al., *Soma-germ cell interactions in Caenorhabditis elegans: multiple events of hermaphrodite germline development require the somatic sheath and spermathecal lineages.* Dev Biol, 1997. **181**(2): p. 121-43.

CHAPTER 4: PREDICTING PHENOTYPIC DIVERSITY AND THE UNDERLYING QUANTITATIVE MOLECULAR TRANSITIONS

4.1 Abstract

During development, regulatory signaling networks instruct cell populations to form multicellular patterns and structures. These signaling networks are composed of highly interconnected molecular interactions. Quantitative variations in these molecular interactions are likely to produce phenotypic changes, the full range of which is impossible to gauge through laboratory genetics. Meanwhile, evolution may exploit "quantitative diversification" as a means to explore phenotypic alternatives while maintaining a constant signaling network architecture. Here, we describe a computational approach to quantify and to explore the phenotypic capacity of a developmental signaling network and apply it to vulval development in *C. elegans*. The phenotypes predicted to arise from quantitative variations in the signaling network span eleven species in the *Caenorhabditis* genus, and model analysis reveals the critical quantitative changes that must have evolved during the diversification of a common ancestor.

4.2 Introduction

Developmental signaling networks instruct cell populations to form multicellular structures and patterns. Select mutations that perturb these regulatory networks yield particular phenotypic alterations [1, 2]. However, the mutant phenotypes uncovered by experimental genetics do not capture the full capabilities of a system. Experimental

---

Manuscript prepared for submission by C. A. Giurumescu, P. W. Sternberg, and A. R. Asthagiri.

studies are typically constrained to extreme modes of perturbation (e.g., knockout or overexpression) and rarely probe potential phenotypic changes due to quantitative alterations to signaling pathways. The regulatory networks that drive developmental patterning are extraordinarily complex [3], and quantitative perturbations are likely to shift their performance into different regimes, and possibly, render alternative phenotypes.

Uncovering the capacity to produce alternative phenotypes due to quantitative variations in network performance is especially significant from the standpoint of evolution [4]. Closely related species may have evolved by subtle, quantitative changes in network interactions rather than large-scale changes to network topology. Thus, the phenotypic capacity gauges the potential for “local” evolutionary diversity.

While the phenotypic capacity of developmental signaling networks is difficult to gauge experimentally, a computational framework that is able to predict phenotypes based on molecular mechanisms provides a unique and essential platform to explore the phenotypic capacity of a particular developmental signaling network. Therefore, using a computational model of *C. elegans* vulval development [5] (detailed in Chapter 2 and Section 4.6), we sought to quantify how many different phenotypes are possible if the underlying network were perturbed quantitatively.

The *C. elegans* vulva develops from an array of six pre-cursor cells (Figure 4.5). These cells commit to a spatial pattern of distinct fates with each fate contributing to different aspects of the fully developed vulva. The patterning process is guided by a highly coupled regulatory network involving a spatial gradient in an inductive signal and direct cell-cell interactions between neighboring cells. Our mathematical model encodes this regulatory network and predicts the pattern of cell fates. Distinct from other modeling strategies [6, 7], this mathematical model formally encodes the quantitative strength of every molecular interaction in the regulatory network, a necessary feature to probe quantitative diversification.

4.3 Phenotypic Capacity

To determine the phenotypic capacity of the vulval signaling network, we varied all model parameter values over a broad physiological range (Table 4.1 and Section 4.7). For each set of model parameter values, the multicellular phenotype was computed. With each phenotype occupying different regions of parameter space, a phase diagram of phenotypes has been developed for this multicellular system.

Table 4.1. Dimensionless model parameters
The model has eight dimensionless parameters associated with the various molecular interactions known to contribute to the specification of vulval pre-cursor cells (see Section 4.6).

Parameter	Meaning
I	Level of inductive signal at the center of the symmetric gradient
ΔI	Gradient steepness
χ	Strength of lateral inhibition of inductive signaling
λ	Basal level of lateral signal
ϕ	Upregulation of lateral signaling to neighboring cells by inductive signaling
θ	Downregulation of receptors for receiving lateral signals by inductive signaling
κ_m	Threshold of inductive signaling needed to upregulate lateral signaling
κ_l	Threshold of lateral signaling needed to inhibit inductive signaling

Our calculations show that the phenotypic diversity of this system, i.e., the total number of distinct phenotypes across the entire parameter space, has an upper limit. As the parameter space is broadened, the number of distinct phenotypes saturates at approximately 560 multicellular patterns (Figure 4.1A). This result reveals that the developmental network is not constrained to a few outcomes that are most actively studied by experimental genetics. Thus, the wild-type and a handful of well-studied mutant phenotypes by no means represents the phenotypic diversity of this system. Furthermore, in this six-cell system there are four fates possible to each cell (Section 4.6.2). Hence, the theoretical upper limit to the number of phenotypes is 4,096. Our model predicts that the molecular network constrains the system from accessing ~85% of the theoretically possible phenotypes.

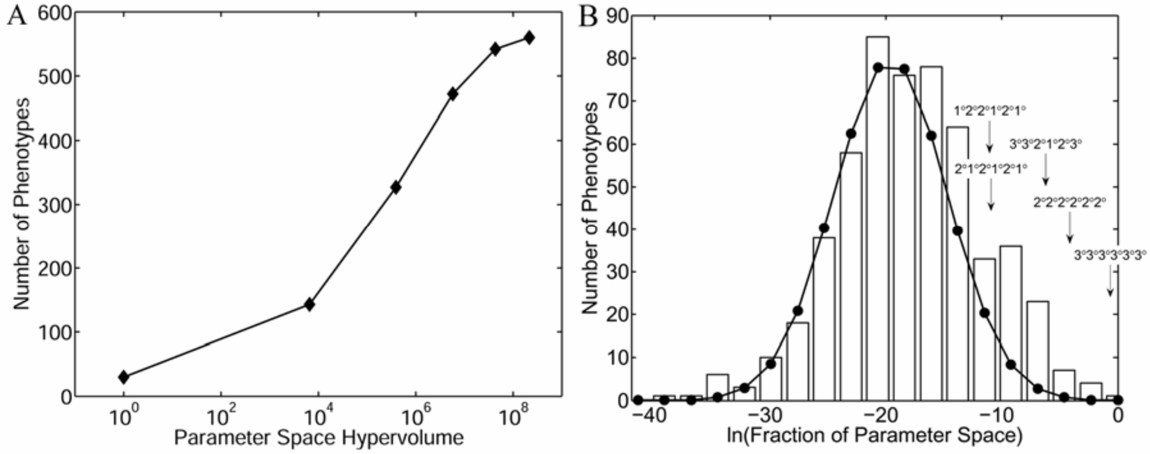

Figure 4.1. Coupled network restricts phenotypic diversity
(A) The total number of predicted phenotypes saturates upon expanding the volume of the parameter space around a central reference point. (B) A histogram depicting the number of phenotypes (bars) occupying different fractions of the parameter space. This histogram is compared to a log-normal distribution (filled circles). The occupancy of the parameter space follows a log-normal distribution with a positive skew. The model predicts that experimentally observed phenotypes (indicated with an arrow) have high frequency of occurrence and fall into the positive skew.

To better understand how the phenotypes are represented in parameter space, we determined the amount of parameter space that gives rise to each phenotype (Section 3.7). Phenotypes that occupy a small region in parameter space may be inaccessible experimentally, while their counterparts occupying a large fraction of parameter space may represent the more tangible outcomes. The distribution of phenotypes in parameter space resembles a log-normal distribution (μ=-19.60, σ=4.90) with a slight positive skew, suggesting that a small subset of phenotypes occupies a disproportionately large portion of the parameter space (Figure 4.1B). Interestingly, within this positive skew are the wild-type phenotype and several well-studied mutants [8, 9]. In addition to these well-established phenotypes, our model predicts ~35 novel phenotypes that are two standard deviations above the mean (Table 4.5). On the other end of the distribution, there are 19 phenotypes that are two standard deviations below the mean (Table 4.6). None of these phenotypes are among the well-studied experimentally observed phenotypes. These may be highly unlikely outcomes that would further reduce our evaluation of the phenotypic capacity of this system.

4.4 Rendering Mutant Phenotypes

Having identified phenotypes with the greatest representation within the parameter space, a key question is how does one render such phenotypes experimentally? The phase diagram of phenotypes allows us to address this question by performing the computational equivalent of a random genetic screen [1, 2]. We identify the mutant phenotype of interest within the phase diagram and then quantify the single-parameter changes (i.e., single mutations) that lead to this outcome starting from the wild-type phenotype (Figure 4.2A; Section 3.8). These computations yield a probability that an increase (or decrease) in an individual parameter will shift the phenotype from wild-type to a mutant pattern. Parameter changes with a higher transition probability have a greater likelihood of generating the desired mutant phenotype.

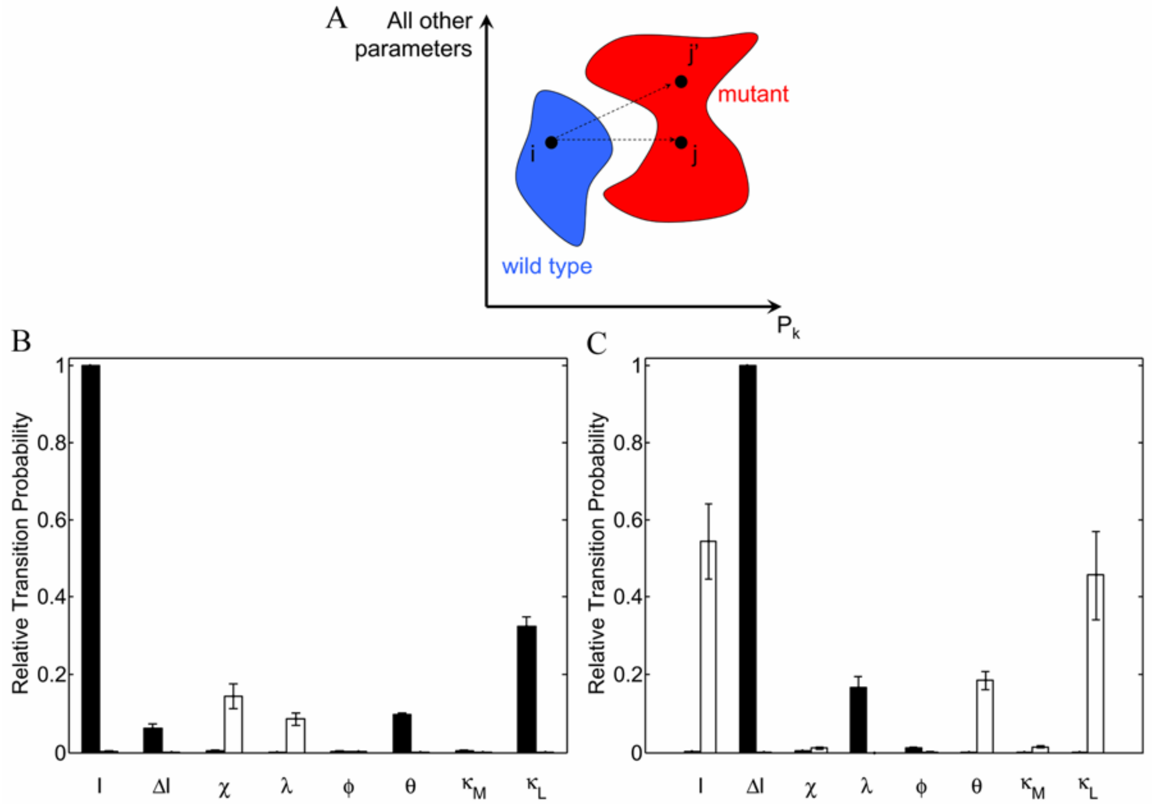

Figure 4.2. Model identifies optimal molecular perturbations necessary to generate experimentally observed mutant phenotypes
(A) Schematic for counting phenotype transitions made possible by single mutations. Subspaces in the 8-dimensional parameter space are occupied by different phenotypes. This diagram portrays a simplified version of the phenotype phase diagram with a single parameter P_k isolated on the *x*-axis and all other parameters denoted on the *y*-axis. The transition from i→j can occur by a change in a single parameter P_k, but the transition i → j' cannot. By counting the number of successful single mutations (i → j) for each parameter P_k, we quantify the relative efficacy of each parameter to render a specific phenotype transition (W → M) (Section 4.8). (B), (C) Relative probability of inducing a transition from the wild-type phenotype to the 3°3°3°3°3°3° phenotype (B) or to the hyperinduced 2°1°2°1°2°1° phenotype (C) by decreasing (filled columns) or increasing (open columns) the values of parameters indicated on the *x*-axis. The *y*-axes report the mean relative transition probability averaged over a broad combination of threshold values for fate-determining signals, and the error bars denote the standard deviation (Section 4.8). The size of the error bar reveals that model predictions are robust to variations in the threshold values of fate-determining signals.

We first applied this approach to predict the best single-parameter changes needed to transform the wild-type organism into a vulvaless mutant. Vulvaless phenotypes have been observed in genetics experiments and occur when all vulval precursor cells acquire the 3° fate. Our model predictions reveal that the best way to render the 3°3°3°3°3°3° phenotype is by decreasing the level of inductive signaling (Figure 4.2B). This result is consistent with experiments in which anchor cell ablation yields the uninduced all-3° fate pattern [10].

In the other extreme of phenotypes, mutant worms with multiple vulvae have been observed when the inductive signaling pathway is hyperactivated. In these mutants, the vulval precursor cells acquire an intriguing alternating pattern of 2°1°2°1°2°1° where each 1° cell produces an invagination [11]. Consistent with experiments, the model scores an increase in inductive signal as one of the most prominent ways to yield this alternating phenotype (Figure 4.2C). In addition, it predicts equivalent perturbations that would render the same outcome. Among these equivalent classes of mutations is an increase in the threshold of lateral signaling needed to inhibit the MAP kinase pathway (κ_L). Such a mutation would be performed by decreasing the binding affinity of the lateral signaling transcription complex (LAG-1:LIN-12-cyto) to LBS elements in the *cis*-regulatory regions of the genes that negatively regulate inductive signaling [12] (*lip-1*, *lst-1,2,3,4*). This mutation would require greater lateral signaling to inhibit the inductive MAP kinase pathway and would be an indirect way to inflate the inductive signaling activity, conceptually consistent with direct hyperactivation of the inductive signaling pathway.

Another prediction of the model is that flattening the gradient in soluble inductive factor would yield the 2°1°2°1°2°1° phenotype. This particular prediction is remarkably consistent with what has been recently uncovered about the most classical experimental mutation to yield this phenotype. The loss of *lin-15* has been shown to cause the secretion of LIN-3 from the surrounding cells, an event that would ablate the gradient [13].

An intriguing feature of mutants, such as *lin-15(lf)* [9, 11] and *let-60(gf)* [14], is that the observed multicellular pattern is variable. In addition to 2º1º2º1º2º1º, the other prominent outcome is 1º2º2º1º2º1º. There are several possible sources of variability [15]. The quantitative levels and interactions of signaling molecules may differ among wild-type organisms in which the mutation is performed; thus, their response to a specific perturbation may produce different outcomes. Alternatively, even if two organisms were "quantitative clones," the magnitude of a perturbation being introduced by the mutation may vary; for example, the amount of RNAi delivered may be different. Finally, even if the perturbation and the wild-type organisms were exactly the same, the execution of the molecular network may deviate due to stochastic effects.

Regardless of the source of variability, the key question we focused on is why this variability would produce these two particular outcomes and not others. We hypothesized that in parameter space, variable mutant phenotypes may lie in the same general direction from the wild-type phenotype. That is, because the starting point, the extent of perturbation and the execution of a perturbation may differ, the target points in parameter space on which these perturbations land will vary but lie within a common vicinity.

To test this hypothesis, we determined what other phenotypes would be predicted by the model upon increasing the inductive signal (Figure 4.3A) or flattening the gradient (Section 4.9). Indeed, the 1°2°2°1°2°1° phenotype is predicted to occur in response to both perturbations, revealing that the variable mutant phenotypes lie in the same direction in parameter space from the wild-type phenotype. However, an apparent conundrum is that the number of predicted phenotypes is far greater than that observed experimentally in *C. elegans*. In fact, similar calculations show that phenotypes other than 3°3°3°3°3°3° are possible when the level of inductive signal is decreased (Figure 4.3A).

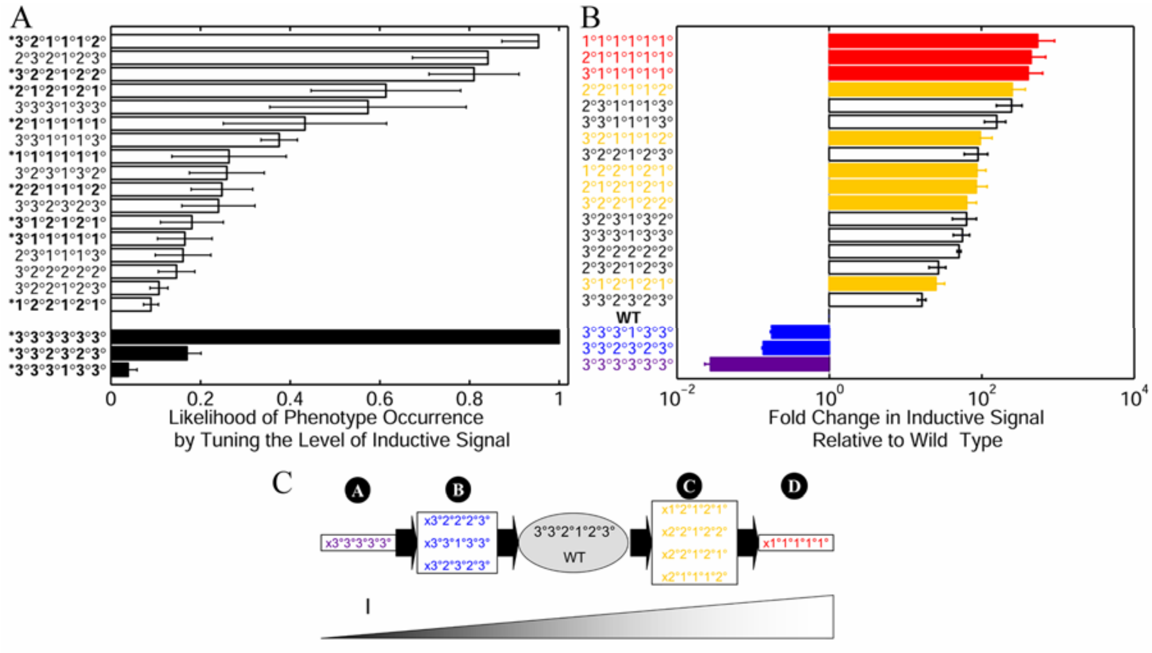

Figure 4.3. Hierarchical phenotypic diversity caused by quantitative changes in morphogen level
(A) The relative probability (*x*-axis) of reaching different mutant phenotypes (*y*-axis) upon decreasing (filled bars) or increasing (open bars) the amount of LIN-3 morphogen (Section 4.9). Phenotypes denoted with an asterisk are experimentally observed phenotypes as detailed in Figure 4.3C. (B) The predicted fold change in inductive signal necessary to convert the wild-type phenotype into underinduced phenotypes (Fold Change in Inductive Signal < 1) and overinduced phenotypes (Fold Change in Inductive Signal > 1) (Section 4.9). The phenotypes listed on the *y*-axis are the same as in Figure 4.3A and are re-sorted according to the required fold change in inductive signal. The colors correspond to the experimentally observed phenotypes highlighted in Figure 4.3C. (C) Summary of experimentally observed phenotypes. Distinct phenotypes have been reported upon increasing or decreasing the level of inductive signal (*I*) in as many as eleven members of the *Caenorhabditis* genus [16]. The phenotypes are grouped here into Classes A, B, C and D according to the amount of perturbation in inductive signal that rendered each mutant. Colors indicate a large increase (red), moderate increase (orange), moderate decrease (blue) and large decrease (violet) in *I*. The fate of the first VPC (P3.p) was not reported [16] and is indicated as "x".

4.5 Evolutionary Aspects

Why then is the remarkably rich set of predicted phenotypes vastly under sampled in *C. elegans*? One intriguing hypothesis is that our model predicts not only phenotypes that arise in *C. elegans*, but also those occurring in several closely related species that use the same molecular network topology to pattern vulval precursor cells. Several such species have been identified, and recent experiments revealed that tuning the level of inductive signal produces distinct species-specific mutants even though the starting wild-type phenotype is the same [16]. Indeed, the experimentally observed phenotypes spanning eleven species in the *Caenorhabditis* genus (Figure 4.3C) match the ones predicted by our model (Figure 4.3A).

Furthermore, the quantitative change in inductive signal needed to render each phenotype is also predicted (Figure 4.3B) and is fully consistent with experimental results (Figure 4.3C). In experiments, the 3°3°3°3°3° (Class A) and 1°1°1°1°1° (Class D) phenotypes are observed only when inductive signal is strongly decreased or increased, respectively; meanwhile Class B (3°2°3°2°3°, 3°2°2°2°3° and 3°3°1°3°3°) and Class C (1°2°1°2°1°, 2°2°1°2°1°, 2°2°1°2°2° and 2°1°1°1°2°) phenotypes occur upon moderate decrease and increase in inductive signal, respectively. Our model predicts this quantitative hierarchy of phenotype classes as inductive signal is increased or decreased from the wild-type starting point (Figure 4.3B).

These results suggest that the parameter space associated with the wild-type phenotype actually contains several subspaces, each representing different species (Figure 4.4A). The key question is which subspace of parameter values corresponds to each species. The answer to this question would reveal how the quantitative settings of this developmental network have evolved during the emergence of the *Caenorhabditis* genus.

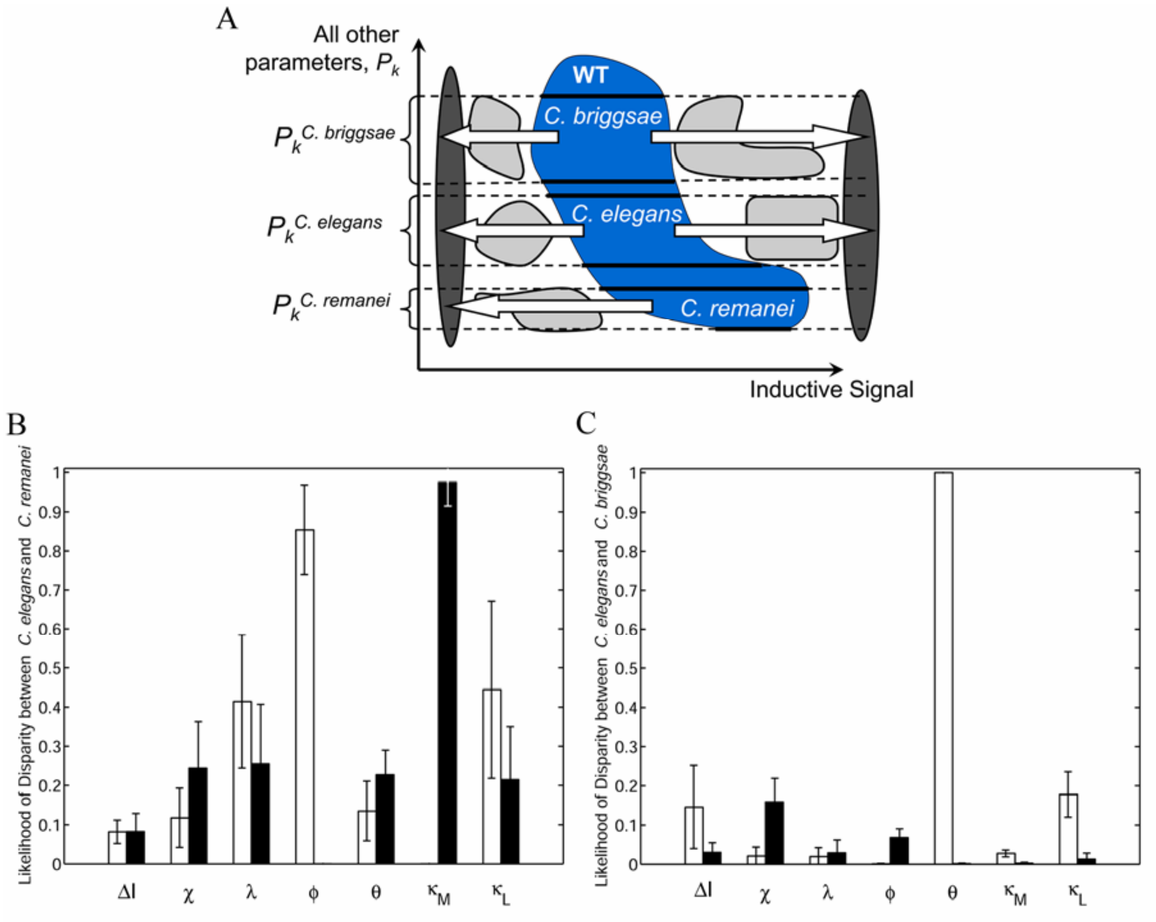

Figure 4.4. Quantitative differences predicted to have arisen during the evolution of the *Caenorhabditis* genus

(A) Schematic for identifying each species within the wild-type parameter space. All the species share a common wild-type phenotype (blue); however, each species renders a unique phenotype (light grey) upon moderate increases or decreases in inductive signal. The position of the species-specific phenotypes relative to the wild-type phenotype in the phase diagram was used to infer the parameter regions associated with each wild-type species. Briefly, we identified the regions within the wild-type space that transition to species-specific mutant phenotypes upon increasing or decreasing the inductive signal (*x*-axis), while holding all other parameters (*y*-axis) constant (Section 4.10). This approach reveals how parameters P_k differ among the different species. (B), (C) The likelihood that *C. elegans* differs from *C. remanei* (B) or *C. briggsae* (C) by higher (open columns) or lower (filled columns) values for parameters indicated on the *x*-axis.

To address this question, we used the experimental observation that each species produces different phenotypes when the level of inductive signal is changed (Figure 4.10)[16]. For example, *C. elegans* transitions from the wild-type phenotype 3°2°1°2°3°

(WT) to 3°3°1°3°3° when inductive signal is reduced moderately; meanwhile, *C. remanei* forms 3°2°3°2°3° upon intermediate reductions in inductive signal. In both species, a strong reduction in inductive signal produces 3°3°3°3°3°. Similarly, *C. briggsae* forms patterns with adjacent 1° fates upon mild increase of inductive morphogen signal, while *C. elegans* requires a strong increase in morphogen activity to render such outcomes. By identifying the subset of wild-type parameter values that produce a WT → 3°3°1°3°3° → 3°3°3°3°3° transition versus WT → 3°2°3°2°3° → 3°3°3°3°3°3° transition upon reducing inductive signal, we isolated the *C. elegans* and *C. remanei* parameter subspaces (Section 4.10). Similarly, by distinguishing between WT → 1°2°1°2°1°→1°1°1°1°1° transitions from WT → 2°1°1°1°2° → 1°1°1°1°1° transitions, we segregated the *C. elegans* and *C. briggsae* subspaces.

Comparing the parameters associated with each species reveals the quantitative differences among *C. elegans, C. briggsae* and *C. remanei*. We discovered two potential groups of parameters (Figure 4.4B and Figure 4.4C). The values of the first group may be higher or lower in *C. elegans* relative to *C. remanei* or *C. briggsae*. Thus, these parameter values may have increased or decreased as the common ancestor evolved to *C. elegans*, *C. remanei* and *C. briggsae*. In contrast, our model predicts a second class of parameters whose values must have changed in a biased manner during the diversification that led to *C. elegans*, *C. remanei* and *C. briggsae*. For example, *C. elegans* is likely to produce a weaker lateral signal in response to inductive signaling than would *C. remanei* (Figure 4.4B). Similarly, inductive signaling is predicted to be more sensitive to negative regulators in *C. elegans* than in *C. briggsae* (Figure 4.4C). In this manner, our model analysis uncovers insights into the quantitative diversification that led to several closely related species operating the same network in quantitatively distinct ways.

4.6 Computational Model of *C. elegans* Vulval Development

4.6.1 Signaling Network and Model Equations

The vulva in *C. elegans* and related species develops from a set of equivalent vulva precursor cells (VPCs) labeled Pn.p (n = 3 to 8) in Figure 4.5 [17]. These cells are arranged linearly along the antero-posterior axis of the body. During the third stage of larval development, the VPCs receive a spatially graded EGF-like stimulus (LIN-3) from the anchor cell (AC) in the gonad. Binding of LIN-3 to its receptor LET-23 activates the MAP kinase MPK-1 and induces their differentiation. In addition to the soluble LIN-3 signal, juxtracrine interactions through Notch-like receptor LIN-12 contribute to VPC differentiation. Together, the inductive LIN-3 signal and the lateral Notch signal establish a pattern of VPC differentiation (3°3°2°1°2°3°) in wild-type organisms (Figure 4.5). Only the VPCs committed to 1° and 2° fates contribute to vulva formation through cell divisions and spatial rearrangements of the daughter cells; meanwhile, the daughters of the 3^{o}-committed VPC fuse to the hypodermal syncytium.

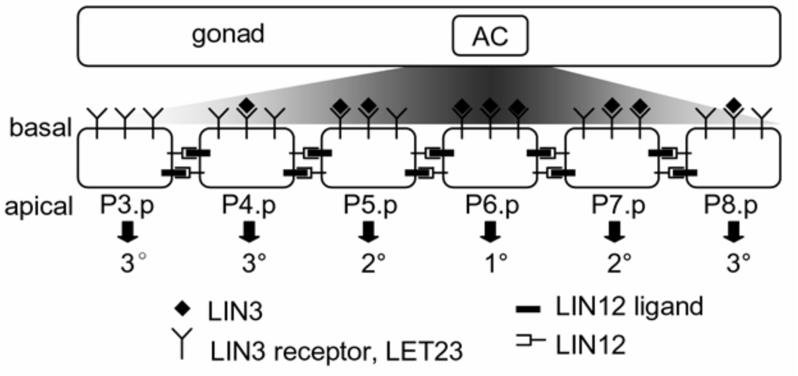

Figure 4.5. Wild-type patterning of *C. elegans* vulva
The anchor cell (AC) stimulates the vulva precursor cells Pn.p with LIN-3 in a graded manner. These cells laterally interact with one another through LIN-12 pathway. Integration of signaling from LIN-3 receptor LET-23 and LIN-12 receptor results in the wild-type pattern of differentiation 3°3°2°1°2°3°.

We previously described a mathematical model of the LIN-3/LIN-12 signaling network [5]. This model was based on the current understanding of the bidirectional coupling between LIN-3 and LIN-12 signaling pathways (Figure 4.6). To make the model tractable, we represented multistage signaling cascades and redundant pathways as a single reaction pathway. This coarse-grained representation completely maintains the regulatory logic of the LIN-3/LIN-12 network, while simplifying its mathematical representation.

Ordinary differential equations were formulated to track the level of two fate-encoding signals in each cell *i*: active MAP kinase (MAPK) molecules (mpk_i^*) and lateral signal activity (lat_i). These equations are:

$$\begin{aligned}
\frac{\mathrm{d}\left(\mathrm{mpk}_{\mathrm{i}}^{*}\right)}{\mathrm{d}t} &= k_m^{+}\mathrm{Ind}_{\mathrm{i}}\left(\mathrm{mpk}_{\mathrm{i}}\right) - k_m^{-}\left(\mathrm{Ph}_{\mathrm{T}}\right)\left(\mathrm{mpk}_{\mathrm{i}}^{*}\right) - k_{x_1}\frac{\left(\mathrm{lat}_{\mathrm{i}}\right)^2}{K_{M_{\mathrm{lat}}}^2 + \left(\mathrm{lat}_{\mathrm{i}}\right)^2}\left(\mathrm{mpk}_{\mathrm{i}}^{*}\right), \\
\frac{\mathrm{d}\left(\mathrm{lat}_{\mathrm{i}}\right)}{\mathrm{d}t} &= k_n^{+} - k_n^{-}\left(\mathrm{lat}_{\mathrm{i}}\right) - k_{x_2}\left(\mathrm{mpk}_{\mathrm{i}}^{*}\right)\left(\mathrm{lat}_{\mathrm{i}}\right) + k_{x_3}\frac{\left(\dfrac{\mathrm{mpk}_{\mathrm{i+1}}^{*}}{\nu_{\mathrm{i+1}}} + \dfrac{\mathrm{mpk}_{\mathrm{i-1}}^{*}}{\nu_{\mathrm{i-1}}}\right)^2}{K_{M_{\mathrm{ind}}}^2 + \left(\dfrac{\mathrm{mpk}_{\mathrm{i+1}}^{*}}{\nu_{\mathrm{i+1}}} + \dfrac{\mathrm{mpk}_{\mathrm{i-1}}^{*}}{\nu_{\mathrm{i-1}}}\right)^2},
\end{aligned} \tag{4.1}$$

where ν_i is the number of neighbors for cell *i* and the other dimensional parameters are described in the legend to Figure 4.6.

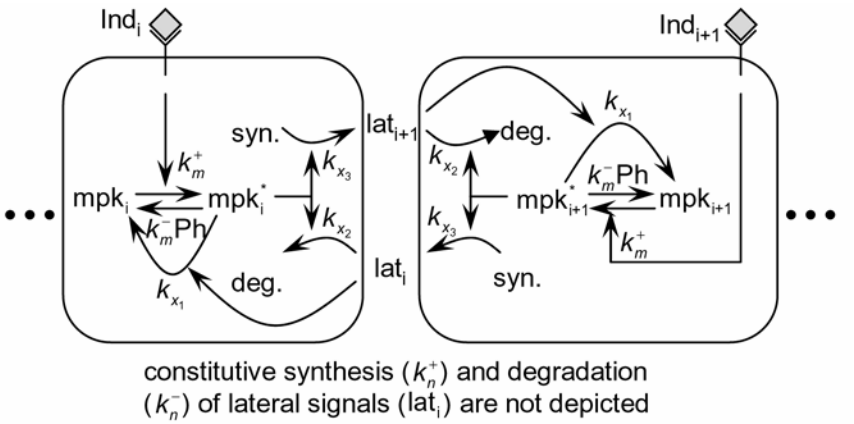

Figure 4.6: Schematic of molecular interactions within and among VPCs. A pair of cells, *i* and *i+1*, within the VPC array are shown; in each cell *i* the inductive LIN-3 signal Ind_i activates MPK-1 in each cell with rate constant k_m^+. The deactivation of MPK-1* occurs at a rate determined by the expression level of constitutive phosphatases (Ph_T) and the rate constant k_m^-. The lateral signal mediated by receptor LIN-12 is constitutively activated in each cell at rate k_n^+ and degrades linearly with rate constant k_n^- (not depicted). The inductive signal upregulates the lateral signal in the neighboring cell with rate constant k_{x_3} and downregulates it in the same cell with rate constant k_{x_2}. In turn, the lateral signal in each cell deactivates MPK-1* with rate constant k_{x_1}

In addition, each VPC is stimulated by a local amount of inductive signal, Ind_i. The values for Ind_i were determined by modeling diffusive transport of the soluble factor coupled with linear degradation in the extracellular space. At steady state, the gradient is described by:

$$0 = D\frac{\partial^2[\mathrm{Ind}]}{\partial x^2} - k_d[\mathrm{Ind}], \tag{4.2}$$

whose solution is:

$$[\mathrm{Ind}](x) = [\mathrm{Ind}_{\mathrm{P6.p}}]e^{-\sqrt{\frac{k_d}{D}}x}, \tag{4.3}$$

when we require that $[\mathrm{Ind}](x=0) = [\mathrm{Ind}_{\mathrm{P6.p}}]$. We rewrite this solution by re-scaling the spatial axis, *x*, in terms of the length of P3.p-P6.p VPC field, *L*, as follows:

$$[\mathrm{Ind}](\tilde{x}) = [\mathrm{Ind}_{\mathrm{P6.p}}]e^{-\sqrt{\frac{k_d}{D}}L\frac{\tilde{x}}{3}} = [\mathrm{Ind}_{\mathrm{P6.p}}]\Delta I^{\frac{\tilde{x}}{3}}, \tag{4.4}$$

where $\tilde{x}$ is 0, 1, 2 and 3 for P6.p, P5/7.p, P4/8.p and P3.p, respectively. Thus, the parameters $\mathrm{Ind}_{\mathrm{P6.p}}$ and *ΔI* specify the local level of inductive signal (Ind_i). A change in the value of ΔI alters the steepness of the exponential gradient in inductive signal.

The dimensional variables $\mathrm{mpk}_\mathrm{i}^*$ and lat_i were normalized by their characteristic values, mpk_T and lat_T, respectively to yield the following non-dimensional state variables:

$$m_i = \frac{\mathrm{mpk}_\mathrm{i}^*}{\mathrm{mpk}_\mathrm{T}}, \quad l_i = \frac{\mathrm{lat}_\mathrm{i}}{\mathrm{lat}_\mathrm{T}}.$$

Subsequently, dimensional parameters in the model equations were re-arranged to identify the following dimensionless parameter groups:

$$\tau = k_m^-(\mathrm{Ph}_\mathrm{T})t, \quad I = \frac{k_m^+(\mathrm{Ind}_{\mathrm{P6.p}})}{k_m^-(\mathrm{Ph}_\mathrm{T})}, \quad \chi = \frac{k_{x_1}}{k_m^-(\mathrm{Ph}_\mathrm{T})}, \quad \lambda = \frac{k_n^+}{k_n^-(\mathrm{lat}_\mathrm{T})},$$

$$\phi = \frac{k_{x_3}}{k_n^-(\mathrm{lat}_\mathrm{T})}, \quad \theta = \frac{k_{x_2}(\mathrm{mpk}_\mathrm{T})}{k_n^-}, \quad \kappa_m = \frac{K_{M_{\mathrm{ind}}}}{\mathrm{mpk}_\mathrm{T}}, \quad \kappa_l = \frac{K_{M_{\mathrm{lat}}}}{\mathrm{lat}_\mathrm{T}}, \quad \gamma = \frac{k_n^-}{k_m^-(\mathrm{Ph}_\mathrm{T})}.$$

Using these non-dimensional quantities, the model equations may be re-written as follows:

$$\frac{\mathrm{d}m_i}{\mathrm{d}\tau} = \left(\Delta I\right)^{\frac{\tilde{x}}{3}} I\left(1-m_i\right) - m_i - \chi m_i \frac{l_i^2}{\kappa_l^2 + l_i^2},$$

$$\frac{\mathrm{d}l_i}{\mathrm{d}\tau} = \gamma\left[\lambda - l_i - \theta m_i l_i + \phi \frac{\left(\frac{m_{i-1}}{\nu_{i-1}} + \frac{m_{i+1}}{\nu_{i+1}}\right)^2}{\kappa_m^2 + \left(\frac{m_{i-1}}{\nu_{i-1}} + \frac{m_{i+1}}{\nu_{i+1}}\right)^2}\right]. \tag{4.5}$$

4.6.2 Framework for Assigning Cell Fates

The timing of VPC patterning has been studied by ablating the anchor cell (AC) at different times during the induction process. Results from these experiments have established that the AC (and therefore, the LIN-3 signal that it secretes) is needed for approximately 6 hours in order for the VPCs to commit to the 3°3°2°1°2°3° fate pattern [10, 18]. Our model calculations show that the fate-determining signals (MAP kinase (m_i) and lateral (l_i) signals) reach their steady-state values within 5 hours for reference parameter values (detailed below). Therefore, we worked under the reasonable assumption that the steady-state values of m_i and l_i prescribe the fate choice of each VPC. For all simulations, the steady-state solution of the dimensionless model equations was determined using the initial condition that the levels of inductive and lateral signal are zero in all cells. We note that for steady-state calculations the dimensionless group γ is eliminated from model Equation 4.5.

The output of each simulation is the dimensionless magnitudes of the fate-determining signals (m_i, l_i). These are in turn recast into the dimensional form (mpk_i^*, lat_i) from which fate assignments are determined using the framework that we described previously [5]. Briefly, (mpk_i^*, lat_i) in each VPC is a point in the (mpk^*, lat) fate plane. Two orthogonal thresholds, ($\mathrm{mpk}_{\mathrm{Th}}^*$, $\mathrm{lat}_{\mathrm{Th}}$) segregate the fate plane into four quadrants. The dimensional inductive and lateral signals in each cell are compared against their respective threshold values, which then translate into 1º, 2º, 3º or *m* fate quadrants (Table 4.2).

Table 4.2. Fate assignment based on threshold values
The dimensional solution to model Equation 4.5 is compared for each of the six VPCs against the orthogonal thresholds ($\mathrm{mpk}_{\mathrm{Th}}^*$, $\mathrm{lat}_{\mathrm{Th}}$) resulting in a pattern of six fates. The position of the thresholds in the fate plane can vary, hence the solution to the model equations at particular parameter values can lead to different fate patterns.

$\mathrm{mpk}_i^* \le \mathrm{mpk}_{\mathrm{Th}}^*$	$\mathrm{lat}_i \le \mathrm{lat}_{\mathrm{Th}}$	Fate
Yes	No	1º
No	Yes	2º
Yes	Yes	3º
No	No	*m*

4.6.3 Reference Values for Dimensional Model Parameters

Our model entails three types of parameters: those driving protein degradation, those driving gene expression, and those driving bimolecular interactions. For the purpose of converting molar concentrations to number of molecules per cell, we assume a cellular volume of 10^{-12} L.

k_n^- is the rate of constitutive degradation of lateral signaling. Lateral signaling is mediated by complexes of LIN-12-cyto with LAG-1 transcription factor. Silencing of lateral signaling occurs due to proteosomal degradation of LIN-12-cyto [19]. The mean half-life of proteins susceptible to proteolysis has been measured to be approximately 43 minutes [20]. Therefore, the reference value of parameter k_n^- is set to 0.016 min^{-1}.

k_{x_2} is the rate constant of lateral signaling destruction due to MPK-1^*-mediated endocytosis of LIN-12 receptors. The reference value of k_{x_2} is 2×10^{-6} $(\text{molec/cell})^{-1}$ min^{-1}, obtained from the rate constant for receptor/complex endocytosis [21] adjusted for the fraction of active MPK-1^*.

k_n^+ is the constitutive rate of lateral signaling synthesis. This process it thought to be limited by generation of LIN-12 receptors or their ligands. We set the reference value for k_n^+ at 130 molec/cell/min based on the rate of EGF receptor (EGFR) synthesis [21].

k_{x_3} is the rate constant for MPK-1^* induced lateral signal generation through transcription of LIN-12 ligands. k_{x_3} reference value is set at 1,300 molec/cell/min, which is one order of magnitude larger than the constitutive rates of lateral signal synthesis k_n^+. This latter estimate is based on tenfold change in promoter activity over the basal value [22, 23].

k_m^+ and k_m^- are bimolecular rate constants describing the activation and deactivation of MAP kinase MPK-1. Their reference value was estimated from k_{cat}/K_M

values for activation and deactivation of MAP kinase by upstream kinases and phosphatases, respectively [24-26]. Hence, the reference value for these parameters is 2×10^{-4} (molec/cell)$^{-1}$ min^{-1}.

The coupling term k_{x_1} combines protein production by lateral signaling induced gene expression and bimolecular reaction between the phosphatase gene products and active MPK-1*. Hence, the reference value is 2 min^{-1}, estimated from the bimolecular reaction rate constant k_m^- and characteristic levels of induced phosphatase gene expression products which we consider to be 10^4 molecules/cell.

We consider that there is a constant number of constitutive phosphatase molecules deactivating MPK-1* during the vulva specification process, and we take this number to be $\text{Ph}_T = 5 \times 10^3$ molecules/cell. Furthermore, the total amount of MPK-1, active and inactive, does not change during this event; hence, we set $\text{mpk}_T = 10^4$ molecules/cell [24]. The characteristic level of lateral signal lat_T is estimated to be on the order of high cellular protein copy numbers; thus, we take $\text{lat}_T = 10^5$ molecules/cell. Occupied cell surface receptor levels vary from 100 to 100,000 receptors/cell [21] therefore take the following reference value, $\text{Ind}_{\text{P6.p}} = 10^4$ molecules/cell.

Concentration of transcription factors in the sea urchin embryo nucleus has been estimated to range from 300 to 10,000 molecules/nucleus [27]. Thus, set reference values $K_{M_{\text{Ind}}}$ = 1,000 molecules/cell and $K_{M_{\text{lat}}}$ = 5,000 molecules/cell.

Table 4.3. Reference values of dimensional parameters
Reference values for the dimensional model parameters were determined as detailed in the text.

Parameters	Reference Value	Units
k_m^+, k_m^-	2×10^{-4}	$(\text{molec/cell})^{-1}\ \text{min}^{-1}$
k_{x_2}	2×10^{-6}	$(\text{molec/cell})^{-1}\ \text{min}^{-1}$
k_n^+	130	molec/cell/min
k_{x_3}	1,300	molec/cell/min
k_n^-	0.016	min^{-1}
k_{x_1}	2.0	min^{-1}
$K_{M_{\text{Ind}}}$	1,000	molec/cell
$K_{M_{\text{lat}}}$	5,000	molec/cell
$\text{Ind}_{\text{P6.p}}$	10^4	molec/cell
mpk_{T}	10^4	molec/cell
lat_{T}	10^5	molec/cell
Ph_{T}	5×10^3	molec/cell

4.6.4 Reference Values for Dimensionless Parameters

From the reference values for dimensional parameters, the following reference values for dimensionless parameters were computed:

$$I = 2, \quad \chi = 2, \quad \lambda = 0.08, \quad \phi = 0.8, \quad \theta = 1.25, \quad \kappa_m = 0.1, \quad \kappa_l = 0.05.$$

To determine a representative value for the gradient steepness, we note that a flat gradient would be represented by $\Delta I = 1$. In contrast, the steepest gradient occurs when a maximum number of receptors [21] (10^5/cell) are occupied in the P6.p cell and only a single receptor is occupied in the neighboring P5/7.p cell. Thus, the steepest gradient is represented by $\Delta I = 10^{-5}$. The center value for ΔI (Table 4.4) was chosen to approximate the geometric mean of these limiting scenarios.

4.7 Quantifying Phenotypic Capacity

In order to explore phenotypes that would result from quantitative variations in network performance, we varied each dimensionless parameter about its central value, chosen to be near its reference value (Table 4.4). The parameter space was expanded in a step-wise fashion by increasing and decreasing each parameter value by ~3-4 fold (Figure 4.7). Thus, the parameter space hypervolume expanded sequentially: 3^8, 5^8, 7^8, 9^8 and ultimately 11^8. Therefore, at its maximum size, the parameter space contained 11 values per parameter (equally spaced on a log scale), spanned 5-6 orders of magnitude for each parameter, and represented 11^8 parameter combinations in total.

Table 4.4. Range of values for dimensionless model parameters
The center parameter values were placed near the reference parameter values. The minimum and maximum values for each parameter are determined upon eleven point discretization of each parameter axis as depicted in Figure 4.7.

Dimensionless Parameter	Center Value	Maximum Value	Minimum Value
I	0.93	5.6×10^{2}	1.5×10^{-3}
ΔI	6×10^{-3}	3.6×10^{-5} (steepest)	1 (most shallow)
χ	0.93	5.6×10^{2}	1.5×10^{-3}
λ	5×10^{-2}	8.0	2.9×10^{-4}
ϕ	0.48	2.9×10^{2}	8.0×10^{-4}
θ	1.61	9.7×10^{2}	2.7×10^{-3}
κ_m	6×10^{-2}	10.0	3.6×10^{-4}
κ_l	4×10^{-2}	6.5	2.32×10^{-4}

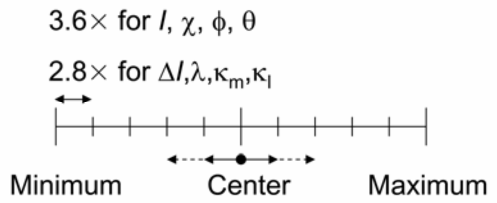

Figure 4.7. Discretization of parameter axes
Each parameter axis was discretized at eleven points equally spaced on a log scale. The center point along each parameter axis is near the reference value for each parameter. The analysis of parameter spaces of different sizes (but at the same discretization of parameter axis) was performed by considering increasing numbers of points around the center value as indicated by centered double arrows.

For each combination of 8 model parameter values, we computed the fate pattern. Importantly, the fate of each cell *i* is determined by whether the amounts of MAP kinase and lateral signals in that cell ($\mathrm{mpk_i}$ and $\mathrm{lat_i}$) exceed threshold levels ($\mathrm{mpk_{Th}}$ and $\mathrm{lat_{Th}}$, respectively; see Table 4.2). Because these threshold values are unknown, and in fact, may be a source of variation in an evolutionary context, we computed fate patterns across a broad range of threshold values. Specifically, $\mathrm{mpk}^*_{\mathrm{Th}}$ and $\mathrm{lat_{Th}}$ were varied across the ranges $0 \le \mathrm{mpk}^*_{\mathrm{Th}} \le 10{,}000$ molec/cell and $0 \le \mathrm{lat}_{\mathrm{Th}} \le 100{,}000$ molec/cell, respectively. The cumulative number of fates predicted across the 8-dimensional parameter space for every combination of threshold values is reported in Figure 4.1A.

Since each phenotype occupies a different amount of the parameter space, we quantified how phenotypes are distributed in the parameter space (Figure 4.1B). The number of parameter points associated with each phenotype was tallied at every combination of threshold values. This total level of occurrence of each phenotype was divided by the total number of parameter points to yield the Fraction of Parameter Space occupied by that particular phenotype. Phenotypes were binned according to the Fraction of Parameter Space occupied in unit $\log_{10}$ bins (i.e., 1 to 0.1, 0.1 to 0.01, etc). The number of distinct phenotypes in each bin is plotted on the *y*-axis in Figure 4.1B. The distribution of parameter space occupancy was then fit to a log-normal probability distribution. There are 35 phenotypes two standard deviations above the mean (Table 4.5) and 19 phenotypes two standard deviations below the mean (Table 4.6).

Table 4.5. List of phenotypes two standard deviations above mean

Phenotype	Frequency
3° 3° 3° 3° 3° 3°	0.5458
3° 3° 3° 1° 3° 3°	0.1293
1° 1° 1° 1° 1° 1°	0.0967
3° 3° 1° 1° 1° 3°	0.0949
3° 1° 1° 1° 1° 1°	0.0538
2° 2° 2° 2° 2° 2°	0.0146
3° 3° 2° 3° 2° 3°	0.0109
3° 2° 2° 2° 2° 2°	0.0065
m m m m m m	0.0061
2° 2° 2° m 2° 2°	0.0053
2° 2° m m m 2°	0.0052
2° m m m m m	0.0032
3° 3° 2° 2° 2° 3°	0.0028
3° 2° 2° m 2° 2°	0.0022
3° 3° 2° 1° 2° 3°	0.0020
2° 2° 2° 3° 2° 2°	0.0014
3° 2° 2° 3° 2° 2°	0.0013
2° 3° 1° 1° 1° 3°	0.0011
2° 2° 3° 3° 3° 2°	0.0011
2° 2° 3° 1° 3° 2°	0.0011
3° 2° m m m 2°	0.0011
2° 2° 1° 1° 1° 2°	0.0009
2° 3° 3° 1° 3° 3°	0.0009
3° 2° 2° 2° 2° 3°	0.0008
2° 2° 2° 1° 2° 2°	0.0007
2° 3° 3° 3° 3° 3°	0.0007
3° 1° 3° 1° 3° 1°	0.0007
3° 2° 3° 3° 3° 2°	0.0006
3° 2° 3° 1° 3° 2°	0.0006
3° 2° 2° 1° 2° 2°	0.0006
3° 3° 2° m° 2° 3°	0.0006
2° 1° 1° 1° 1° 1°	0.0005
1° m m m m 1°	0.0004
1° 3° 3° 1° 3° 1°	0.0004

Table 4.6. List of phenotypes two standard deviations below mean

Phenotype	Frequency
2° 2° 1° 3° 1° 3°	$1.21\cdot10^{-13}$
m 2° 1° 1° m 1°	$1.05\cdot10^{-13}$
m 2° m 1° 2° 2°	$8.56\cdot10^{-14}$
1° 2° 3° m 2° 2°	$7.86\cdot10^{-14}$
1° 2° 1° m 2° 2°	$6.18\cdot10^{-14}$
2° 2° 1° m 2° 1°	$4.36\cdot10^{-14}$
m 2° 1° m m 2°	$3.48\cdot10^{-14}$
1° 2° 3° 2° 2° 2°	$3.46\cdot10^{-14}$
m 2° 1° 1° 1° 1°	$1.09\cdot10^{-14}$
3° 2° 1° 3° 3° 2°	$1.03\cdot10^{-14}$
2° 2° 1° 3° 3° 2°	$5.12\cdot10^{-15}$
2° 3° 1° 3° 3° 3°	$2.36\cdot10^{-15}$
3° 2° m 2° m 2°	$2.1\cdot10^{-15}$
2° 2° 1° 2° 3° 2°	$8.45\cdot10^{-16}$
3° 2° 1° 2° 3° 2°	$7.42\cdot10^{-16}$
2° 2° 1° 3° 3° 3°	$3.67\cdot10^{-16}$
2° 2° 1° 2° m 2°	$3.38\cdot10^{-16}$
3° m 1° 1° 2° 1°	$2.72\cdot10^{-16}$
2° 2° 1° 2° 2° 2°	$6.21\cdot10^{-18}$

4.8 Transition Probability between Phenotypes

Each phenotype, including the wild type, occupies a subspace within the 8-dimensional parameter space (Figure 4.2A). This phase diagram of phenotypes was analyzed to address the following question: given a choice of 8 single mutations (i.e., 8 parameter perturbations), which single-parameter change (i.e., single mutation) would be most likely to promote a transition from wild-type (W) to a mutant (M) phenotype? To address this question, we rank ordered the parameters according to their relative transition probabilities (Figure 4.2B and Figure 4.2C), computed as described below. The same transition probability metric is computed to quantify the single-parameter differences that distinguish *C. elegans* from closely related species (Figure 4.4B and Figure 4.4C). For this analysis, "transitions" between parameter spaces associated with *C. elegans* and another species (*C. briggsae* or *C. remanei*) were considered.

For the purpose of this discussion, let P_k denote each dimensionless parameter where $k = 1$ to 8. Let i denote a point in the W parameter space, and j denote a point in the M parameter space (Figure 4.2A). By scanning through all (i, j) pairs, we determined the total number that differ only by a single parameter value. These pairs represent the cases where a single-parameter change can cause a W → M phenotype transition. Among this total number of single-mutation pairs, we determined the fraction of phenotype transitions that are attributable to an increase in a particular parameter P_k. This fraction is the transition probability of W → M phenotype transition by *increasing* P_k. The same calculation was conducted for quantifying the transition probability due to a decrease in P_k.

Importantly, the 8-dimensional phenotype phase diagram will be sensitive to the threshold values of MAPK ($\mathrm{mpk}^{*}_{\mathrm{Th}}$) and lateral ($\mathrm{lat}_{\mathrm{Th}}$) signals. Recall that these thresholds determine how fates are assigned (Table 4.2). To determine the robustness of the transition probability to variations in the fate-determining thresholds, we computed the transition probability for 25 different threshold combinations spanning the following ranges:

$$\begin{aligned} \mathrm{mpk}^{*}_{\mathrm{Th}} &\in \left[1,000;2,000;3,000;4,000;5,000\right] \text{ molecules/cell} \\ \mathrm{lat}_{\mathrm{Th}} &\in \left[10,000;20,000;30,000;40,000;50,000\right] \text{ molecules/cell} \end{aligned}$$

The *y*-axes of Figure 4.2B, Figure 4.2C, Figure 4.4B, and Figure 4.4C report the mean transition probability computed over all 25 threshold combinations, and the error bar denotes the standard deviation.

4.9 Phenotype Diversity from Quantitative Changes in the Level of Inductive Signal

Using the phenotype phase diagram, we determined all the mutant phenotypes that may be rendered solely by increasing (or decreasing) the inductive signal. Since some mutant phenotypes are more prevalent than others, we quantified the likelihood that an increase (or decrease) in inductive signal would produce each mutant (M). To quantify this Likelihood of Phenotype Occurrence, we first tallied the total number of ways that a change in inductive signal (*I*) would abolish the wild-type (W) phenotype. Among this total, we quantified the fraction that shifted W to a specific mutant M upon an increase (or decrease) in *I*. This fraction represents the likelihood of producing M phenotype by an increase (or decrease) in inductive signal (*I*).

Phenotype assignments must be sensitive to fate-determining threshold values of MAPK and lateral signals (Table 4.2). To quantify the robustness of the Likelihood of Phenotype Occurrence to threshold variations, we performed the calculation for 25 different threshold combinations (Section 4.8). The mean of the Likelihood of Phenotype Occurrence is reported in Figure 4.3A and Figure 4.8A, and the error bars denote the standard deviation. Figure 4.3A shows the mutant phenotypes with the greatest Likelihood of Phenotype Occurrence upon an increase (empty) or decrease (filled) in inductive signal. The more complete set of phenotypes, including the ones that occur less frequently, are shown in Figure 4.8A. Similar calculations were performed to determine the phenotype diversity due to changes in gradient steepness. Figure 4.9 shows the mutant phenotypes with greatest Likelihood of Phenotype Occurrence upon an increase (empty) and decrease (filled) in gradient steepness. Note the occurrence of 1°2°2°1°2°1° and 2°1°2°1°2°1° phenotypes in both Figure 4.3A and Figure 4.9.

In addition to the likelihood of generating a particular mutant phenotype, it is also important to gauge the amount of change in inductive signal needed to render each mutant. Some mutant phenotypes may require only small changes, while others may require substantial perturbations. Therefore, we quantified the Fold Change in *I* needed to produce a specific mutant phenotype (M). For every increase (or decrease) in *I* that produced phenotype M, we kept track of the associated magnitude of change in *I*. The geometric mean of these magnitudes was computed to give the Fold Change in *I*. As with other calculations, we examined the robustness of this quantity to variations in fate-determining thresholds. The mean Fold Change in *I* across a broad range of threshold settings is reported in Figure 4.3B and Figure 4.8B, and the error bars represent the standard deviation.

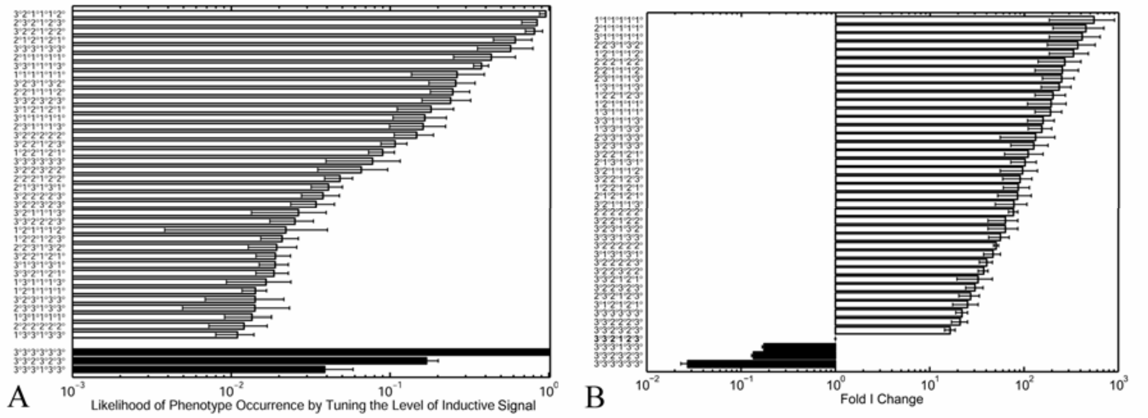

Figure 4.8. Extended set of phenotypes occurring upon I change
(A) Ranking of phenotypes according to their likelihood to be reached upon changes in the morphogen levels. (B) Fold changes in *I* required for reaching these diverse phenotypes.

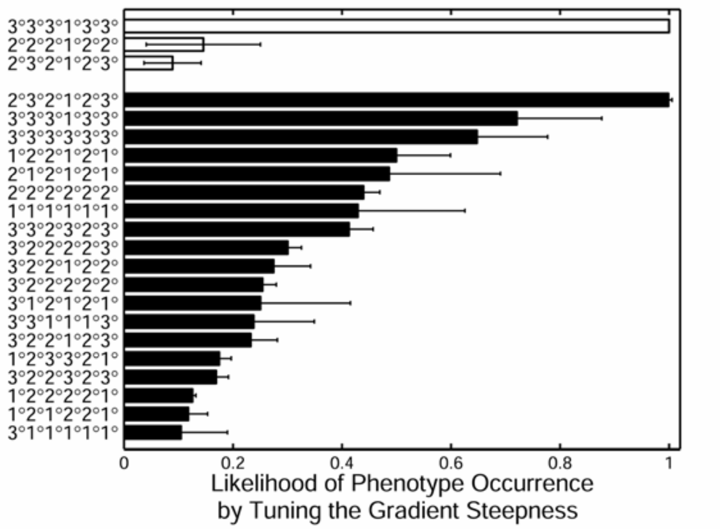

Figure 4.9. Phenotypic diversity caused by quantitative changes in gradient steepness
Mutant phenotypes with greatest Likelihood of Phenotype Occurrence upon an increase (empty) and decrease (filled) in gradient steepness *ΔI*.

4.10 Segregation of Wild-type Parameter Space into Species-specific Regions

Quantitative perturbation of morphogen levels in several species of *Caenorhabditis* has revealed a plethora of phenotype patterns that the vulva precursor cells can attain (Figure 4.3C [16]). The first striking observation is that the predicted phenotypes with the greatest Likelihood of Occurrence upon changing *I* (Figure 4.3A) match those reported in experiments (Figure 4.3C). Moreover, the model predicts the magnitude of change needed to produce each phenotype (Figure 4.3B); these quantitative predictions again match the quantitative hierarchy of phenotypes observed in experiment (Figure 4.3C).

A key experimental observation is that changes in inductive signal produce species-specific phenotypes [16]. Figure 4.10 highlights the progression of phenotypes observed in *C. elegans*, *C. briggsae* and *C. remanei* along the inductive signal axis. We used these experimental observations to segregate the wild-type space into species-specific regions using the methodology described on the next page.

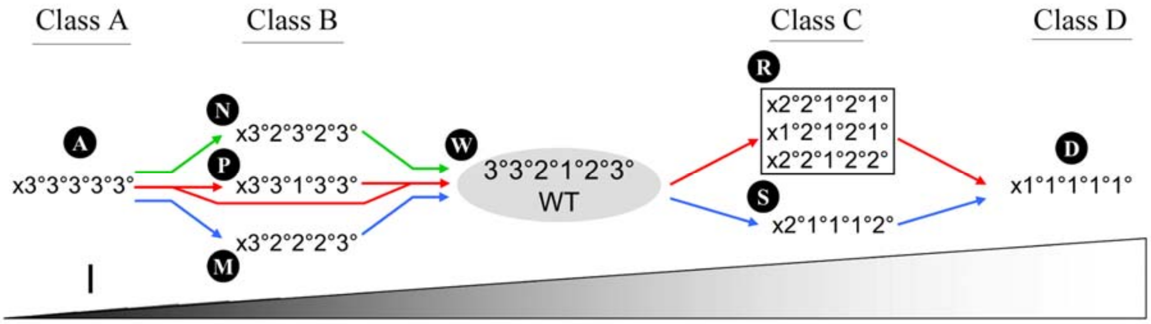

Figure 4.10. Summary of phenotypes observed experimentally in *Caenorhabditis* in response to changes in the level of inductive signal
The red, blue and green arrows denote the progression of phenotypes reported by Felix [16] in *C. elegans*, *C. briggsae* and *C. remanei*, respectively, as the level of inductive signal (*I*) is increased. Phenotypes associated with *C. elegans* have also been documented in several other reports [9, 28]. Classes A, B, C and D are described in the legend to Figure 4.3C. Here, we have labeled the phenotypes within classes B and C as N, P, M, R and S in order to distinguish species-specific phenotypes. The wild-type phenotype is labeled W. Phenotypes were not reported in *C. remanei* upon increasing inductive signal above the wild-type level [16]; therefore, green arrows are not drawn to the right of the wild-type phenotype.

First, we designated each phenotype with a letter code (Figure 4.10), so that a string of characters or a word may be used to represent the phenotype progression of each species. Phenotypes that are not described in Figure 4.10 were designated "O". For example, following the lines for *C. elegans* in Figure 4.10, one word is APWRD. Using this nomenclature, we identified the words that are consistent with the fate progression observed experimentally in *C. elegans*, *C. briggsae* and *C. remanei* (Table 4.7).

Table 4.7. Characteristic words associated with each species
Words are formed from letters designated for each phenotype (Figure 4.10) in order to represent the experimentally observed, species-specific phenotype progressions along the inductive signal (*I*) axis (Figure 4.10).

Species	Words assigned
C. elegans	AW, APW, AWR, APWR, AWRD, APWRD, WRD, WR, PW, PWRD, PWR
C. briggsae	AMW, AWSD, AWS, APWSD, APWS, WSD, WS, PWSD, PWS
C. remanei	(A)NW*

Next, we determined the word associated with every point in the wild-type parameter space. To construct the word, we varied the value of *I* from its minimum to maximum while holding all other parameter values constant. As the *I*-axis was traversed, we recorded each phenotype with its character designation, thereby yielding a 11-character word (11 characters because of the discretization of the *I*-axis). The length of these words was then condensed by eliminating adjacent repeats of a character. For example, APPPOWOSSDD would become APOWOSD (Figure 4.11). Since "O" phenotypes include cases where VPCs are designated as "m" fate (a fate whose experimental equivalent remains to be elucidated), we removed "O" from the predicted words. In the example, APOWOSD would become APWSD. Thus, at the end of this step, every point in the wild-type parameter is associated with a word that characterizes how the phenotype would change when *I* is increased or decreased.

Finally, we compared the predicted words associated with each point in wild-type parameter space with the experimentally observed phenotype progressions/words of *C. elegans*, *C. briggsae* and *C. remanei*. In this manner, we identified the regions within the wild-type parameter space associated with each species. We find that *C. elegans* represents 41.01±7.90%, *C. briggsae* represents 3.71±1.95%, and *C. remanei* represents 41.31±8.20% of all wild-type space points. The remaining 13.97±2.25% of wild-type space points represent words that are inconsistent with experimental results for these three species.

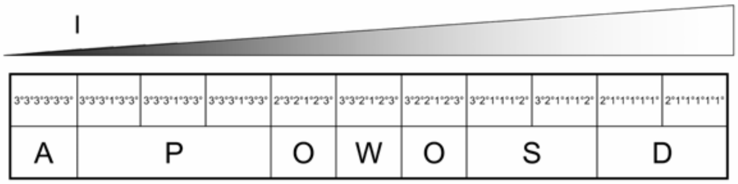

Figure 4.11. Illustration of translation of phenotypes along morphogen axis to words A sample wild-type space point that leads to 3°3°3°3°3°3°, 3°3°3°1°3°3° and 2°3°2°1°2°3° phenotypes and 3°2°2°1°2°3°, 3°2°1°1°1°2° and 2°1°1°1°1°1° phenotypes upon decreasing and increasing morphogen levels, respectively, is translated to its corresponding word according to the procedure detailed in the text.

4.11 References

1. Nusslein-Volhard, C. and E. Wieschaus, *Mutations affecting segment number and polarity in Drosophila.* Nature, 1980. **287**(5785): p. 795-801.
2. Sulston, J.E. and H.R. Horvitz, *Abnormal cell lineages in mutants of the nematode Caenorhabditis elegans.* Dev Biol, 1981. **82**(1): p. 41-55.
3. Arnone, M.I. and E.H. Davidson, *The hardwiring of development: organization and function of genomic regulatory systems.* Development, 1997. **124**(10): p. 1851-64.
4. Kirschner, M. and J. Gerhart, *Evolvability.* Proc Natl Acad Sci U S A, 1998. **95**(15): p. 8420-7.
5. Giurumescu, C.A., P.W. Sternberg, and A.R. Asthagiri, *Intercellular coupling amplifies fate segregation during Caenorhabditis elegans vulval development.* Proc Natl Acad Sci U S A, 2006. **103**(5): p. 1331-6.
6. Fisher, J., et al., *Computational insights into Caenorhabditis elegans vulval development.* Proc Natl Acad Sci U S A, 2005. **102**(6): p. 1951-6.
7. Fisher, J., et al., *Predictive modeling of signaling crosstalk during C. elegans vulval development.* PLoS Comput Biol, 2007. **3**(5): p. e92.
8. Greenwald, I.S., P.W. Sternberg, and H.R. Horvitz, *The lin-12 locus specifies cell fates in Caenorhabditis elegans.* Cell, 1983. **34**(2): p. 435-44.
9. Sternberg, P.W. and H.R. Horvitz, *The combined action of two intercellular signaling pathways specifies three cell fates during vulval induction in C. elegans.* Cell, 1989. **58**(4): p. 679-93.
10. Kimble, J., *Alterations in cell lineage following laser ablation of cells in the somatic gonad of Caenorhabditis elegans.* Dev Biol, 1981. **87**(2): p. 286-300.
11. Sternberg, P.W., *Lateral inhibition during vulval induction in Caenorhabditis elegans.* Nature, 1988. **335**(6190): p. 551-4.
12. Yoo, A.S., C. Bais, and I. Greenwald, *Crosstalk between the EGFR and LIN-12/Notch pathways in C. elegans vulval development.* Science, 2004. **303**(5658): p. 663-6.
13. Cui, M., et al., *SynMuv genes redundantly inhibit lin-3/EGF expression to prevent inappropriate vulval induction in C. elegans.* Dev Cell, 2006. **10**(5): p. 667-72.

14. Ferguson, E.L., P.W. Sternberg, and H.R. Horvitz, *A genetic pathway for the specification of the vulval cell lineages of Caenorhabditis elegans.* Nature, 1987. **326**(6110): p. 259-67.
15. Samoilov, M.S., G. Price, and A.P. Arkin, *From fluctuations to phenotypes: the physiology of noise.* Sci STKE, 2006. **2006**(366): p. re17.
16. Felix, M.A., *Cryptic quantitative evolution of the vulva intercellular signaling network in Caenorhabditis.* Curr Biol, 2007. **17**(2): p. 103-14.
17. Sulston, J.E. and H.R. Horvitz, *Post-embryonic cell lineages of the nematode, Caenorhabditis elegans.* Dev Biol, 1977. **56**(1): p. 110-56.
18. Wang, M. and P.W. Sternberg, *Competence and commitment of Caenorhabditis elegans vulval precursor cells.* Dev Biol, 1999. **212**(1): p. 12-24.
19. Ilagan, M.X.G. and R. Kopan, *SnapShot: Notch Signaling Pathway.* Cell, 2007. **128**(6): p. 1246.e1-1246.e2.
20. Belle, A., et al., *Quantification of protein half-lives in the budding yeast proteome.* Proc Natl Acad Sci U S A, 2006. **103**(35): p. 13004-9.
21. Lauffenburger, D.A. and J.J. Linderman, *Receptors : models for binding, trafficking, and signaling.* 1993, New York: Oxford University Press. x, 365.
22. Buchler, N.E., U. Gerland, and T. Hwa, *Nonlinear protein degradation and the function of genetic circuits.* Proc Natl Acad Sci U S A, 2005. **102**(27): p. 9559-64.
23. Lutz, R. and H. Bujard, *Independent and tight regulation of transcriptional units in Escherichia coli via the LacR/O, the TetR/O and AraC/I1-I2 regulatory elements.* Nucleic Acids Res, 1997. **25**(6): p. 1203-10.
24. Asthagiri, A.R. and D.A. Lauffenburger, *A computational study of feedback effects on signal dynamics in a mitogen-activated protein kinase (MAPK) pathway model.* Biotechnol Prog, 2001. **17**(2): p. 227-39.
25. Force, T., et al., *Enzymatic characteristics of the c-Raf-1 protein kinase.* Proc Natl Acad Sci U S A, 1994. **91**(4): p. 1270-4.
26. Zhou, B., et al., *The specificity of extracellular signal-regulated kinase 2 dephosphorylation by protein phosphatases.* J Biol Chem, 2002. **277**(35): p. 31818-25.
27. Bolouri, H. and E.H. Davidson, *Transcriptional regulatory cascades in development: initial rates, not steady state, determine network kinetics.* Proc Natl Acad Sci U S A, 2003. **100**(16): p. 9371-6.
28. Katz, W.S., et al., *Different levels of the C. elegans growth factor LIN-3 promote distinct vulval precursor fates.* Cell, 1995. **82**(2): p. 297-307.

CHAPTER 5: RECOMMENDATIONS

5.1 Recommended Future Directions

The work conducted in this thesis offers quantitative insights into how the interplay between LIN-3/EGF inductive signaling and LIN-12 lateral signaling in the vulval precursor cells leads to robust fate specification and gives rise to multiple vulva phenotypic patterns. An important future direction for modeling will be to extend beyond the time period of fate specification and to include events associated with fate execution and further division and terminal fate specification of vulva precursor cells progeny (Figure 5.1). Modeling the terminal differentiation of VPCs will allow predictions of the detailed division patterns that occur subsequent to 1°, 2° and 3° fate specification [1, 2].

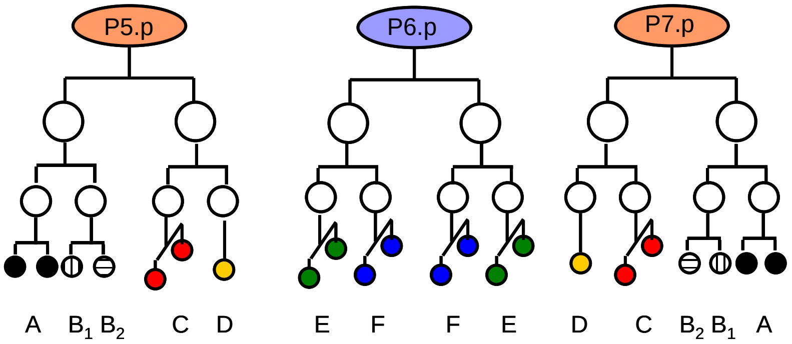

Figure 5.1. Pattern of terminal differentiation of vulva precursor cells
Seven types of cells (A, B_1, B_2, C, D E and F) represent the twenty-two cells that form the worm vulva.

Cells in a terminally differentiated vulva belong to seven classes of cells: A, B_1, B_2, C, D, E, and F. Each cell type has a specific pattern of gene expression [3]. However, only three signaling pathways regulate formation of this diverse set of classes of cells: Ras, Notch [1] and Wnt [4] signaling. Little experimental mechanistic detail is currently available about the Wnt signaling contribution to vulval patterning [5].

The modeling formalism developed in Chapter 2 assigns one fate to one biochemical marker (see Table 4.2 for fate plane definition). However, in the case of the terminally differentiated vulval cells, there are seven distinct cell types specified by only three signaling pathways. It is clear that signaling integration in the cytoplasm or at the level of *cis*-regulatory networks must occur to increase fate diversity. Further modeling efforts could include such aspects of signal integration. In fact available experimental results may offer hints on constructing a mapping from the biochemical markers of Ras, Notch, and Wnt signaling to the seven cell types. It is known that mutations in the Wnt receptors LIN-17 and LIN-18 lead to an inversion of polarity of terminal cell fates displayed by P7.p descendants (wild-type pattern DCB_2B_1A is inverted to AB_1B_2CD) [6]. Construction of the mapping would entail a binning of combinations of three signals (Ras, Notch and Wnt), potentially made distinguishable using time and space markers, into seven bins (the fates) in such a way that no two bins are the same. The time markers would be the action of signaling at one, two, four or later vulval cell stages. The space marker would be the restriction of the action of a particular signal on a specific set of P5-7.p descendants.

Our definition of the fate plane (Chapters 2 and 4) can be further improved. Currently, our model does not account for isolated vulva precursor cells undertaking a 2° fate at intermediate levels of inductive signaling [7]. A definition of fate thresholds as illustrated in Figure 5.2 would allow for such situations.

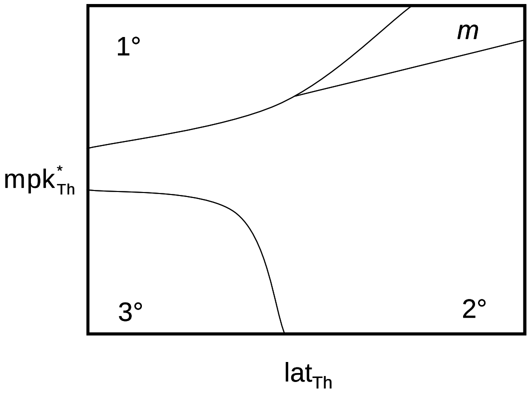

Figure 5.2. Improved definition of fate plane

The quantitative-diversification modeling approach developed in Chapter 4 could potentially be used to infer differential *Caenorhabditis* species response to molecular perturbations in the vulva patterning network. A direct application of the species-specific wild-type parameter space segregation results of Chapter 4 could be directed toward inferring the mutant vulval phenotypes that should be observed experimentally upon increases in inductive signaling in *C. remanei*.

From a computational perspective, a modeling approach based on differential equations and state-space formalism [8, 9] could be used in this system to allow for the dynamic nature of molecular interactions in an ON/OFF fashion (as in the case of spatially segregated species). While ordinary differential equations offer the advantage of allowing quantitative perturbation of model parameters, it has the disadvantage of requiring a fixed model structure which assumes that molecular interactions of a particular type occur throughout the entire period of system dynamics. The state-space approach allows for variable model structure depending on the value of the state variables in the system, essentially circumventing the need for partial differential equations encoding spatial information about molecular species

5.2 References

1. Sternberg, P.W. and H.R. Horvitz, *The combined action of two intercellular signaling pathways specifies three cell fates during vulval induction in C. elegans.* Cell, 1989. **58**(4): p. 679-93.
2. Felix, M.A., *Cryptic quantitative evolution of the vulva intercellular signaling network in Caenorhabditis.* Curr Biol, 2007. **17**(2): p. 103-14.
3. Inoue, T., et al., *Transcriptional network underlying Caenorhabditis elegans vulval development.* Proc Natl Acad Sci U S A, 2005. **102**(14): p. 4972-7.
4. Gleason, J.E., H.C. Korswagen, and D.M. Eisenmann, *Activation of Wnt signaling bypasses the requirement for RTK/Ras signaling during C. elegans vulval induction.* Genes Dev, 2002. **16**(10): p. 1281-90.
5. Gleason, J.E., E.A. Szyleyko, and D.M. Eisenmann, *Multiple redundant Wnt signaling components function in two processes during C. elegans vulval development.* Dev Biol, 2006. **298**(2): p. 442-57.
6. Deshpande, R., et al., *lin-17/Frizzled and lin-18 regulate POP-1/TCF-1 localization and cell type specification during C. elegans vulval development.* Dev Biol, 2005. **278**(1): p. 118-29.
7. Sternberg, P.W. and H.R. Horvitz, *Pattern formation during vulval development in C. elegans.* Cell, 1986. **44**(5): p. 761-72.
8. Fisher, J., et al., *Computational insights into Caenorhabditis elegans vulval development.* Proc Natl Acad Sci U S A, 2005. **102**(6): p. 1951-6.
9. Fisher, J., et al., *Predictive modeling of signaling crosstalk during C. elegans vulval development.* PLoS Comput Biol, 2007. **3**(5): p. e92.